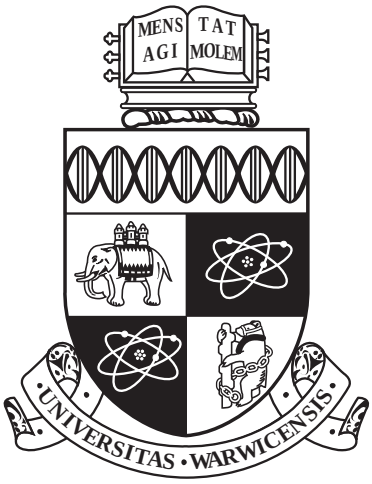

Investigating Strong Flow-Turbulence Dynamics via Numerical Simulations

by

James D Collier

Thesis

Submitted to the University of Warwick

for the degree of

Doctor of Philosophy

Department of Physics

January 2016

THE UNIVERSITY OF
WARWICK

Contents

List of Figures

Acknowledgments

First and foremost, I thank my PhD supervisor, Dr Ben McMillan, for his invaluable support and assistance through the course of my PhD. Without the help and knowledge he provided, I would not have completed this thesis.

I would also like to thank the other staff and students in the CFSA and Physics department that have helped me in anyway throughout my studies. My friends at Warwick, both inside and outside CFSA, have provided encouragement and helped make my time at the University an enjoyable experience.

I am grateful to everyone that has worked on ORB5 in the past, and present, without their work I would have no code with which to perform simulations. I would also like to acknowledge the staff that keep the supercomputers I used to perform my simulations, both Minerva at Warwick and the Helios supercomputer in Japan, operating.

I am also thankful for the University of Warwick for funding my WPRS scholarship.

Finally, an enormous thank you goes out to my family that have provided support throughout my PhD and inspired me to keep working.

Declarations

This thesis is submitted to the University of Warwick in support of my application for the degree of Doctor of Philosophy. It has been composed by myself and has not been submitted in any previous application for any degree. The work contained is my own, except where stated otherwise.

Abstract

In a magnetically confined fusion plasma, small scale instabilities drive the anomalous transport which determines the confinement. It is possible for the plasma in a tokamak to have a toroidal rotation, either formed spontaneously or by being given some external drive. This rotation may help improve confinement. Therefore, this thesis aims to investigate the effects of strongly rotating plasmas, with toroidal Mach number approaching unity, on the turbulence dynamics in numerical simulations. For this purpose, the global gyrokinetic PIC code ORB5 has been extended to include these strong-flow terms; retaining the background $E \times B$ drift terms typically neglected.

Investigations into GAMs appearing as eigenfunctions with forms similar to the Airy function found that although the behaviour of GAMs with increasing radial wavenumber were poorly predicted, eigenfunctions of the predicted form were still found. As radial wavenumber increased the eigenfunctions became less well defined.

Linear simulations with a solid-body rotation found that the frequency of the GAMs and toroidal modes with $n \neq 0$ exhibited an increase for larger magnitude of toroidal velocity and were largely independent of direction of rotation. Further studies found that an increasing toroidal rotation initially showed a destabilization effect on the linear modes, acting against the stabilizing effects of already present gradient profile flows, before beginning to reduce the mode growth at large toroidal velocities. This behaviour was found to be largely reflected in the tilting of the mode structures caused by rotation.

A stabilizing effect was also observed in collisionless non-linear simulations. The presence of a positively rotating plasma gave reductions to turbulence, but a much stronger turbulence suppression was found when the plasma was rotated in the opposite direction. It is suspected that the large flows caused by the equilibrium profile gradients give rise to some of this observed asymmetry.

Chapter 1

Introduction

1.1 Motivation

In recent times, an increasing amount of focus has been directed towards 'alternate' power sources and attempts have been made to move away from the more traditionally used fossil fuels [1]. One of the main factors causing this shift is the production of carbon dioxide from the older power source, which is likely contributing to global warming [2]. As such, renewable power has become an area of great interest in the scientific community, with upwards of two hundred billion dollars invested each year [3].

Nuclear fusion is one such source of renewable power. As well as being CO_2 neutral, fusion power also has the benefit of readily available fuel. Deuterium, one of the isotopes of hydrogen used in fusion, is easily attainable from sea water and Tritium, although much less abundant than Deuterium, can be attained through the use of Lithium breeding techniques. This ample fuel supply gives a stark contrast to the limited remaining oil reserves [4]. Additionally, a fusion reactor has no risk of an uncontrollable reaction and would produce a significantly lower amount of radioactive waste material for disposal when compared with a fission reactor. Though nuclear fusion is not without its problems.

Research into the field has been taking place since the 1950s and optimism of the simple power plants initially envisioned has long since faded [5]. However, great progress has been made and fusion reactions have now been successfully achieved in several places around the world, with the next goal being to reach a self-sustaining reaction. ITER (International Thermonuclear Experimental Reactor), a tokamak created by an international collaboration, has aims of producing 10 times more power than is input for auxiliary heating [6]. ITER is scheduled to begin plasma

experiments in 2020 [7]. Following this, there are also future plans for a device known as DEMO which is hoped to be the first demonstration of a commercial fusion power plant [8].

1.2 Fusion

Binding energy, the energy released when protons and neutrons form a nucleus, is an important concept for both nuclear fission and fusion processes. When atoms with atomic mass higher than iron split, energy is released as a result of the changing binding energy; this process is known as nuclear fission. Nuclear fusion is the opposite. When two lighter particles have sufficient energy to get close enough for the strong force to overcome the Coulomb repulsion, the two nuclei combine and energy is released. Some of the most common reactions considered use Deuterium and Tritium, two isotopes of hydrogen; most current magnetic confinement research looks at D-T mixes [9].

The most obvious problem with initiating a nuclear fusion reaction is the Coulomb repulsion between the two nuclei. To successfully overcome this repulsion the particles must be heated up to extremely high temperatures and fusion therefore typically takes place between particles in a plasma. Due to the high temperatures involved, the containment of this plasma can no longer be achieved with simple material walls and as such an alternative is required.

1.2.1 Lawson criterion

In a D-T reaction, most of the energy produced is carried by neutrons out of the device and may be used to generate electricity. The remaining alpha particles also have energy and this will in turn serve to heat the other particles in the plasma through collisions. The power from this self-heating, P_α, along with the external heating power, P_H, serve to maintain the temperature of the plasma and must balance out the power lost from the device, P_L. It is desirable to reach a point that P_α can maintain the plasma temperature against P_L on its own, without any external heating; we refer to this as the ignition point.

This is important as any fusion device must give more energy out than it takes in if it is to be feasible as a power plant. A measure of whether a plasma can achieve ignition has been provided by the Lawson criterion, first published in 1957 [10]; also known as the ignition condition.

$$nT\tau_E \geq 3 \times 10^{21} keV m^{-3} s \tag{1.1}$$

Here, n is the particle density, T is plasma temperature (ideally of order 10 keV) and τ_E is the plasma confinement time (the length of time the plasma is contained within the device). Increasing the confinement time of the reactor, i.e. minimising particle loss, is one of the easiest ways to move towards this ignition point.

1.2.2 Confinement

Fusion reactions take place naturally in stars, where the plasma is contained with gravitational confinement. Not only is this an infeasible confinement method for a fusion device, but the reaction rate of stars is also much lower than would be useful for a working reactor. The challenge is therefore to contain a plasma on Earth, with a higher temperature and density than the Sun, for as long as possible. To this end there are two leading approaches; inertial and magnetic confinement.

Inertial confinement uses lasers to heat up a fuel pellet, causing ablation on the outer layer. The resulting implosion heats the pellet and increases the density and pressure. Fusion reactions then take place within the small time window that the implosion contains the particles. There are several experiments around the world currently working on this branch of research, such as NIF [11, 12].

The other main branch of fusion research, and the focus of this thesis, is magnetic confinement fusion. Here, a magnetic field is used to exert a force on the charged particles of a plasma which move perpendicular to the field lines. The charged particles will then exhibit a gyrating motion around the magnetic field lines. By creating a closed loop with the magnetic field, the charged particles are contained within the device.

In actuality, simply having a device which creates a looped magnetic field is not enough, as the magnetic field will not be uniform across the loop. A helicity in the magnetic field is required to prevent instabilities forming. To create this helical field there are two different options; the device may be constructed so as to give a helical field straight away (as in the stellerator case) or a plasma current may be used to generate a poloidal magnetic field (as in the tokamak case). A tokamak creates this plasma current by increasing an electrical current through a central solenoid. The tokamak must therefore, by necessity, be a pulsed device.

1.3 Tokamaks

It is convenient for much of this section to discuss the tokamak on a macroscopic scale, and so fluid theory is used here despite a kinetic approach being taken through-

out the majority of this thesis. In a fluid theory, the plasma is described in terms of several macroscopic parameters such as temperature, particle density and the flow velocity. These parameters are found by taking velocity moments of the particle quantities. The time evolution of these values is then calculated via the use of fluid equations [13].

For a plasma to be in equilibrium, the basic condition is that there should be no force on the plasma at any point. Therefore, the magnetic force should balance the force caused by the plasma pressure:

$$\mathbf{J} \times \mathbf{B} = \boldsymbol{\nabla} p \tag{1.2}$$

where p is plasma pressure, J is plasma current density, and B is magnetic field. This is known as the force balance equation.

The helical field of a tokamak can be thought to contain two components: the poloidal field (B_p) and the toroidal field (B_t). If the magnetic field lines are followed around the torus of the tokamak for many turns a magnetic surface is mapped out; assuming the magnetic field line does not close on itself.

The poloidal magnetic flux within a magnetic surface, ψ, may be used as a convenient radial coordinate and label for each of these 'flux surfaces' as it can be shown to remain constant along any magnetic surface

$$\mathbf{B} \cdot \boldsymbol{\nabla} \psi = 0. \tag{1.3}$$

From this relation between B and ψ, we can define a commonly used set of tokamak coordinates, (ψ, θ, ζ), as shown in figure 1.1; where θ and ζ are poloidal and toroidal angles respectively. ψ, θ, ζ are often used to define a set of curvilinear coordinates $\boldsymbol{\nabla}\psi, \boldsymbol{\nabla}\theta$ and $\boldsymbol{\nabla}\zeta$, discussed more by D'haeseleer [14]. A function which is dependent only upon ψ, such that $f = f(\psi)$, is known as a flux function. In addition, it is common to make references to 'parallel' and 'perpendicular' directions which is understood to be in relation to the magnetic field lines. A value s is also sometimes used as a radial coordinate in place of ψ which is defined as

$$s = \sqrt{\frac{\psi}{\psi_0}} \tag{1.4}$$

where ψ_0 is ψ of the last closed flux surface.

Looking at equation 1.2, it is also apparent that $\mathbf{B} \cdot \boldsymbol{\nabla} p = 0$. This means that the magnetic surfaces must be surfaces of constant pressure. In addition, we

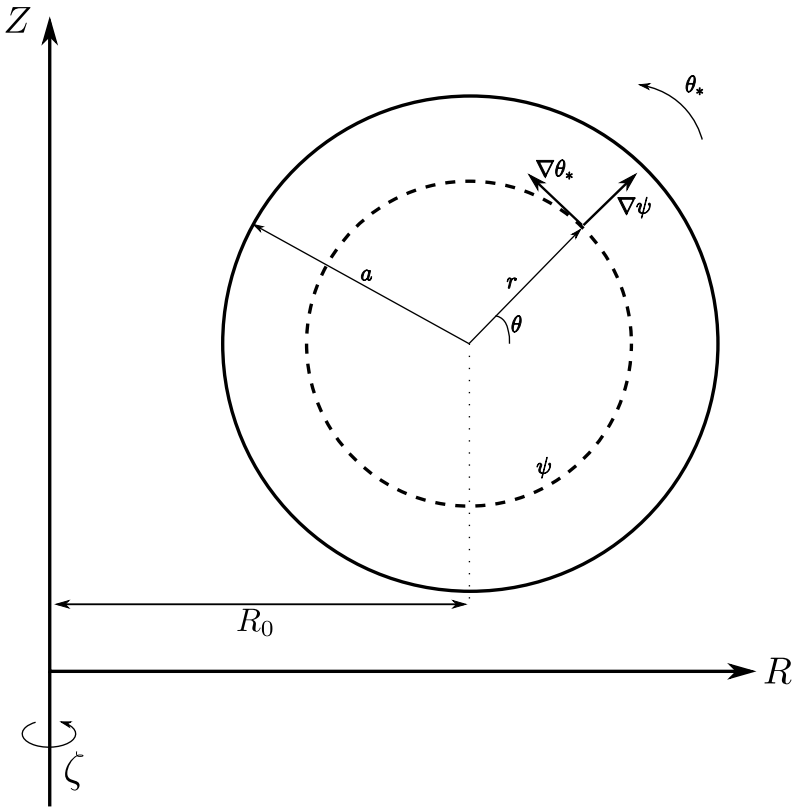

Figure 1.1: The set of co-ordinates used for the description of a tokamak in this thesis. Here, the dashed line represents an arbitrary flux surface.

can see that $\mathbf{J} \cdot \boldsymbol{\nabla} p = 0$ and the current lines must therefore also lie on the magnetic surfaces.

We can conclude from the symmetry between $\mathbf{J}$ and $\mathbf{B}$ that a poloidal current flux function F also exists, which is defined as

$$F = RB_t. \tag{1.5}$$

The safety factor is a value that represents how many times a magnetic field line travels around the tokamak toroidally for each time poloidally.

$$q = \frac{1}{2\pi} \int_0^{2\pi} \frac{\mathbf{B} \cdot \boldsymbol{\nabla} \zeta}{\mathbf{B} \cdot \boldsymbol{\nabla} \theta} \mathrm{d}\theta \tag{1.6}$$

As q will be constant on each magnetic surface, it too is a flux function.

The definitions of this coordinate system and the flux functions allow us to define an aximmetric magnetic field in its simplest form:

$$\mathbf{B} = F \boldsymbol{\nabla} \zeta + \boldsymbol{\nabla} \psi \times \boldsymbol{\nabla} \zeta. \tag{1.7}$$

Finally, we define the plasma β as a simple ratio used to represent the efficiency of confinement of the plasma pressure by the magnetic field,

$$\beta = \frac{p}{B^2/2\mu_0} \tag{1.8}$$

where the plasma pressure, $p = nT$. By necessity, $\beta < 1$ in a tokamak, as a β larger than one would mean the magnetic pressure was not enough to contain the plasma pressure exerted. β is typically a few percent.

1.4 Single Particle Motion

As mentioned previously, charged particles moving in a magnetic field exhibit helical paths around the magnetic field lines, which is shown in figure 1.2. This is a result of the interaction between the magnetic field and the component of velocity perpendicular to the magnetic field ($\mathrm{v}_\perp$). The parallel component of the velocity is unchanged, as is the kinetic energy of a particle, when in constant magnetic field and no electric field. The orbit of an ion has an ion gyroradius, also known as the Larmor radius, which given by

$$\rho_i = \frac{m_i v_\perp}{qB}$$

where m_i and q are the ion mass and charge respectively.

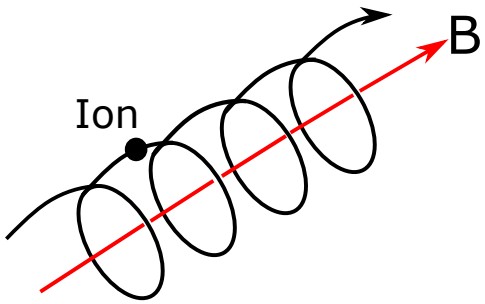

Figure 1.2: The particles exhibit a fast gyration around the magnetic field lines but also retain a parallel velocity along the field lines. The motion described by the movement of the centre of their gyrating orbit is known as the gyrocentre velocity.

An electric field parallel to the magnetic field ($E_{\|}$) or a magnetic field that changes strength along the field lines can accelerate a particle in the parallel direction. However, a force acting on the particle perpendicular to the magnetic field gives rise to a particle drift, which is perpendicular to both the force exerted and the magnetic field.

A simple way to picture the origin of this drift is that when the particle is moving in the same direction as the force ρ_i will increase (due to the acceleration of the particle), but when moving in the opposite direction ρ_i will decrease (due to the particle decelerating). This results in a net movement of the particle,

$$\mathbf{v}_D = \frac{\mathbf{F} \times \mathbf{b}}{qB} \tag{1.9}$$

where $\mathbf{b} = \mathbf{B}/B$.

In a tokamak, there are numerous drifts that can affect a charged particle. A perpindicular electric field will give rise to an $E \times B$ drift. Despite the force from an electric field being dependant on the charge of a particle, the resultant drift is independent of charge.

$$\mathbf{v}_{E\times B} = \frac{\mathbf{E} \times \mathbf{b}}{B} \tag{1.10}$$

It is also worth noting that this drift is independent of mass, and therefore an $E \times B$ drift will not lead a charge separation as may otherwise be expected. If the electric field is not constant in time however, a polarization drift will occur which can lead to a separation of charge.

$$\mathbf{v}_p = \frac{m}{qB^2}\frac{d\mathbf{E}}{dt} \tag{1.11}$$

If the magnetic field is not homogeneous, which it is not in a tokamak, two more

particle drifts arise. A particle moving along a curved magnetic field line will experience a centrifugal force acting outwards and this will give rise to a curvature drift. When the magnetic field strength is not constant the ∇B drift occurs. This is a result of the magnetic force exerted on the particle changing throughout its orbit. The two drifts together are given by

$$\mathbf{v}_d = \left(\frac{mv_\parallel}{qB} + \mu\right)\frac{\mathbf{b}\times\boldsymbol{\nabla}B}{B} \tag{1.12}$$

where the terms in brackets are related to the curvature and ∇B drifts respectively.

A mathematical derivation of these drifts in a gyrokinetic frame is shown later in chapter 2.

1.4.1 Trapped particles

When a particle moves into a higher magnetic field, in addition to the ∇B drift, it will experience a force that acts to reduce its parallel velocity. This force is a result of the conservation of the magnetic moment, μ, and energy, ϵ, of the particle.

$$\mu = \frac{mv_\perp^2}{qB} \qquad \epsilon = \frac{1}{2}mv_\parallel^2 + \mu B$$

Energy is a constant of motion, but magnetic moment is actually an adiabatic invariant. This means that it will remain constant as long as the magnetic field changes slowly.

As a particle moves into higher B, an increase in $v_\perp$ is observed. To account for this, and keep ϵ conserved, $v_\parallel$ must then decrease. This decelerating 'mirror force' is given by

$$F = -\mu\boldsymbol{\nabla}B$$

and may eventually cause $v_\parallel$ to reduce to zero, before reversing the parallel velocity altogether and causing the particle to move back from the direction it came. A tokamak has a varying magnetic field strength, approximately proportional to $1/R$, and a particle travelling from the low field (outboard) side into the high field (inboard) side must have a high enough parallel velocity to overcome this magnetic mirror effect. Whether or not a particle undergoes this velocity reversal can be described by the condition:

$$v_{\parallel 0} > \sqrt{\frac{2r}{R_0 - r}}v_{\perp 0} \tag{1.13}$$

where $v_{\parallel 0}$ and $v_{\perp 0}$ are the parallel and perpendicular velocity of the particle on the outboard side.

The particles that cannot reach the inboard side are known as trapped particles and display a banana orbit similar to that shown in figure 1.3. It can be seen that the particle does not follow the exact same path in each direction; the different signs of $v_{\|}$ cause different drifts which gives the particles orbit a finite width.

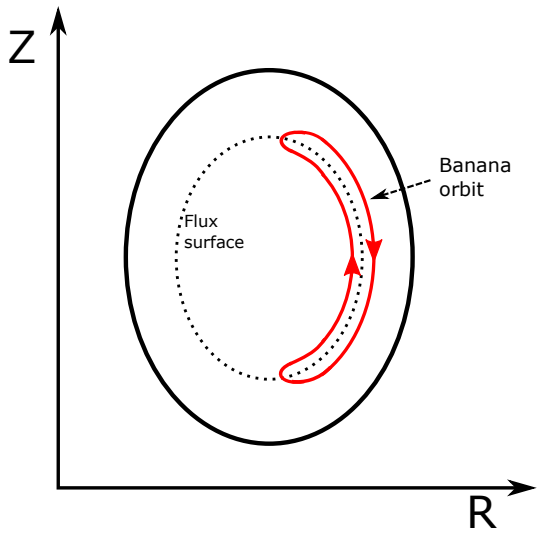

Figure 1.3: A trapped particle will not travel back along the same path, but will instead follow an orbit with a small width in the radial direction.

1.5 Tokamak Transport

1.5.1 Anomalous Transport and Turbulence

For a tokamak to achieve thermonuclear conditions, it is necessary to contain the plasma for a significant time period. As such, it is useful to gain estimates of the transport processes which are taking place within the tokamak. A neoclassical theory was developed as an attempt to describe the diffusion within the device which results from collisions [15].

The predictions made by the neoclassical model originally lead to a high optimism in regards to the ease with which nuclear fusion could be achieved and the plasma contained. However, actual experimental results have shown a large discrepancy between models and reality, with the levels of transport being clearly underestimated; the predictions sometimes differ from observations by orders of magnitude [16].

The transport that is not accounted for by the neoclassical model is known as anomalous transport, and it is now thought that it is caused by instabilities in

the plasma. Explanations of the anomalous transport remain one of the biggest challenges to theoretical tokamak physics.

Larger instabilities in a tokamak tend to affect the equilibria of the plasma itself. For a plasma in a stable equilibria it is therefore smaller scale 'microinstabilities' that are of importance.

1.5.2 Micro-instabilities

Micro-instabilities take the form of drift waves, which are collective plasma oscillations that arise in a magnetised plasma as a result of the interaction between the ions and electrons. A displacement of one species generates a field which acts to maintain the quasi-neutrality of the plasma and gives rise to the oscillations.

Drift wave micro-turbulence is widely believed to be driven by the 'free energy' provided by the density and temperature profile gradients. Dissipation, such as from particle collisions, often plays a critical role in the generation of instabilities, and these drift waves are known as dissipative. Reactive micro-instabilities on the other hand do not require dissipation[17].

The perpendicular wavelength of the drift waves is on the order of the gyroradius but the parallel wavelength is much longer, due to the lack of confinement along the magnetic field lines. This is a property that is also shared with the turbulence driven by the micro-instabilities. These drift waves tend to evolve relatively slowly, on a much longer time scale than the ion-cyclotron frequency of the plasma.

A simple example of a drift wave is derived here with the use of an ion fluid model with adiabatic electrons, although a review paper by Horton provides a more in-depth discussion of drift waves and transport [17]. The adiabatic electrons are assumed to have an instantaneous response to any variations in the electrostatic perturbation which result from a change of ion density. We consider an ion density perturbation in the presence of a 'radial' density gradient, $\boldsymbol{\nabla} n_0/n_0 = -(1/L_n)\mathbf{e}_x$, in a slab plasma. The plasma has a uniform and homogeneous magnetic field acting in the z-direction, $\mathbf{B} = B\mathbf{e}_z$ and cold ions, $T_i = 0$.

In this case, the ion mass continuity equation is given by

$$\frac{\partial n_i}{\partial t} + \boldsymbol{\nabla} \cdot (n_i \mathbf{v}) = 0 \tag{1.14}$$

where $\mathbf{v}$ is the ion fluid velocity, n_i is the ion density and $\boldsymbol{\nabla} \cdot [n_i v_{dia}] = 0$ in the slab limit. In this configuration, no magnetic drifts are present.

By assuming a small density perturbation ($\delta n_i \ll n_0$), equation 1.14 can be

linearised

$$n_i = n_0 + \delta n_i(\mathbf{x}, t) \tag{1.15}$$

with a time-independent density component, n_0, and the time-dependent perturbed density which can be represented by a plane wave solution

$$\delta n_i(\mathbf{x}, t) = \tilde{n}_i \exp\left(i\left[k_\parallel z + k_\perp y - \bar{\omega} t\right]\right) \tag{1.16}$$

where $\bar{\omega} = \omega + i\gamma$ may in general be complex, containing both a frequency, ω, and growth rate, γ. The equilibrium density n_0 will be constant over a flux surface ($\nabla_\parallel n_0 = 0$). Since the plasma should remain neutral, n_0 represents the unperturbed density for both ions and electrons.

The perturbed potential gives rise to an $E \times B$ velocity, for which we again assume a plane wave solution. The $E \times B$ velocity can be given by

$$\tilde{\mathbf{v}}_{E\times B} = \frac{\mathbf{b} \times \boldsymbol{\nabla}\phi}{B} = \frac{1}{B}\frac{\mathrm{d}\phi}{\mathrm{d}x}\mathbf{e}_y - \frac{1}{B}\frac{\mathrm{d}\phi}{\mathrm{d}y}\mathbf{e}_x = -i\frac{k_\perp \phi}{B}\mathbf{e}_x \tag{1.17}$$

for which ϕ represents the perturbed potential.

Substituting equations 1.16 and 1.17 into the ion mass continuity equation 1.14, we calculate

$$\frac{\partial \delta n_i}{\partial t} + \tilde{v}_{E\times Bx}\frac{\mathrm{d}n_i}{\mathrm{d}x} + n_i\frac{\partial \tilde{v}_\parallel}{\partial z} = 0 \tag{1.18}$$

which gives

$$\omega \delta n_i = \omega_* n_0 \frac{e\phi}{T_e} \tag{1.19}$$

for waves such that $\omega/k_\parallel << v_{Ti}$, so that the parallel ion motion is negligible. Here $\omega_* = k_\perp T_e/eBL_n$ is the diamagnetic frequency.

The equation for the parallel electron dynamics is derived later in section 2.8 and given in equation 2.91. The solution is found to be

$$n_e = n_0 \exp\left(\frac{e\phi}{T_e}\right) \tag{1.20}$$

and the Taylor expansion of this gives the "Boltzmann response":

$$\delta n_e = n_0 \frac{e\phi}{T_e}. \tag{1.21}$$

Finally, by imposing quasi-neutrality, $n_i = n_e$, the perturbed potential can be elim-

inated from equation 1.19 to give the frequency of the drift wave as

$$\omega = \omega_*. \tag{1.22}$$

As this is a purely real frequency it will only propagate and will not grow or decay with time. If a phase shift was introduced between the potential and density perturbations however, it would lead to the development of an exponentially growing mode.

It is important to note that in a tokamak, there are non-linear interactions between modes at competing scales which leads to turbulent saturation. This saturation causes the amplitude of each mode to peak and for further growth to cease. It is because of this that individual drift waves cannot be viewed in their linear form experimentally. It also means that the nonlinear physics must be included in simulations to provide a full description of the plasma behaviour.

The two different classes of particles in a tokamak, the passing and trapped particles, behave differently under an electrostatic potential perturbation. This leads to different dispersion relations being obtained depending on whether trapped or passing particle dynamics are important. This also leads to two different categories of instability, passing and trapped particle instabilities.

Perturbations may be Fourier tranformed in the poloidal and toroidal directions with mode numbers m and n labelling the found poloidal and toroidal modes respectively. This form of the Fourier analysed modes are often used to discuss the various micro-instabilities present in a tokamak.

Many varieties of drift waves exist, but in this section the focus will be on the two reactive drift waves which are known to be the most important in determining transport under typical tokamak operating conditions. These are the Ion Temperature Gradient (ITG) mode and the Trapped Electron Mode (TEM). Zonal flows, which play an important part in turbulence regulation, are also discussed.

Ion Temperature Gradient (ITG) mode

Several different branches of the ITG mode exist: slab, impurity and toroidal but the focus in this section is placed on the mode with the most relevance in tokamaks; the toroidal ITG mode. A simple description is presented here of the linear mechanisms, but there are numerous articles that give more in-depth explanations and derivations [17, 18].

The ITG mode is considered to be the dominant mode transport mechanism in a large aspect ratio tokamak. As its name suggests, the ITG mode is driven by

the ion temperature gradient.

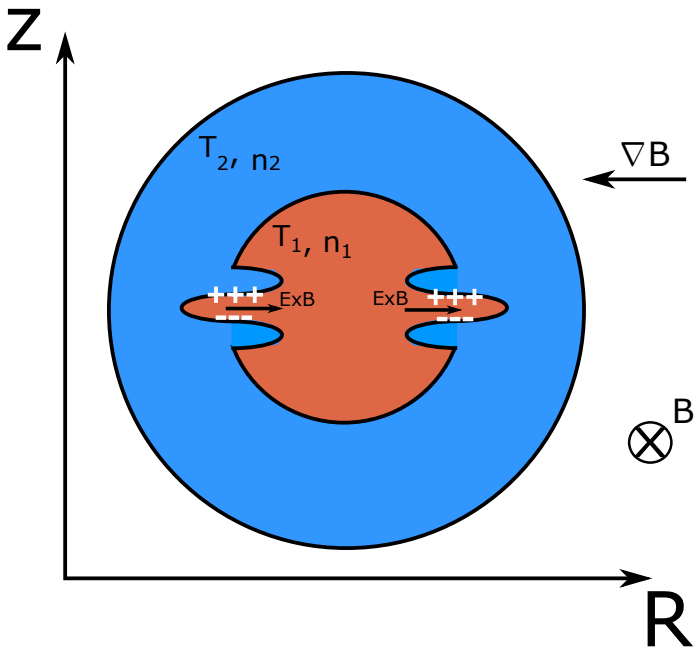

Figure 1.4: A simple picture of the ITG mode can be developed by considering a poloidal cross-section which has a hot, dense region and cool, lower pressure region. A small temperature perturbation is then introduced between the two regions. $T_1 > T_2$ and $n_1 > n_2$.

A simple picture of the ITG mode can be formed by considering a poloidal tokamak cross section, as shown in figure 1.4, which has a hot, dense inner core and a cooler, lower pressure outer region [19]. We consider a perturbation in the ion temperature, radially elongated on the low-field side of the tokamak. As the curvature and grad-B drifts are proportional to the velocity of each particle, we expect that the net drift in the hotter ion region would be larger than the drift in the cooler ion region. This variation of drifts will in turn result in a build up of ions on the edge of the hot (positive) side of the temperature perturbation and a deficit of ions on the edge of the cool (negative) side of the perturbation which is $\pi/2$ out of phase with the initial temperature perturbation. As the electrons move to balance the density and maintain the quasi-neutrality of the plasma, an electrostatic potential perturbation results which is in phase with the density perturbation (for instantaneously reacting adiabatic electrons).

This electrostatic potential perturbation will result in an $E \times B$ drift which acts to pull hot plasma into the hotter regions of the temperature perturbation and cooler plasma into the cooler region of the temperature perturbation. This results

in feedback loop which enhances the initial temperature perturbation, and causes an exponential growth.

While this growing perturbation forms on the outboard side of the tokamak, ∇B has the opposite sign on the inboard side of the tokamak and the drifts instead cause the instability to be suppressed. This leads to the inboard side sometimes being referred to as the "good curvature" region and the outboard side being referred to as the "bad curvature" region.

The time averaged radial particle flux generated by the perturbation is given by

$$P_i = \langle\langle n_i \mathbf{v}_{fluid} \cdot \mathbf{e}_r \rangle\rangle = \langle\langle \delta\tilde{n}_i \tilde{v}_E \cdot \mathbf{e}_r \rangle\rangle \tag{1.23}$$

and will always be zero for systems with adiabatic electrons, as there is no phase difference between $\delta\tilde{n}$ and $\tilde{\phi}$ (the time averaged value $\langle\langle ... \rangle\rangle$ is zero for a single fluctuating quantity). However, if the electrons were not adiabatic (kinetic electrons were used) then it would be possible for a phase difference to occur between these two quantities.

However, the time averaged heat flux

$$Q_i = \langle\langle \tilde{T}_i \tilde{v}_E \cdot \mathbf{e}_r \rangle\rangle \tag{1.24}$$

will be nonzero because of the phase difference between $\tilde{T}_i$ and $\tilde{\phi}$. This instability is therefore known to transport heat along the temperature gradient.

The ion fluid model serves well to discuss the underlying mechanism which describes the ITG mode, but it can be further expanded by taking into account the effects of the finite size of the Larmor radius; which would be included in a kinetic approach. The finite size of the gyro-radius means that the particles only feel the gyro-averaged electrostatic potential with scales smaller the the gyro-radius. This results in a suppression of modes with $k_\theta \rho_i \ll 1$.

Trapped Electron Mode (TEM)

Due to the trapping condition outlined in equation 1.13, a fraction of the electrons always remain on the low-field side of their flux surface. These trapped electrons have a bounce frequency

$$\omega_{Be} = v_\parallel \frac{\sqrt{\varepsilon/2}}{qR_0} \tag{1.25}$$

where ε is the fraction of trapped particles. Unlike the passing electrons, the trapped electrons have their parallel velocity restricted by this confinement. For drift waves with $\omega \ll \omega_{Be}$, the trapped electrons do not contribute to the parallel dynamics that

determine quasi-neutrality. When averaged over their bounce orbits, these trapped particles have no parallel motion and the trapped electrons no longer respond instantaneously to electrostatic perturbations.

Therefore, the dynamics of the trapped electrons have a resemblance to the passing ions, and as a result a TEM exists similarly to the ITG mode. This TEM is driven by the gradient of the electron temperature profile. In the TEM, the trapped particles play a role similar to the ions in the ITG and the passing electrons provide the parallel dynamics. As this instability relies on the movement of the electrons, it will only be apparent when considering kinetic electrons, and will be absent with adiabatic electrons.

Zonal Flows

Zonal flows are axisymmetric $n = 0, m = 0$ electrostatic potential perturbations that have a finite radial wavenumber k_r. They are thought to be one of the most important physical processes that play a role in determining the saturation levels of micro-turbulence [20, 21]. It is not possible for zonal flows to drive $E \times B$ perturbations as they are $n = 0$ modes and therefore they cannot drive radial transport. As a result, they cannot tap the free energy sources that other modes use such as the temperature gradient ∇T or density gradient ∇n. Zonal flows must therefore be driven by non-linear interactions; they are excited by drift waves (more generally micro-instabilities).

Zonal flows play an important role in the regulation of turbulence and transport in a tokamak by shearing the drift waves of the system and also extracting energy from them, which contributes a large part to the saturation that is seen in a non-linear simulations. As zonal flows are $n = 0$, $k_{\|} = 0$ modes they are not subject to Landau damping.

1.6 Outline

The main aim of this thesis is to study the effects of a strongly rotating plasma on transport with the use of a gyrokinetic model. All simulations performed used the global gyrokinetic code ORB5. The first chapter of this thesis introduced some of the broader information that is relevant to the study of turbulence and transport in a tokamak.

Chapter 2 introduces the gyrokinetic model which was originally derived by Hahm [22, 23]. The weak-flow form was initially used in ORB5, but work completed as part of this thesis extended the gyrokinetic model to allow more accurate study of

strong-flow simulations. Chapter 3 moves on to introduce ORB5, covering many of the more important aspects of the code and also discusses some of the modifications that were made to the equations of motion and the equilibrium distribution function; this includes mention of testing processes which were used to ensure the code still worked as intended.

Chapters 4 and 5 feature a series of linear simulations using this strong-flow version of ORB5, first investigating GAM eigenmodes and the change of GAM frequency that occurs in a rotating plasma and then moving on, in chapter 5, to study the micro-instabilities of the system under a toroidal rotation.

Finally, in chapter 6 this work is built upon in a set of non-linear simulations with varying rates of rotation.

All applied rotation profiles discussed are solid body rotations as the focus has been on the centrifugal and Coriolis effects and not on shearing.

Chapter 2

Gyrokinetics

2.1 Introduction

The two main methods of describing the motion of particles in a plasma and the behaviour of the plasma are the fluid and kinetic approaches. While the fluid approach describes the plasma by modelling each species as a fluid with quantities derived by taking velocity moments of the particles, the kinetic approach considers the dynamics of each particle composing the plasma [13].

A kinetic theory provides the most thorough description of plasma. However, due to the high number of particles in a plasma this would require solving a very large N-body system and thus the description must take a statistical approach. The change from a description of N particles to a single particle distribution function can be achieved through the use of the BBGKY hierarchy [24, 25]. This is implemented by describing each plasma species with distribution function $f_s(\mathbf{x}, \mathbf{v}, t)$, which gives the probability density of a particle being found at position $\mathbf{x}$ and with velocity $\mathbf{v}$.

The electromagnetic fields must be computed self-consistently with Maxwell's equations, which involve a charge density and current

$$\rho = \sum_s q_s \int f_s(\mathbf{x}, \mathbf{v}, t) d\mathbf{v} \tag{2.1}$$

$$\mathbf{J} = \sum_s q_s \int \mathbf{v} f_s(\mathbf{x}, \mathbf{v}, t) d\mathbf{v} \tag{2.2}$$

where the subscript s is used to label particle species.

With the use of Liouville's theorem, it is possible to create a continuity equation for the distribution function, which mathematically states that the flow out of a closed volume of phase space is equal to the rate of change of the particle

distribution function. The time evolution of the particle distribution functions can then be described by

$$\frac{\mathrm{d}f_s}{\mathrm{d}t} = \frac{\partial f_s}{\partial t} + \frac{\mathrm{d}\mathbf{x}}{\mathrm{d}t} \cdot \boldsymbol{\nabla} f_s + \frac{\mathrm{d}\mathbf{v}}{\mathrm{d}t} \cdot \frac{\partial f_s}{\partial \mathbf{v}} = 0 \tag{2.3}$$

where the total derivative with respect to time has been expanded using the chain rule. This is known as the Vlasov equation and it describes the behaviour of particles in the absence of any particle (or heat) sources and sinks and in a collisionless system. It is possible to modify the Vlasov equation with the inclusion of a collisional term $(\partial f/\partial t)_c$ on the right hand side of equation 2.3. This collisional kinetic equation for a plasma is known as the Fokker-Planck equation [26]. The Vlasov (or Fokker-Planck) equation is extremely important in a kinetic theory as it describes the evolution of the particle distribution function in time $\mathrm{d}f_s/\mathrm{d}t$, which in turn is used to evolve the particles represented by the distribution function.

One of the main issues that motivates the transition from a kinetic to gyrokinetic approach is the large range of spatial and temporal scales found in a tokamak. The size of the micro-instabilities are typically of the order of the Larmor radius, $\rho_i \sim 10^{-3}$m, while the size of the tokamak is of order 1m. Additionally, the frequencies of the micro-instabilities are typically of the order of the drift frequencies, $\omega \sim 10^6 s^{-1}$, but the cylotron frequency of the ions (electrons) is $\Omega \sim 10^8 (10^{11}) s^{-1}$. Furthermore, the transport time scale is $\sim 1s$. Gyrokinetics takes advantage of this separation of scales.

As the gyrofrequency is much higher than the main physics of interest, the effects of gyration can be treated in a time-averaged fashion. Equations and distribution functions then follow the guiding centre of the particles instead of their actual position and the problem effectively reduces to a five dimensional one in phase space, three in physical space and two in velocity; which is a less computationally expensive problem to solve.

There are multiple approaches that may be used to find a set of gyrokinetic equations. A sensible approach may be to gyro-average the Vlasov equations, as shown by Frieman and Chen [27]. Unfortunately, this method does not conserve energy. A Lagrangian or Hamiltonian approach is therefore better, as it should automatically satisfy several conservation properties; such as for energy and momentum. This Lagrangian approach [22] forms the basis of modern gyrokinetic theory and codes.

2.2 Plasma Rotation

When neutral beams (with a toroidal component of velocity) are injected into the plasma of a tokamak, the momentum of the neutral particles is transferred into the plasma which causes a net toroidal rotation around the tokamak. There are other ways of 'spinning up' a plasma, such as through ion cyclotron waves, but the resulting rotation is much smaller. Some level of rotation intrinsic to the system is also possible, which can originate from momentum transport and profile shearing. Such rotation has recently been observed experimentally [28]. Therefore, even simulations of 'non-rotating' plasmas in this thesis (that is plasmas that have not had an external momentum source) may show some level of toroidal rotation in simulations. For future experiments, such as ITER, the intrinsic rotation of the system may out-weigh the rotation added by an external momentum source. Neoclassical collision mechanisms tend to damp strong poloidal flows and as such, in the absence of a direct driving force poloidal flows in a tokamak are typically small and of a lower order than the toroidal flows [29, 30]. For this reason, poloidal rotation has been neglected from investigation in this thesis .

As would be expected for a rotating object, the particles in a toroidally rotating plasma undergo a centrifugal effect which results in a density shift of particles towards the outboard side of the tokamak. This introduces a poloidally varying density along the flux surfaces [26].

Toroidal rotation can often be thought of as two components. One is a parallel flow, an additional contribution to velocity along the field lines, and the other a background $E \times B$ velocity, u_E, perpendicular to the field lines but still on the flux surface. The toroidal rotation will have a related background potential Φ which is the electrostatic potential that generates u_E. The poloidal components of the parallel flow and u_E caused by the background potential approximately cancel.

If the background electrostatic potential is assumed to only vary radially (an approximation used throughout this thesis), the background $E \times B$ velocity has magnitude given by

$$u_E = \left(\frac{\partial \Phi}{\partial \psi}\right) \frac{|\nabla \psi|}{B}$$

and has direction perpendicular to the field lines but still on the flux surfaces. We can calculate the size of u_E compared to the toroidal velocity

$$\frac{u_E}{v_{tor}} = \left\{ \frac{\partial \Phi}{\partial \psi} \frac{|\nabla \psi|}{B} \right\} \Big/ \left\{ \frac{\partial \Phi}{\partial \psi} R \right\} = \frac{B_p}{B} \tag{2.4}$$

where the toroidal velocity is given by $v_{tor}^2 = \Omega_t^2 R^2$ and $B_p = |\nabla \psi|/R$. Ω_t is used

to represent the toroidal rotation rate. The background $E \times B$ flow is therefore dependent upon the rate of toroidal rotation as well as the pitch angle of the magnetic field. For a system with a higher pitch angle, such as a spherical tokamak, the relative size of u_E would be expected to be greater than in a large aspect ratio tokamak.

In large aspect ratio tokamaks, such as JET, the deuterium Mach number describing toroidal velocity is typically observed to be below 0.3, and as such the rotational effects upon the plasma were not originally included in the gyrokinetic equations used to model turbulence. However, recent interest has increased with the observations of spontaneous toroidal rotation in tokamaks in the absence of an external momentum source [28]. Experimental observations have been made of toroidal rotation in beam heated conventional aspect ratio devices which show toroidal velocities with Mach numbers as high as 0.7 [31]. It has also long been known that spherical tokamaks exhibit deuterium Mach numbers of order unity [32]. Therefore, an effort has been made to study the transport properties of tokamaks which contain these strong flows [33].

Previous studies have derived gyrokinetic equations which describe the centrifugal and Coriolis effects observed in a co-moving frame [34] and have since been used in the local gyrokinetic code GKW to investigate strong rotations [35, 36]. However, studies have not yet been performed which include strong flow gyrokinetic equations in a global code.

2.3 Gyrokinetic ordering

Several small parameters are required to derive a gyrokinetic theory. Within the gyrokinetic orderings in this thesis the background profile quantities are represented by n, T and Φ for density, temperature and electric potential respectively while the small fluctuations related to micro-instabilities are represented as δn and $\delta\phi$ for density and electrostatic potential perturbations respectively. More in depth discussion of the ordering and other aspects of gyrokinetic theory can be found in an article by Brizard [37].

The first ordering term is related to the ratio of frequency of the micro-instabilities in the tokamak and the cyclotron frequency, defining a small parameter, ϵ_ω,

$$\frac{\omega}{\Omega_{ci}} \sim \epsilon_\omega \ll 1 \tag{2.5}$$

which represents the fundamental assumption of gyrokinetics: that the frequency of the micro-instability ω is much smaller than the ion cyclotron frequency Ω_{ci}.

There are also orderings related to the size of the components of the wave vector parallel, $k_\parallel$, and perpendicular, $k_\perp$, to the magnetic field.

$$\frac{k_\parallel}{k_\perp} \ll 1 \tag{2.6}$$

This states that the turbulence is assumed to largely align with the magnetic field lines. In addition,

$$k_\perp \rho_i \sim 1. \tag{2.7}$$

We must also separate out the spatial scales. This is possible if the gradient scale length of the magnetic field is much longer than the Larmor radius,

$$\frac{\rho_i}{L_B} \sim \epsilon_B \ll 1 \tag{2.8}$$

where $L_B = |\boldsymbol{\nabla} B/B|$. L_B is assumed to be of order of the major radius.

The amplitude of electrostatic field perturbations are required to be substantially smaller than the magnitude of the temperature

$$\frac{e\delta\phi}{T} \sim \epsilon_\delta \ll 1. \tag{2.9}$$

Although fluctuations of the electrostatic potential are rarely measured in the interior of a tokamak experimentally, estimates suggest that in a typical tokamak $e\delta\phi/T_e \sim \delta n/n_0$ [37]. The variation of $\delta n/n_0$ within a tokamak has been measured experimentally to vary from below 1% at the core up to 10% at the edge [38].

Often, the $E \times B$ background velocity of the system is assumed to be small in comparison to the thermal velocity, $u_E/v_{Ti} \sim \epsilon_B$, which was an important assumption made in the original derivation of Hahm's gyrokinetic equations [22].

If all these orderings are met, then Hahm's gyrokinetic equations for drift-wave turbulence in a tokamak can be utilised. Although it is not required, the three small parameters are taken to be approximately equal in Hamh's formalism.

$$\epsilon_\omega \sim \epsilon_B \sim \epsilon_\delta \sim \epsilon \tag{2.10}$$

Hahm also introduces a new small ordering parameter, $\delta_B \equiv B_\theta/B$, which is only applied at the end of his derivation. This new ordering is more relevant to tokamak core transport barriers, and simplifies the equations of motion for the purposes of gyrokinetic simulations [23]. The ordering of the electrostatic fluctuations

becomes

$$\frac{e\delta\phi}{T} \sim \epsilon\delta_B \ll 1 \tag{2.11}$$

and the distribution function is also given the ordering

$$\frac{\delta f}{f} \sim \epsilon\delta_B \tag{2.12}$$

where the distribution function has been split into a background and perturbed component, $f = f_0 + \delta f$.

2.3.1 Toroidally rotating plasma

The ordering of u_E given above is invalid in the presence of a strong radial electric field, and therefore also in the case of a fast toroidally rotating plasma.

The $E \times B$ velocity is usually assumed to be of the order of the diamagnetic velocity and therefore negligibly small, but the derivations made in a later article by Hahm relaxed this assumption and for generality u_E was allowed to be of the same order as the thermal velocity [23].

$$\frac{u_E}{v_{ti}} \sim 1 \tag{2.13}$$

2.4 Gyrokinetic Lagrangian

The gyrokinetic equations derived here are done so using the phase-space Lagrangian variation method and Lie perturbation theory [39, 40]. The advantage of this method is that it ensures the conservation properties are preserved throughout the transformation between real space and gyro-centre space. The particle Lagrangian is first calculated in real space, and our derivation then follows on to use two changes of coordinate system. The first is from real space $(\mathbf{x}, \mathbf{v}, t)$ into guiding-centre space $(\mathbf{R}, v_\parallel, \mu, \alpha, t)$ for which the coordinate system is shown in figure 2.1. The next transformation is from the guiding-centre frame into the gyro-centre frame, $(\bar{\mathbf{R}}, \bar{v}_\parallel, \bar{\mu}, t)$. The difference between the guiding and gyro frames is the inclusion of perturbed fields. These perturbed fields break the conservation of μ, and so a new coordinate $\bar{\mu}$ is used instead in the gyro-centre frame. Usually, these derivations only need to be performed up to the second order.

The Einstein notation is used in this section, where a summation over the indices is implied by pairs of repeated indices. In addition, i and j are used to represent an index spanning only the spatial dimensions while the greek letters, σ and ν represent indices over the spatial and temporal dimensions.

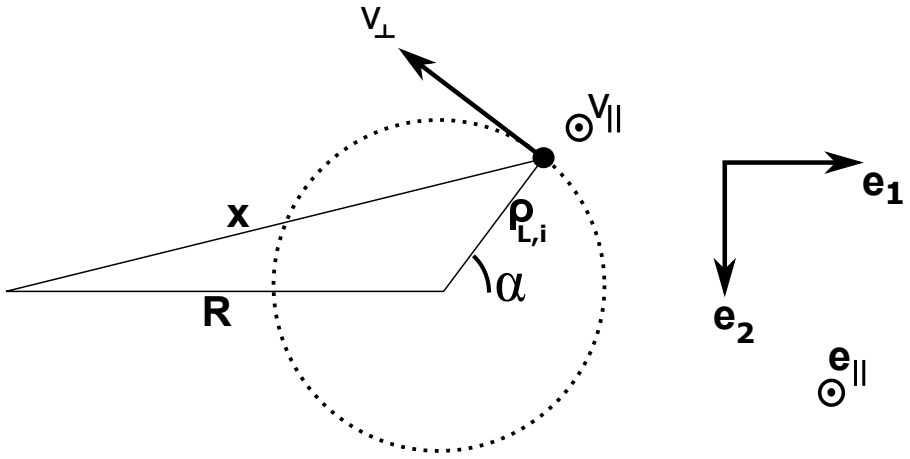

Figure 2.1: The gyro-centre coordinates are shown. **R** is the position vector of the guiding center of the ions, which the ions orbit with gyroradius $\rho_{L,i}$. The gyrophase angle α describes the position of the ion in its gyro-orbit.

2.4.1 The unperturbed phase-space Lagrangian

For a single particle, the Euler-Lagrange equation is

$$\frac{\mathrm{d}}{\mathrm{d}t}\left(\frac{\partial \mathcal{L}}{\partial \dot{q}_i}\right) - \frac{\partial \mathcal{L}}{\partial q_i} = 0 \tag{2.14}$$

where $(\mathbf{q}, \mathbf{p})$ are canonical variables. The Lagrangian is given by

$$\mathcal{L} = \mathbf{p} \cdot \dot{\mathbf{q}} - H_c(\mathbf{q}, \mathbf{p}, t) \tag{2.15}$$

and H_c is the canonical Hamiltonian. The Lagrangian can also be rewritten in an arbitrary coordinate system of phase space, $\mathbf{z} = \mathbf{z}(\mathbf{q}, \mathbf{p}, t)$, via the use of the chain rule:

$$\mathcal{L} = \gamma_i \dot{z}_i - H. \tag{2.16}$$

with

$$\gamma_i = \mathbf{p} \cdot \frac{\partial \dot{\mathbf{q}}}{\partial z_i}$$

$$H = H_c - \mathbf{p} \cdot \frac{\partial \mathbf{q}}{\partial t}.$$

By introducing the fundamental Poincaré-Cartan one-form, the covariance of this formulation becomes more apparent.

$$\gamma \equiv \mathcal{L}\mathrm{d}t = \gamma_i \mathrm{d}z^i - H\mathrm{d}t \equiv \gamma_\sigma \mathrm{d}z^\sigma \tag{2.17}$$

This covariance implies that for a coordinate transformation,we have:

$$\gamma = \gamma_\sigma \mathrm{d}z^\sigma = \Gamma_\sigma \mathrm{d}Z^\sigma \tag{2.18}$$

where

$$\Gamma_\sigma = \gamma_\nu \frac{\partial z^\nu}{\partial Z^\sigma}. \tag{2.19}$$

We can then form the Euler-Lagrange equation

$$\left(\frac{\partial \gamma_j}{\partial z^i} - \frac{\partial \gamma_i}{\partial z^j}\right)\frac{\mathrm{d}z^j}{\mathrm{d}t} = \hat{\omega}_{ij}\frac{\mathrm{d}z^j}{dt} = \frac{\partial H}{\partial z^i} + \frac{\partial \gamma_i}{\partial t} \tag{2.20}$$

where $\hat{\omega}_{ij}$ are components of a Lagrangian tensor.

Note that the Euler-Lagrange equations are invariant under a gauge transformation in phase space, which will be used later to simplify the one-form.

$$\gamma = \gamma + \mathrm{d}\mathbf{S} \qquad \forall \quad \mathbf{S}(\mathbf{z}) \tag{2.21}$$

The canonical single particle Hamiltonian in an arbritrary electromagnetic field is

$$H(\mathbf{q},\mathbf{p},t) = \frac{1}{2m}\left[\mathbf{p} - Ze\mathbf{A}(\mathbf{q})\right]^2 + Ze\phi(\mathbf{q},t), \tag{2.22}$$

where $\mathbf{A}$ is the vector magnetic potential related to the magnetic field as $\mathbf{B} = \boldsymbol{\nabla}\times\mathbf{A}$ and ϕ is an electrostatic potential.

Using the transformation

$$\mathbf{x} = \mathbf{q}$$

$$\mathbf{v} = \frac{1}{m}\left(\mathbf{p} - q\mathbf{A}\right)$$

and rewriting the charge of the particle with $q = Ze$, we then find the new one-form.

$$\begin{aligned}\gamma &= \gamma_i \mathrm{d}z^i - H\mathrm{d}t \\ &= \left[q\mathbf{A}(\mathbf{x}) + m\mathbf{v}\right]\cdot\mathrm{d}\mathbf{x} - \frac{1}{2}mv^2\mathrm{d}t - q\phi(\mathbf{x},t)\mathrm{d}t\end{aligned} \tag{2.23}$$

which can be broken into an unperturbed, γ_0, and a perturbed, γ_1, component.

$$\gamma_0 = \left[q\mathbf{A}(\mathbf{x}) + m\mathbf{v}\right]\cdot\mathrm{d}\mathbf{x} - \left(\frac{1}{2}mv^2 + q\Phi(\mathbf{x},t)\right)\mathrm{d}t \tag{2.24}$$

$$\gamma_1 = -q\delta\phi(\mathbf{x},t)\mathrm{d}t \tag{2.25}$$

$\delta\phi(\mathbf{x},t)$ represents the perturbed part of the electric potential and $\Phi(\mathbf{x},t)$ the

background electric potential. The goal is to now find a transformation and gauge that can be used to remove the oscillatory parts of the Lagragian to the lowest order. This begins with a transformation into a gyro-centre frame.

2.4.2 The gyro-center phase-space Lagrangian

The gyro-centre phase space Lagrangian can be derived, starting from the unperturbed phase-space Lagrangian, with the use of the Lie perturbation formalism as described by Brizard [41, 42] and Littlejohn [43]. Under the conditions that the gyrokinetic ordering depicted in equation 2.5 is valid, we may say that

$$\mathbf{x} = \mathbf{R} + \epsilon \boldsymbol{\rho}_{L,i}(\mathbf{R}, \alpha) = \mathbf{R} + \epsilon \frac{v_\perp}{\Omega_{ci}} \hat{\mathbf{a}} \tag{2.26}$$

$$\mu = \frac{m v_\perp^2}{2B} \tag{2.27}$$

$$\mathbf{v} = v_\parallel \mathbf{b} + v_\perp \hat{\mathbf{c}} + \mathbf{u}_E \tag{2.28}$$

$$\alpha = \cos^{-1}\left(-\frac{(\mathbf{v} - \mathbf{u}_E) \cdot \hat{\mathbf{e}}_2}{v_\perp} \right) \tag{2.29}$$

$$\mathbf{u}_E = -\frac{1}{B} \mathbf{b} \times \boldsymbol{\nabla} \Phi \tag{2.30}$$

where $v_\parallel$ and $v_\perp$ are the velocity parallel and perpendicular to the magnetic field respectively, Ω_{ci} is the ion cyclotron frequency and

$$\hat{\mathbf{a}} = \cos\alpha \hat{\mathbf{e}}_\mathbf{1} - \sin\alpha \hat{\mathbf{e}}_\mathbf{2}$$

$$\hat{\mathbf{c}} = -\sin\alpha \hat{\mathbf{e}}_\mathbf{1} - \cos\alpha \hat{\mathbf{e}}_\mathbf{2}.$$

Here, $\hat{\mathbf{e}}_\mathbf{1}$ and $\hat{\mathbf{e}}_\mathbf{2}$ are two arbitrary orthogonal unit vectors in the plane perpendicular to magnetic field as depicted in figure 2.1. The vector $\mathbf{R}$ represents the guiding-centre coordinates of the particle and α is the gyro-angle of the particle. We also introduce a small ordering parameter, ϵ, which will be set to 1 at the end of the calculations but is useful for visualizing the relative order of terms in the equations.

$\mathbf{A}(\mathbf{x})$ and $\Phi(\mathbf{x})$ can be expanded about the gyrocentre variable, $\mathbf{R}$, by using equation 2.26.

$$\mathbf{A}(\mathbf{x}) = \mathbf{A}(\mathbf{R}) + \epsilon \frac{v_\perp}{\Omega_{ci}} \hat{\mathbf{a}} \cdot \boldsymbol{\nabla} \mathbf{A}(\mathbf{R}) + \mathcal{O}(\epsilon^2) \tag{2.31}$$

$$\Phi(\mathbf{x}) = \Phi(\mathbf{R}) + \epsilon \frac{v_\perp}{\Omega_{ci}} \hat{\mathbf{a}} \cdot \boldsymbol{\nabla} \boldsymbol{\Phi}(\mathbf{R}) + \mathcal{O}(\epsilon^2). \tag{2.32}$$

$$\mathrm{d}\mathbf{x} = \mathrm{d}\mathbf{R} + \epsilon \frac{1}{\Omega_{ci}} \hat{\mathbf{a}} \mathrm{d}v_\perp + \epsilon \frac{v_\perp}{\Omega_{ci}} \mathrm{d}\hat{\mathbf{a}} + \mathcal{O}(\epsilon^2) \tag{2.33}$$

Here, the d$\mathbf{B}$ term that would appear in equation 2.33 may be considered low order due to the gyrokinetic ordering depicted in equation 2.8.

By substituting equations 2.31, 2.32 and 2.33 into equation 2.24 we can move the one-form Lagrangian into guiding centre coordinates.

$$\begin{aligned}\gamma_0 = &\left(\frac{1}{\epsilon}q\mathbf{A}(\mathbf{R}) + q\frac{v_\perp}{\Omega_{ci}}\hat{\mathbf{a}}\cdot\boldsymbol{\nabla}\mathbf{A}(\mathbf{R}) + m\mathbf{v} + \mathcal{O}(\epsilon)\right)\cdot\left(\mathrm{d}\mathbf{R} + \epsilon\frac{1}{\Omega_{ci}}\hat{\mathbf{a}}\mathrm{d}v_\perp\right.\\ &\left.+\epsilon\frac{v_\perp}{\Omega_{ci}}\mathrm{d}\hat{\mathbf{a}} + \mathcal{O}(\epsilon^2)\right) - \left(\frac{1}{2}mv^2 + \frac{1}{\epsilon}q\Phi(\mathbf{R}) + \frac{v_\perp}{\Omega_{ci}}\hat{\mathbf{a}}\cdot\boldsymbol{\nabla}\boldsymbol{\Phi}(\mathbf{R}) + \mathcal{O}(\epsilon)\right)\mathrm{d}t\end{aligned} \tag{2.34}$$

However, the one-form given by equation 2.34 still contains dependencies on the gyro-angle, α. To begin removing these we take advantage of the gauge invariance of the Euler-Lagrange equation previously noted.

$$S_1 = -\frac{qv_\perp}{\Omega_{ci}}\hat{\mathbf{a}}\cdot\mathbf{A} - \epsilon\frac{1}{2}\frac{qv_\perp^2}{\Omega_{ci}^2}(\hat{\mathbf{a}}\cdot\boldsymbol{\nabla}\mathbf{A})\cdot\hat{\mathbf{a}} \tag{2.35}$$

$$\begin{aligned}\mathrm{d}S_1 = &-\frac{q}{\Omega_{ci}}(\hat{\mathbf{a}}\cdot\mathbf{A})\,\mathrm{d}v_\perp - \frac{qv_\perp}{\Omega_{ci}}(\mathbf{A}\cdot\mathrm{d}\hat{\mathbf{a}}) - \frac{qv_\perp}{\Omega_{ci}}(\hat{\mathbf{a}}\cdot\mathrm{d}\mathbf{A})\\ &-\epsilon\frac{1}{2}\frac{qv_\perp^2}{\Omega_{ci}^2}[(\mathrm{d}\hat{\mathbf{a}}\cdot\boldsymbol{\nabla}\mathbf{A})\cdot\hat{\mathbf{a}} + (\hat{\mathbf{a}}\cdot\boldsymbol{\nabla}\mathbf{A})\cdot\mathrm{d}\hat{\mathbf{a}}]\\ &-\epsilon\frac{qv_\perp}{\Omega_{ci}^2}(\hat{\mathbf{a}}\cdot\boldsymbol{\nabla}\mathbf{A})\cdot\hat{\mathbf{a}}\mathrm{d}v_\perp + \mathcal{O}(\epsilon^2)\end{aligned} \tag{2.36}$$

Where once again the ordering of the magnetic field gradient scale length is used. Adding equation 2.36 to equation 2.34 allows us to simplify the one-form.

$$\begin{aligned}\gamma_0 + \mathrm{d}S_1 = &\left(\frac{1}{\epsilon}q\mathbf{A} + mv_\parallel\mathbf{b} + m\mathbf{u}_E + \mathcal{O}(\epsilon)\right)\cdot\mathrm{d}\mathbf{R} + \epsilon\frac{m}{\Omega_{ci}}\mathbf{v}\cdot\hat{\mathbf{a}}\mathrm{d}v_\perp\\ &+\epsilon\frac{mv_\perp}{\Omega_{ci}}\mathbf{v}\cdot\mathrm{d}\hat{\mathbf{a}} + \epsilon\frac{1}{2}\frac{qv_\perp^2}{\Omega_{ci}^2}[(\hat{\mathbf{a}}\cdot\boldsymbol{\nabla}\mathbf{A})\cdot\mathrm{d}\hat{\mathbf{a}} - (\mathrm{d}\hat{\mathbf{a}}\cdot\boldsymbol{\nabla}\mathbf{A})\cdot\hat{\mathbf{a}}]\\ &-\left(\frac{1}{2}mv^2 + \frac{1}{\epsilon}q\Phi(\mathbf{R}) + \frac{v_\perp}{\Omega_{ci}}\hat{\mathbf{a}}\cdot\boldsymbol{\nabla}\boldsymbol{\Phi}(\mathbf{R}) + \mathcal{O}(\epsilon)\right)\mathrm{d}t + \mathcal{O}(\epsilon^2)\end{aligned} \tag{2.37}$$

Next, we expand $\mathbf{v}\cdot\hat{\mathbf{a}}$, $\mathbf{v}\cdot\hat{\mathbf{c}}$ and v^2 as well as calculating

$$(\hat{\mathbf{a}}\cdot\boldsymbol{\nabla}\mathbf{A})\cdot\mathrm{d}\hat{\mathbf{a}} - (\mathrm{d}\hat{\mathbf{a}}\cdot\boldsymbol{\nabla}\mathbf{A})\cdot\hat{\mathbf{a}} = -B + \mathcal{O}(\epsilon) \tag{2.38}$$

where $\mathrm{d}\hat{\mathbf{a}} \simeq \hat{\mathbf{c}}\mathrm{d}\alpha + \epsilon\boldsymbol{\nabla}\hat{\mathbf{a}} \cdot \mathrm{d}\mathbf{R}$, which allows us to simplify γ_0 further.

$$\begin{aligned}\gamma_0 = &\left(\frac{1}{\epsilon}q\mathbf{A} + mv_\parallel\mathbf{b} + m\mathbf{u}_E + \mathcal{O}(\epsilon)\right)\cdot\mathrm{d}\mathbf{R} + \epsilon\frac{m}{q}\mu\mathrm{d}\alpha - \epsilon\frac{m}{\Omega_{ci}}\frac{1}{B}\hat{\mathbf{c}}\cdot\boldsymbol{\nabla}\Phi\mathrm{d}v_\perp \\ &+ \epsilon\frac{mv_\perp}{\Omega_{ci}}\frac{1}{B}\hat{\mathbf{a}}\cdot\boldsymbol{\nabla}\Phi\mathrm{d}\alpha - \left(\frac{1}{2}m\left[v_\parallel^2 + v_\perp^2 + u_E^2\right] + q\Phi\left(\mathbf{R}\right) + \mathcal{O}(\epsilon)\right)\mathrm{d}t \\ &+ \mathcal{O}(\epsilon^2)\end{aligned} \tag{2.39}$$

A second gauge is then applied of

$$S_2 = \epsilon\frac{mv_\perp}{\Omega_{ci}B}\hat{\mathbf{c}}\cdot\boldsymbol{\nabla}\Phi \tag{2.40}$$

$$\mathrm{d}S_2 = \epsilon\frac{m}{\Omega_{ci}B}\hat{\mathbf{c}}\cdot\boldsymbol{\nabla}\Phi\mathrm{d}v_\perp - \epsilon\frac{mv_\perp}{\Omega_{ci}B}\hat{\mathbf{a}}\cdot\boldsymbol{\nabla}\Phi\mathrm{d}\alpha \tag{2.41}$$

to eliminate $\boldsymbol{\nabla}\Phi$ dependent terms.

Finally, by setting the ordering term ϵ to 1 and neglecting higher ordered terms we find

$$\gamma_0 = \left(q\mathbf{A} + mv_\parallel\mathbf{b} + m\mathbf{u}_E\right)\cdot\mathrm{d}\mathbf{R} + \frac{m}{q}\mu\mathrm{d}\alpha - \left(\frac{1}{2}m\left[v_\parallel^2 + v_\perp^2 + u_E^2\right] + q\Phi\right)\mathrm{d}t \tag{2.42}$$

which gives a gyrophase independent guiding centre one-form Lagrangian. This is rewritten as

$$\gamma_0 = \left(q\mathbf{A} + m\mathbf{u}_E + mv_\parallel\mathbf{b}\right)\cdot\mathrm{d}\mathbf{R} + \frac{\mu B}{\Omega_{ci}}\mathrm{d}\alpha - H_0\mathrm{d}t \tag{2.43}$$

$$H_0 = q\Phi + \mu B + \frac{m}{2}\left(v_\parallel^2 + u_E^2\right). \tag{2.44}$$

The calculations have previously been performed to a higher order by Littlejohn [39, 43], however the $\mathcal{O}(\epsilon^2)$ terms have been neglected in the gyrokinetic equations discussed in this thesis; doing so should not qualitatively affect the physics.

2.4.3 The total gyrokinetic phase-space Lagrangian

With the inclusion of a perturbed potential, the guiding centre Lagrangian γ once again has a gyro-angle dependence and so we wish to transform into a new coordinate system which removes this dependence.

The Lie transform is a natural choice for this transformation since the difference will be small when ϵ tends to zero and because the Lie transform method allows us to freely define the generators, g_n^σ, and the gauge transformation, S. We can therefore specify g_n^σ and S to ensure the gyro-angle dependence is removed from the one-form. This transformation moves the Lagrangian from a guiding centre

frame into a gyro-centre frame.

Formally, the Lie coordinate transform can be written as

$$Z^\sigma = Tz^\sigma \tag{2.45}$$

where, in general, T is a a sequence of individual near-identity Lie transforms, $T = ...T_3T_2T_1$. In operator form, it can be written as

$$T_n = \exp(\epsilon^n L_n) \tag{2.46}$$

where ϵ is a small parameter and the operator L_n acts on scalars as $L_n f = g_n^\sigma \partial f/\partial z^\sigma$. When acting on a vector, L_n behaves as:

$$(L_n\gamma)_\sigma = g_n^\nu \left(\frac{\partial \gamma_\sigma}{\partial z^\nu} - \frac{\partial \gamma_\nu}{\partial z^\sigma}\right). \tag{2.47}$$

The general expression for the transformation of the one-form from guiding-centre to gyro-centre co-ordinates under T is

$$\Gamma = T^{-1}\gamma + \mathrm{d}S \tag{2.48}$$

where S represents an unspecified gauge transformation.

Due to ϵ being small and the nature of T as a near-identity transformation, it is possible to expand T. Expanding T and keeping terms up to $\mathcal{O}(\epsilon^3)$ gives

$$T^{-1} = (T_2T_1)^{-1} = \exp(-\epsilon L_1)\exp(-\epsilon^2 L_2) \tag{2.49}$$

$$T^{-1} = \left(1 - \epsilon L_1 + \epsilon^2 \frac{L_1^2}{2} + \mathcal{O}(\epsilon^3)\right)\left(1 - \epsilon^2 L_2 + \mathcal{O}(\epsilon^3)\right) \tag{2.50}$$

$$T^{-1} = 1 - \epsilon L_1 + \epsilon^2\left(\frac{1}{2}L_1^2 - L_2\right) + \mathcal{O}(\epsilon^3). \tag{2.51}$$

By expanding γ, Γ and S in ϵ, substituting them (along with equation 2.51) into equation 2.48 and then collecting terms of the same order, we find

$$\Gamma_0 = \gamma_0 + \mathrm{d}S_0, \tag{2.52}$$

$$\Gamma_1 = \gamma_1 - L_1\gamma_0 + \mathrm{d}S_1, \tag{2.53}$$

$$\Gamma_2 = \gamma_2 - L_1\gamma_1 + \left(\frac{1}{2}L_1^2 - L_2\right)\gamma_0 + \mathrm{d}S_2. \tag{2.54}$$

To begin with, we set $\mathrm{d}S_0 = 0$ and choose to make $g_1^t = 0$ which will give

$$\begin{aligned}\Gamma_1 = &- q\delta\phi \mathrm{d}t + \mathrm{d}S_1 + g_1^\alpha \frac{m}{q}\mathrm{d}\mu - g_1^\mu \frac{m}{q}\mathrm{d}\alpha + m g_1^{\mathbf{R}} \cdot \mathbf{b}\mathrm{d}v_\parallel \\ &- m g_1^{v_\parallel}\mathbf{b}\cdot\mathrm{d}\mathbf{R} + q\left(g_1^{\mathbf{R}} \times \mathbf{B}^*\right)\cdot\mathrm{d}\mathbf{R} \\ &+ \left[g_1^\mu\left(B + \frac{B}{2\Omega_{ci}}\mathbf{b}\cdot\boldsymbol{\nabla}\times\mathbf{u}_E\right) + g_1^{v_\parallel} m v_\parallel + g_1^\alpha q\frac{\partial\Phi}{\partial\theta} - g_1^{\mathbf{R}}\cdot\boldsymbol{\nabla}H_0\right]\mathrm{d}t,\end{aligned} \tag{2.55}$$

where

$$g_1^{\mathbf{R}} \equiv \left(g_1^{R_1}, g_1^{R_2}, g_1^{R_3}\right).$$

In equation 2.55, we may choose $\mathrm{d}S_1$ and g_1^σ so that all $\Gamma_{1\sigma}$ except for Γ_{1t} vanish. By also requiring that there be no α dependence in Γ_{1t} we get

$$\Gamma_{1t} = -q\langle\delta\phi\rangle\mathrm{d}t \tag{2.56}$$

where $\langle\delta\phi\rangle \equiv (2\pi)^{-1}\oint\delta\phi(\mathbf{R}+\boldsymbol{\rho},t)\mathrm{d}\alpha$ is the perturbed potential averaged over the gyro-angle, also known as the gyro-average.

The second order perturbation analysis is also important to calculate, as it allows us to define a plasma polarisation and a set of equations of motion which are consistent and conservative. Carrying over the previous choices for S_1 and g_1^σ used to find equation 2.56 gives the nonlinear modifications to the effective potential shown in equation 2.58.

Finally, the total gyro-centre phase-space Lagrangian is found to be

$$\Gamma = \left(q\mathbf{A} + m\mathbf{u}_E + m\bar{\mathbf{v}}_\parallel\mathbf{b}\right)\cdot\mathrm{d}\bar{\mathbf{R}} + \frac{\bar{\mu}B}{\Omega}\mathrm{d}\bar{\alpha} - \left(H_0 + q\langle\delta\psi\rangle\right)\mathrm{d}t \tag{2.57}$$

where the effective potential, $\langle\delta\psi\rangle$, is given by

$$\langle\delta\psi\rangle \equiv \langle\delta\phi\rangle - \frac{q}{2\Omega}\left(\frac{\partial}{\partial\mu}\langle\delta\tilde{\phi}^2\rangle + \frac{1}{\Omega_{ci}}\langle\boldsymbol{\nabla}\delta\tilde{\Phi}\times\mathbf{b}\cdot\boldsymbol{\nabla}\delta\tilde{\phi}\rangle\right). \tag{2.58}$$

The overbar is used to indicate gyrocentre variables, $\delta\tilde{\phi} \equiv \delta\phi - \langle\delta\phi\rangle$ and $\delta\tilde{\Phi} \equiv \int\delta\bar{\phi}\mathrm{d}\alpha$. The Hamiltonian, H_0 remains as given in equation 2.44.

2.5 Equations of Motion

The fundamental one-form will always have the same form for Γ in any phase space coordinates. The Euler-Lagrange equation shown in equation 2.20 can still be used with the gyro-centre phase-space Lagrangian from equation 2.57. Substituting the

Lagrangian into the Euler-Lagrange equation, it is possible to calculate the different values of $\hat{\omega}_{ij}$ and then the equations of motion.

$$\frac{\mathrm{d}\bar{\mu}}{\mathrm{d}t} = 0 \tag{2.59}$$

$$\frac{\mathrm{d}\bar{\alpha}}{\mathrm{d}t} = \Omega_{ci} + \frac{1}{2}\mathbf{b}\cdot\boldsymbol{\nabla}\times\mathbf{u}_E + q\frac{\partial\langle\delta\psi\rangle}{\partial\mu} \tag{2.60}$$

$$\mathbf{b}\cdot\frac{\mathrm{d}\bar{\mathbf{R}}}{\mathrm{d}t} = v_\parallel \tag{2.61}$$

$$\begin{aligned}\hat{\omega}_{\mathbf{R}v_\parallel}\frac{\mathrm{d}v_\parallel}{\mathrm{d}t} &= \frac{\partial H}{\partial\mathbf{R}} + \frac{\partial\Gamma_{\mathbf{R}}}{\partial t} \\ = -\mathbf{B}^*\times\frac{\mathrm{d}\bar{\mathbf{R}}}{\mathrm{d}t} - m\mathbf{b}\frac{\mathrm{d}\bar{v}_\parallel}{\mathrm{d}t} &= \bar{\boldsymbol{\nabla}}\left(H_0 + q\langle\delta\psi\rangle\right)\end{aligned} \tag{2.62}$$

where $\mathbf{B}^*$ has been defined as

$$\begin{aligned}\mathbf{B}^* &= \boldsymbol{\nabla}\times\left(\mathbf{A} + \frac{m}{q}\mathbf{u}_E + \frac{m}{q}v_\parallel\mathbf{b}\right) \\ &= \mathbf{B} + \frac{m}{q}\boldsymbol{\nabla}\times\left(\mathbf{u}_E + v_\parallel\mathbf{b}\right).\end{aligned} \tag{2.63}$$

By decomposing equation 2.62, it is possible to find the gyro-center equations of motion. When taking the cross product with $\mathbf{b}$, it is found that

$$\frac{d\bar{\mathbf{R}}}{dt} = \bar{v}_\parallel\frac{\mathbf{B}^*}{B^*_\parallel} + \frac{\mathbf{b}}{qB^*_\parallel}\times\left[q\bar{\boldsymbol{\nabla}}\left(\Phi + \langle\delta\psi\rangle\right) + \frac{m}{2}\bar{\boldsymbol{\nabla}}\left(u_E^2\right)\right] \tag{2.64}$$

and taking the dot product of equation 2.62 with $\mathbf{B}^*$ gives

$$\frac{d\bar{v}_\parallel}{dt} = -\frac{\mathbf{B}^*}{mB^*_\parallel}\cdot\left[q\bar{\boldsymbol{\nabla}}\left(\Phi + \langle\delta\psi\rangle\right) + \bar{\mu}\bar{\boldsymbol{\nabla}}B + \frac{m}{2}\bar{\boldsymbol{\nabla}}\left(u_E^2\right)\right]. \tag{2.65}$$

All $\mathbf{u}_E$ terms in the equations would have been neglected in the weak-flow limit.

It is possible to rewrite $\mathbf{B}^*$ in a different form,

$$\mathbf{B}^* = B^*_\parallel\mathbf{b} + \frac{mv_\parallel}{qB}\left(\mathbf{b}\times\boldsymbol{\nabla}B\right) - \frac{mv_\parallel}{qB}\mathbf{b}\times\left[\mathbf{b}\times\left(\boldsymbol{\nabla}\times\mathbf{B}\right)\right] - \frac{m}{q}\mathbf{b}\times\left[\mathbf{b}\times\left(\boldsymbol{\nabla}\times\mathbf{u}_E\right)\right] \tag{2.66}$$

$$B^*_\parallel = B_\parallel + \frac{mv_\parallel}{q}\mathbf{b}\cdot\left(\boldsymbol{\nabla}\times\mathbf{b}\right) + \frac{m}{q}\mathbf{b}\cdot\left(\boldsymbol{\nabla}\times\mathbf{u}_E\right). \tag{2.67}$$

Additionally, Hahm here introduces the tokamak-relevant ordering which modifies the ordering of the electrostatic fluctuation to $e\delta\phi/T_e \sim \epsilon\delta_B$. This new ordering means the nonlinear modifications to the effective potential are now of

order $\mathcal{O}(\epsilon^2\delta_B^2)$ and can be safely neglected [23]. It is then possible to rearrange and simplify equations 2.64 and 2.65.

$\mathrm{d}\bar{\mathbf{R}}/\mathrm{d}t$ is now given by

$$\begin{aligned}\frac{\mathrm{d}\bar{\mathbf{R}}}{\mathrm{d}t} =& \bar{v}_\parallel \mathbf{b} + \frac{m}{qBB^*_\parallel}\left(\bar{v}_\parallel^2 + \frac{\bar{v}_\perp^2}{2}\right)\mathbf{b}\times\bar{\boldsymbol{\nabla}}B - \frac{m\bar{v}_\parallel^2}{qBB^*_\parallel}\mathbf{b}\times\left[\mathbf{b}\times\left(\bar{\boldsymbol{\nabla}}\times\mathbf{B}\right)\right] \\ &+ \frac{\langle\mathbf{E}+\delta\mathbf{E}\rangle\times\mathbf{B}}{BB^*_\parallel} + \frac{m}{2qB^*_\parallel}\mathbf{b}\times\bar{\boldsymbol{\nabla}}(u_E^2) - \frac{m\bar{v}_\parallel}{qB^*_\parallel}\mathbf{b}\times\left[\mathbf{b}\times\left(\bar{\boldsymbol{\nabla}}\times\mathbf{u}_E\right)\right]\end{aligned} \tag{2.68}$$

and $\mathrm{d}\bar{v}_\parallel/dt$ is given by

$$\begin{aligned}\frac{\mathrm{d}\bar{v}_\parallel}{\mathrm{d}t} =& -\left(\frac{\mathbf{b}}{m} + \frac{\bar{v}_\parallel}{qBB^*_\parallel}\mathbf{b}\times\bar{\boldsymbol{\nabla}}B - \frac{\bar{v}_\parallel}{qBB^*_\parallel}\mathbf{b}\times\left[\mathbf{b}\times\left(\bar{\boldsymbol{\nabla}}\times\mathbf{B}\right)\right]\right. \\ &\left. - \frac{1}{qB^*_\parallel}\mathbf{b}\times\left[\mathbf{b}\times\left(\bar{\boldsymbol{\nabla}}\times\mathbf{u}_E\right)\right]\right)\cdot\left(\bar{\mu}\bar{\boldsymbol{\nabla}}B - q\langle\mathbf{E}+\delta\mathbf{E}\rangle + \frac{m}{2}\bar{\boldsymbol{\nabla}}\left(u_E^2\right)\right)\end{aligned} \tag{2.69}$$

where $\langle\mathbf{E}+\boldsymbol{\delta}\mathbf{E}\rangle = -\boldsymbol{\nabla}\langle\Phi+\delta\phi\rangle$.

The first term in equation 2.68 is clearly the parallel motion of the particle, and the second term a combination of curvature and grad-B drifts. The third term is a diamagnetic drift and the fourth an $\mathbf{E}\times\mathbf{B}$ drift, with contributing background and perturbed electric fields. The last terms are all strong flow related, with the fifth having a form similar to the curvature drift and the sixth sharing a similarity with diamagnetic drift; suggesting the sixth term to be smaller than the fifth.

Equation 2.69 contains a magnetic mirror term, a term giving the parallel electric field acceleration, an interaction between electric field and the parallel components of curvature and diamagnetic drift as well as other terms which include strong-flow related ones.

For the sake of convenience, the overbar which has been used to denote gyrocentre coordinates will now be dropped, but these gyrocentre coordinates will be used throughout the rest of this thesis.

2.6 Toroidal Canonical Momentum

It is already known that μ is a constant of motion, because of equation 2.59. Due to the Hamiltonian approach taken in the derivation of the equations of motion H_0, the particle energy, must also be a constant. However, there is a third constant of motion in an unperturbed system: the toroidal canonical momentum, ψ_c. Since the unperturbed system is axisymmetric it follows that the toroidal component of

the canonical momentum will not vary. ψ_c can be found from the total phase space Lagrangian, equation 2.57, with a similar calculation to that used for the poloidal flux.

$$\psi_c = \frac{1}{q} R\mathbf{p} \cdot \hat{\boldsymbol{\zeta}} \tag{2.70}$$

where $\hat{\boldsymbol{\zeta}} = R\boldsymbol{\nabla}\zeta$ is the toroidal unit vector.

$$\psi_c = \frac{1}{q} R\left(q\mathbf{A} + m\mathbf{u}_E + mv_\parallel \mathbf{b}\right) \cdot \hat{\boldsymbol{\zeta}} \tag{2.71}$$

$$\psi_c = \psi + \frac{m}{q} R\mathbf{u}_E \cdot \hat{\boldsymbol{\zeta}} + \frac{m}{q} Rv_\parallel \mathbf{b} \cdot \hat{\boldsymbol{\zeta}} \tag{2.72}$$

Calculation of the toroidal components of $\mathbf{u}_E$ and $\mathbf{b}$ are then completed

$$\mathbf{b} \cdot \hat{\boldsymbol{\zeta}} = \frac{R}{B}\mathbf{B} \cdot \boldsymbol{\nabla}\zeta = \frac{R}{B}\left(F\boldsymbol{\nabla}\zeta + \boldsymbol{\nabla}\psi \times \boldsymbol{\nabla}\zeta\right) \cdot \boldsymbol{\nabla}\zeta$$

$$= \frac{R}{B}\left(\frac{F}{R^2} + \boldsymbol{\nabla}\zeta \cdot \left(\boldsymbol{\nabla}\psi \times \boldsymbol{\nabla}\zeta\right)\right) = \frac{F}{BR}$$

$$\mathbf{u}_E \cdot \hat{\boldsymbol{\zeta}} = Ru_\zeta \boldsymbol{\nabla}\zeta \cdot \boldsymbol{\nabla}\zeta = \frac{u_\zeta}{R}$$

and substited into equation 2.72 to give the toroidal canonical momentum used in this thesis.

$$\psi_c = \psi + \frac{m}{q}\frac{F}{B} v_\parallel + \frac{m}{q} u_\zeta \tag{2.73}$$

The final term is neglected in the weak-flow limit.

2.7 The δf method

In order to simulate the movement of particles, the distribution function of the markers must be evolved over time. The δf formalism has been developed which reduces the amount of noise generated when evolving the system. This is done by splitting the distribution function into two parts: a background time-independent (or slowly varying) distribution, f_0 and a perturbed distribution function, δf.

$$f(\mathbf{R}, v_\parallel, \mu, t) = f_0(\mathbf{R}, v_\parallel, \mu) + \delta f(\mathbf{R}, v_\parallel, \mu, t) \tag{2.74}$$

By defining f_0 so that it is a function only of the constants of motion, $f_0 = f_0(\psi_c, \mu, \epsilon)$, we have a distribution function that is a solution of the unperturbed Vlasov equation. The distribution function is often chosen to be a Maxwellian distribution because collisions are usually enough to keep the particle distribution close

to a Maxwellian. We define f_0 as

$$f_0(\Upsilon, \epsilon, \mu) = \frac{n_{0i}(\Upsilon)}{(2\pi)^{2/3} v_{thi}^3(\Upsilon)} \exp\left(-\frac{\epsilon}{2T_i(\Upsilon)}\right) \tag{2.75}$$

v_{th} is the thermal velocity, n_0 and T are the equilibrium density and temperature respectively and Υ is an undefined variable which is chosen to parametrise the distance from the magnetic axis.

If Υ is chosen to be ψ_c, then equation 2.75 will be independent of time and referred to as a canonical Maxwellian. However, it is not uncommon to use ψ in the distribution instead (equation 2.75 will then be a local Maxwellian) as it will ensure the reconstructed profiles of the simulation match the input profiles used. In that case though, the assumptions that the distribution is a function independent of time will no longer be true which will lead to additional terms in the derived weight evolution equation. Attempts have been made to derive a corrected canonical momentum, ψ_{corr}, to reduce the difference between the equilibrium and input profiles (such as by Angelino [44]) and this subject will be explored in more depth in later sections.

To evolve this distribution function, we use Vlasov's equation

$$\frac{\mathrm{d}f}{\mathrm{d}t} = \frac{\mathrm{d}f_0}{\mathrm{d}t} + \frac{\mathrm{d}\delta f}{\mathrm{d}t} \tag{2.76}$$

which is equal to 0 in the absence of collisions, and therefore leads to

$$\frac{\mathrm{d}f_0}{\mathrm{d}t} = -\frac{\mathrm{d}\delta f}{\mathrm{d}t}. \tag{2.77}$$

By calculating the time derivative of f_0

$$\frac{\mathrm{d}\delta f}{\mathrm{d}t} = -\underbrace{\frac{\partial f_0}{\partial t}}_{0} - \frac{\partial f_0}{\partial v_\parallel}\frac{\mathrm{d}v_\parallel}{\mathrm{d}t} - \boldsymbol{\nabla} f_0 \cdot \frac{\mathrm{d}\mathbf{R}}{\mathrm{d}t} - \underbrace{\frac{\partial f_0}{\partial \mu}\frac{\mathrm{d}\mu}{\mathrm{d}t}}_{0} \tag{2.78}$$

we find that the evolution of the distribution function is dependent on only two terms. It is possible to expand this further by taking derivatives of f_0

$$\boldsymbol{\nabla} f_0 = \left[\frac{n_0'}{n_0} - \frac{3}{2}\frac{T_i'}{T_i} + \epsilon\frac{T_i'}{T_i^2}\right] f_0 \boldsymbol{\nabla}\Upsilon - \frac{\mu}{T_i} f_0 \boldsymbol{\nabla} B \tag{2.79}$$

$$\frac{\partial f_0}{\partial v_\parallel} = -\frac{m v_\parallel}{T_i} f_0 \tag{2.80}$$

where $T_i' = \partial T_i/\partial\Upsilon$ and $n_0' = \partial n_0/\partial\Upsilon$. Substituting equations 2.79 and 2.80 into

equation 2.78 gives

$$\frac{\mathrm{d}\delta f}{\mathrm{d}t} = \tau(\mathbf{E}) = -f_0 \left[\kappa(\Upsilon) \frac{\mathrm{d}\mathbf{R}}{\mathrm{d}t} \cdot \boldsymbol{\nabla}\Upsilon + \frac{q_i f_0}{T_i} \langle \delta\mathbf{E} \rangle \cdot \left. \frac{\mathrm{d}\mathbf{R}}{\mathrm{d}t} \right|_0 \right] \tag{2.81}$$

where the last term is the derivative taken along an unperturbed orbit, δE is the perturbed electric field and

$$\kappa(\Upsilon) \equiv \left[\frac{n_0'}{n_0} - \frac{3}{2}\frac{T_i'}{T_i} + \epsilon \frac{T_i'}{T_i^2} \right]. \tag{2.82}$$

The equilibrium distribution function used in ORB5 is a modified version of the Maxwellian given here. $\tau(\mathbf{E})$ is also different when implemented within ORB5, but its form appears very similar.

There is another way of obtaining δf that can be used by ORB5. This method is known as the direct δf method and it takes advantage of the fact that the distribution function, f, is constant along trajectories [45].

$$\delta f\left(\mathbf{R}, v_\parallel, \mu, t\right) = f\left(\mathbf{R}, v_\parallel, \mu, t_0\right) - f_0\left(\mathbf{R}(t_0), v_\parallel(t_0), \mu(t_0)\right) \tag{2.83}$$

This method is largely not used in this thesis as it does not allow simulations in linear mode and has heavier restrictions in regards to time step size. However, it was used for checking that the modifications of the ORB5 weight evolution during the addition of strong flows was correct.

Finally, it is important to note that at no point has the assumption that the perturbation δf is small been made. It is desirable for δf to be much smaller than f_0 as it reduces numerical errors, but is not a requirement for either of the described methods.

2.8 Poisson Equation

An important part of gyrokinetic simulations is calculating the perturbed electric field produced by the particles. When assuming only two species of particles in the plasma, electrons of charge $-e$ and mass m_e and a species of ions with charge Ze and mass m_i, the Poisson equation is given by:

$$\nabla^2 \phi\left(\mathbf{x}, t\right) = \frac{e}{\epsilon_0} \left\{ n_e\left(\mathbf{x}, t\right) - Z_i n_i\left(\mathbf{x}, t\right) \right\} \tag{2.84}$$

which must be solved to find the perturbed electric potential in the plasma.

It is assumed that quasi-neutrality is imposed in the system so that the

density of the ions and electrons is equal in an unperturbed state. To solve this equation, the densities in particle space are required. The density in the gyro-centre frame will also include the effects of the gyro-screening of the potential. In particle space, the ion density is given by

$$n\left(\mathbf{x}\right)=\int f\left(z\right)\delta\left(\mathbf{R}+\rho-\mathbf{x}\right)J\mathrm{d}^{6}z. \tag{2.85}$$

where J is the Jacobian and z is the particle phase space.

It is possible to apply the Lie transform used earlier on the distribution function, which will ultimately give the ion density as calculated by Hahm [23].

$$\begin{aligned} n_{i}\left(\mathbf{x},t\right)=&\int B_{\parallel}^{*}f_{i}\left(\mathbf{R},v_{\parallel},\mu,t\right)\delta\left(\mathbf{R}+\boldsymbol{\rho_{i}}-\mathbf{x}\right)\mathrm{d}\mathbf{R}\mathrm{d}v_{\parallel}\mathrm{d}\mu\mathrm{d}\alpha\\ &+\int B_{\parallel}^{*}\frac{q_{i}^{2}}{m_{i}^{2}\Omega_{i}}\left\{\left[\phi-\left\langle\phi\right\rangle\right]\frac{\partial f_{i}\left(\mathbf{R},v_{\parallel},\mu,t\right)}{\partial\mu}\right.\\ &\left.+\frac{1}{m_{i}\Omega_{i}}\left[\boldsymbol{\nabla}\left(\phi-\left\langle\phi\right\rangle\right)\times\mathbf{b}\right]\cdot\boldsymbol{\nabla}f_{i}\right\}\delta\left(\mathbf{R}+\boldsymbol{\rho_{i}}-\mathbf{x}\right)\mathrm{d}\mathbf{R}\mathrm{d}v_{\parallel}\mathrm{d}\mu\mathrm{d}\alpha \end{aligned} \tag{2.86}$$

The second integral of equation 2.86 is a result of the finite Larmor radius effect.

Eventually, Poisson's equation will be linearised which will mean that the ∇f in the last term of equation 2.86 will be replaced with ∇f_{0}. As this term is already of order $\mathcal{O}\left(\epsilon\right)$, the introduction of the temperature and density gradients from ∇f_{0} will make this last term negligible in comparison to the other term and is therefore ignored. This allows the ion density given in equation 2.86 to be written in the form:

$$n_{i}\left(\mathbf{x},t\right)=\left\langle n_{i}\left(\mathbf{x},t\right)\right\rangle+n_{i,pol}\left(\mathbf{x},t\right) \tag{2.87}$$

$$\left\langle n_{i}\right\rangle\left(\mathbf{x},t\right)=\int\mathrm{d}\mathbf{R}\mathrm{d}v_{\parallel}\mathrm{d}\mu\mathrm{d}\alpha B_{\parallel}^{*}f_{i}\left(\mathbf{R},v_{\parallel},\mu,t\right)\delta\left(\mathbf{R}+\boldsymbol{\rho_{Li}}-\mathbf{x}\right) \tag{2.88}$$

$$\begin{aligned} n_{i,pol}\left(\mathbf{x},t\right)=\frac{q_{i}^{2}}{m_{i}^{2}}\int\mathrm{d}\mathbf{R}\mathrm{d}v_{\parallel}\mathrm{d}\mu\mathrm{d}\alpha B_{\parallel}^{*}\frac{1}{\Omega_{ci}}&\left[\phi\left(\mathbf{x},t\right)-\left\langle\phi\right\rangle\left(\mathbf{x},\mu,t\right)\right]\\ &\frac{\partial f_{i}}{\partial\mu}\delta\left(\mathbf{R}+\boldsymbol{\rho_{i}}-\mathbf{x}\right) \end{aligned} \tag{2.89}$$

where $n_{i,pol}\left(\mathbf{x},t\right)$ is known as the polarization density.

A common assumption for the electrons is that they are adiabatic, where the electron mass is neglected and electrons respond instantaneously to any perturbation in the electrostatic potential. The equation of motion for adiabatic electrons is

$$en_{e}\nabla_{\parallel}\phi-T_{e}\nabla_{\parallel}n_{e}=mn_{e}\frac{\mathrm{d}v_{\parallel}}{\mathrm{d}t}$$

$$en_e\nabla_\parallel\phi - T_e\nabla_\parallel n_e = 0 \tag{2.90}$$

which can be rearranged to give

$$\frac{\nabla_\parallel n_e}{n_e} = \frac{e\nabla_\parallel\phi}{T_e}. \tag{2.91}$$

Equations 2.87 and 2.91 then make up the majority of the requirements used to solve for the electrostatic potential within ORB5. Further details on the implementation of Poisson's equation can be found in section 3.12.4.

Chapter 3

ORB5

The code used for the simulations of a tokamak plasma in this thesis is known as ORB5. ORB5 is a global gyrokinetic Particle-In-Cell code written in Fortran 95, created by collaboration between many people and used for simulations investigating plasma behaviour in many different devices. It solves the gyrokinetic equations for a multi-species plasma in a toroidal geometry and can complete both linear and non-linear simulations. One focus of this thesis was on further development of ORB5 and introducing new terms in the gyrokinetic equations of motion and Vlasov equation that are related to strong rotations. There were also several other changes required for successful implementation of strong-flows, largely in the storage of equilibrium quantities and the background potential. Further information on ORB5 can be found in [46].

3.1 Particle-In-Cell Method

There are many possible approaches to use for the modelling of a plasma, such as kinetic, fluid or a hybrid between the two. However, on a wider scale there are two main methods of simulating a plasma. These are the Eulerian and Lagrangian approaches. The Eulerian approach [47, 48] considers fixed points in space and models the plasma which flows through them while the Lagrangian approach considers individual particles, or plasma parcels, and focuses on following them as they move freely about the system (unless they reach a boundary). They both have their merits but the Lagrangian system is easier to implement and it is this approach that the Particle-In-Cell (PIC) method utilises. In a PIC code, individual particles are tracked in a Lagrangian frame, but the fields are derived on fixed grids.

A physical tokamak has an extremely high number of particles and the sim-

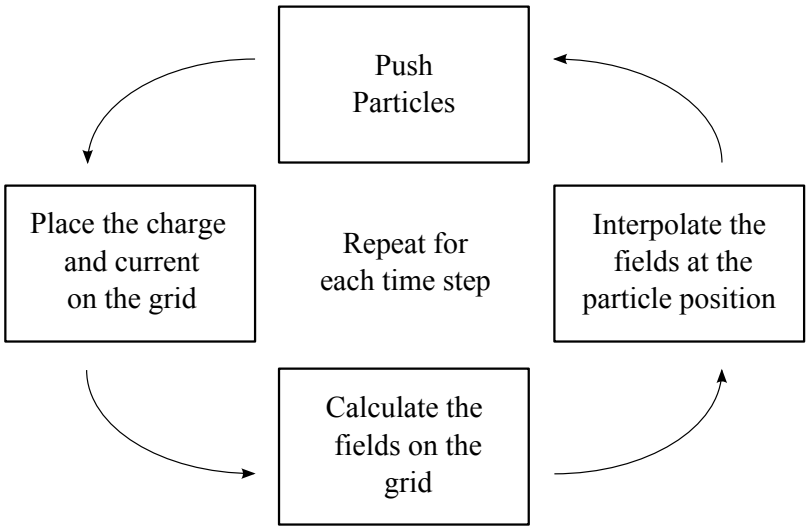

Figure 3.1: The steps performed by a Particle-In-Cell method at each time-step are repeated in a continuous cycle to evolve the system.

ulation of all of them would be impractical; because of this the Particle-In-Cell method uses markers, sometimes also called super particles. Each markers represents a discritized distribution function in a finite volume of phase space, and it is these markers which are evolved in time. The markers have an associated weight which describes the number of physical particles they represent. Each marker also has its own position and velocity, as a real particle would.

After the fields have been calculated from the initial marker positions they, and many equilibrium properties, are stored on 3D grids and interpolated to each markers position. The field and markers are related by a shape function; numerous different functions may be used for this purpose. After this, a discritized set of equations of motion may be used to 'push' the particles and move them forward by a small time step.

$$\mathbf{x_{new}} = \mathbf{x_{old}} + \dot{\mathbf{x}}\Delta t \tag{3.1}$$

$$\mathbf{v_{new}} = \mathbf{v_{old}} + \dot{\mathbf{v}}\Delta t \tag{3.2}$$

Once all particles have been moved, the field equations can be solved again to calculate the new values on the field grid. The specific details of the particle push can vary depending on the implementation, but after the field has been solved this process will begin again and move the markers forward another time step. A simple

representation of the cycle can also be seen in figure 3.1. This discretization can give rise to statistical noise in the simulation, and therefore using a high number of markers with small time steps is desirable. During this movement of the particles, either the volume of the phase space element or the weight of the markers will be evolved in time (while the other is kept constant). In ORB5 it is the weight of the markers which are developed over time.

More in depth information on the PIC method has been written by Birdsall and Langdon [49], Dawson [50] and Tskhakaya [51].

3.2 Local and Global Analysis

When performing a gyrokinetic simulation of a tokamak, a common assumption is that the normalized gyroradius, $\rho_* = \rho_i/a$, is extremely small. The system will then be large compared to the ion gyroradius and the flux surfaces can be assumed to not interact with each other. This is known as the local limit. Many local codes exist and they make the assumption that the equilibrium quantities are constant across the domain of the simulation. As a result, quantities will often be inconsistent with each other; for example, the temperature, T, and temperature gradient, $dT/d\psi$ will both be taken as constants.

When the $\rho_* \to 0$ limit is taken this local approach remains valid, as the simulation will look at a very thin slice of the system. This limit is usually acceptable for devices with large aspect ratios, such as JET. However, some devices, such as MAST, have normalized gyroradii of the order $\rho_* \sim 1/50$ and the local codes may then have a radial domain larger than the system they are simulating.

For such cases, a simulation code which models the full radial domain would be better suited for use. These global codes, such as ORB5, describe the full 3D geometry of a tokamak and allow variation of the equilibrium profiles. The inclusion of varying profiles that remain consistent with each other provides a more accurate treatment of the simulation of a plasma confined in a tokamak device, both with larger and smaller aspect ratios. By changing the value of ρ_* in a global code however, it is possible to compare a local and global code with each other for benchmarking purposes by moving simulations performed within the global code towards the local limit [52].

3.3 Geometry of the tokamak

Cartesian coordinates, and even cylindrical coordinates, are not the best coordinate system to use in ORB5 simulations. Instead, a coordinate system is used that takes advantage of the fact that turbulence in a tokamak tends to align with the magnetic field lines. This coordinate system allows for a simplification of calculations.

One of these coordinates is in the radial direction and is labelled by the poloidal flux, corresponding to the nested flux surfaces, while the other two are based on the poloidal and toroidal angles respectively. The system of co-ordinates used to describe a tokamak in ORB5 and this thesis were shown earlier in figure 1.1; although it is important to note that ORB5 does not limit the cross-section of the tokamak to be circular (it may also be elongated).

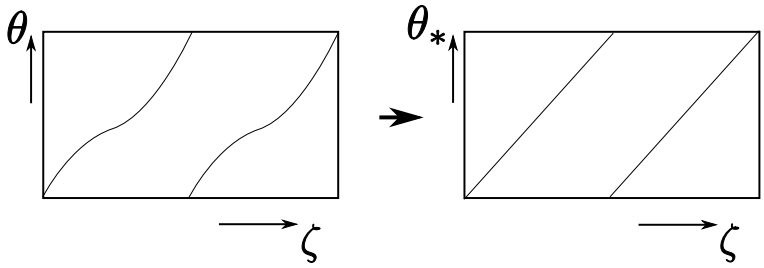

Figure 3.2: The field lines on a flattened flux surfaces when viewed in (θ, ζ) coordinates have a curve, but they map a straight line when viewed in (θ_*, ζ) coordinates.

The set of angles used is chosen such that the equation of a field line gives a straight line on an "un-rolled" flux surface. This is done by distorting one, or both, angles; although doing so requires knowing B in its entirety. The straight field line coordinates used in ORB5 only modify the poloidal angle and leave the toroidal angle unchanged, which allows the axi-symmetry of the system to still be represented simply. Figure 3.2 illustrates the shapes of the field lines on un-rolled flux surfaces for both poloidal angles. The equation relating the new poloidal angle, θ_*, with the un-straightened coordinate system is

$$\theta_* = \frac{1}{q(\rho)} \int_0^\theta \frac{\vec{B} \cdot \vec{\nabla}\zeta}{\vec{B} \cdot \vec{\nabla}\theta'} \mathrm{d}\theta' \tag{3.3}$$

where θ' is a dummy variable used for the integration and $q(\rho)$ is the safety factor.

Although this is the method used in ORB5 there are other coordinate systems that give straight field lines as well. The Hamada coordinate system deforms the

coordinates to give straight current-density lines as well as magnetic field lines, and the Boozer coordinate system modifies the magnetic scalar potential.

The coordinates, $(\boldsymbol{\nabla}\psi, \boldsymbol{\nabla}\theta_*, \boldsymbol{\nabla}\zeta)$, used are in fact curvi-linear co-ordinates which allow the co-ordinate system to have curved grid lines [14]. Although it is true that $\boldsymbol{\nabla}\zeta$ is perpindicular to both $\boldsymbol{\nabla}\psi$ and $\boldsymbol{\nabla}\theta_*$, it is important to note that $\boldsymbol{\nabla}\psi \cdot \boldsymbol{\nabla}\theta_* \neq 0$.

3.4 Magnetic Field

If the magnetic field is axisymmetric, as is assumed in ORB5, then the most general equation for the magnetic field is given by:

$$\mathbf{B} = F(\psi)\boldsymbol{\nabla}\zeta + \boldsymbol{\nabla}\psi \times \boldsymbol{\nabla}\zeta \tag{3.4}$$

where $F(\psi)$ is the poloidal current function. By definition, the magnetic field and the safety factor are very closely linked values. The magnetic shear of a q-profile can be an important quantity in the transport physics and is defined as

$$\hat{s} = \frac{r}{q}\frac{\mathrm{d}q}{\mathrm{d}r} = \frac{\mathrm{d}\ln(q)}{\mathrm{d}\ln(r)}. \tag{3.5}$$

The magnetic equilibrium used in simulations is related to the Grad-Shafranov equation:

$$\nabla^2\psi - \frac{2}{r}\frac{\partial\psi}{\partial r} = -F'(\psi)F(\psi) - r^2p'(\psi) = -rj_\zeta \tag{3.6}$$

By solving this equation with the use of CHEASE [53] or FLOW [54], a true equilibria may be found for given $F(\psi)$ and $p(\psi)$ profiles and used within a simulation. This has been implemented in ORB5, as has the 'ad-hoc' equilibria which is a much simpler implementation that approximates the magnetic flux surfaces as circular concentric. This 'ad-hoc' equilibria is not a true solution of the Grad-Shafranov equation, and instead the magnetic field takes the form discussed in section 3.7.1.

3.5 Parallelisation scheme

A high number of particles are required in order to give good convergence, and therefore a large amount of memory and CPU power is also required. Fortunately, PIC schemes are inherently easy to parallelise, due to the markers each moving independently. ORB5 has been highly parallelised and can be used on upwards of 8000 cores. Parallelisation of ORB5 uses the Message Passing Interface (MPI) to

exchange data between processors [55].

This parallelisation is accomplished by using a 2D domain cloning algorithm, where the 3D torus is cloned and split across many processors [56]. The use of P processors can be decomposed to

$$P = CP_\zeta, \tag{3.7}$$

where C is the number of clones and P_ζ is the number of processors the toroidal direction has been split across. Each of the P_ζ processors contains a slice of the total torus. Each clones is equivalent in that they all contain a copy of the entire torus and the 3D grids used to store the fields.

The particles are evenly distributed across all processors; each containing approximately N/P markers (with N being the total number of markers used in the simulation). After each step of the integration scheme the markers will have moved in the toroidal direction, and some will have left their toroidal slice. At this point, the markers that have moved beyond the bounds of their processors will be sent to a new corresponding processor that represents the toroidal slice they are now in. This decomposition in toroidal space takes advantage of the axisymmetric nature of the system.

It is important for a balance to be achieved between C and P_ζ. If only one clone is used, then each toroidal slice may be unreasonably small and cause each particle to be moved from its processor after every time step. This will cause the communication between processors to substantially slow down the simulation. However, too many clones will drastically increase the memory required and also lead to excessive amounts of communication between processors. This is due to the communication between the clones, as the particles must be summed on the grids across all clones after each time step.

3.6 Normalization

In ORB5, every dimensioned value has been renormalized into code units, which are usually not in standard units of measurement. All calculations are performed in these code units. These normalizations arise from the choice of units for length and magnetic field strength and are shown in table 3.1.

In this table, $T_e(s_{peak})$ is the electron temperature at an assigned flux surface, s_{peak}. All lengths in ORB5 are in units of gyro-radii, ρ_i, and time is in units of inverse gyro-frequency, Ω_{ci}, of the same nominal particle that is used to define the thermal velocity. The electric charge is normalized against an elementary electric charge and

	Units
Temperature	$T_e(s_{peak})$
Length	ρ_i
Time	Ω_{ci}^{-1}
Velocity	$c_s = \rho_i \Omega_i$
Magnetic field	B_0
Charge	e
Mass	m_i

Table 3.1: This table shows the units used for quantities stored in ORB5. s_{peak} is the s value at which the gradient profiles peak.

mass is normalized to the mass of an ion species m_i. B_0 is the magnetic field at the axis.

3.7 Equilibria

In the past, there were two different options for implementing the equilibria in ORB5, the 'ad-hoc' equilibria or a numerical MHD equilibria calculated by the CHEASE code [53]. Recently though, a new option has been added for use as an equilibria. This new equilibria utilises the FLOW code [54] to calculate an MHD equilibria which would be consistent with a strongly rotating plasma. The FLOW equilibria has not been used in this thesis as it was still undergoing implementation and testing at the time of writing, however, it should serve to provide useful equilibria in future ORB5 simulations which investigate toroidal rotation.

The background distribution function, f_0, used is a Maxwellian similar to equation 2.75, and is in fact identical to this in the absence of a background potential field. The background distribution function used in ORB5 is given by equation 3.32 from section 3.11.

3.7.1 Ad-hoc equilibria

For all of the cases discussed in this thesis, an ad-hoc equilibria is used instead of a real magnetic equilibrium. This ad-hoc equilibria is a simple set of circular concentric flux surfaces. Additionally, $F(\psi)$ is taken to be a constant with this equilibria. The magnetic field in this case is given by:

$$\mathbf{B} = \frac{B_0 R_0}{R}\hat{\mathbf{e}}_\zeta - \frac{B_0 \rho}{\bar{q}(\rho) R}\hat{\mathbf{e}}_\theta \tag{3.8}$$

where B_0 and R_0 are the magnetic field and major radius at the axis respectively. $\rho = r/a$ gives the normalized radial coordinate for the tokamak and $\bar{q}$ is a quantity known as the psuedo safety factor, related to the safety factor by

$$q(\psi) = \frac{\bar{q}(\rho)}{\sqrt{1 - \frac{r^2}{R_0^2}}}. \tag{3.9}$$

3.7.2 Storage of Equilibria quantities

A 1D grid, varying radially, is used to store the input profiles such as temperature, density and the flux surface average of background potential. A 2D grid, which varies with (s, θ_*), stores the equilibria quantities. This information is linearly interpolated from the grids to the marker positions.

Included on the 2D equilibria grid is the background electrostatic potential, while the perturbed potential is stored on the field grid. The flux surface averaged background potential is calculated from this 2D background electrostatic potential. Currently, only a radially varying potential has been implemented in ORB5 but the potential has been intentionally stored in this way so as to allow for an expansion into a poloidally varying potential in the future. This change was made because a strongly rotating equilibria may be expected to have a small poloidal variation of background flow.

3.8 Rotation Profiles

The background rotation profiles used in simulations are specified at input in terms of a background electric potential, Φ. The background electric potential results in a toroidal rotation from a combination of the $E \times B$ drift and the parallel velocity implied by the choice of equilibrium.

There are some restrictions to the background potential that may be used. As s tends towards 0, the electric field E_s must also tend towards 0. This is because a finite value of radial electric field at s=0 would imply that the background potential was not a smooth function. Additionally, for a purely toroidal rotation, this would imply an infinite rotation at the axis.

The background $E \times B$ velocity is defined as

$$u_E = \frac{\mathbf{E} \times \mathbf{b}}{B} = \left(\frac{\partial \Phi}{\partial \psi}\right) \frac{1}{B} \boldsymbol{\nabla} \psi \times \mathbf{b} \tag{3.10}$$

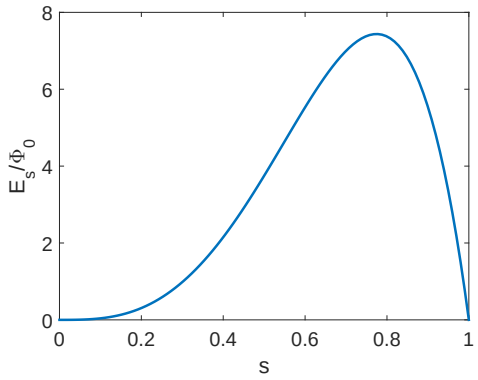

Figure 3.3: The electric field for potential profile 1.

3.8.1 Profile 1

The first profile is designed to have a large peak in E_s at approximately $s = 0.77$. Its only purpose has been for testing the modifications to the canonical equilibrium distribution function, providing a large flow to exaggerate any modifications to the equilibrium profiles, and testing the conservation of ψ_c and ϵ. The shape of the electric field is as shown in figure 3.3, and is given by:

$$\Phi(s) = 40\Phi_0 \left(\frac{s^6}{6} - \frac{s^4}{4} \right) \tag{3.11}$$

$$E_s = -\frac{\partial \Phi}{\partial s} = -40\Phi_0 \left(s^5 + s^3 \right) \tag{3.12}$$

$$E_\psi = E_s \frac{\mathrm{d}s}{\mathrm{d}\psi} = -\frac{40\Phi_0 \left(s^5 + s^3 \right)}{2s\psi_0} = -\frac{20\Phi_0}{\psi_0} \left(s^4 + s^2 \right). \tag{3.13}$$

3.8.2 Profile 2

The main background electric potential profile used is that of a constant rotation rate, $\mathrm{d}\Phi/\mathrm{d}\psi$. The electric field, E_s, can be seen in figure 3.4 and is given by:

$$\Phi(s) = \Phi_0 s^2 \tag{3.14}$$

$$E_s = -\frac{\partial \Phi}{\partial s} = -2\Phi_0 s \tag{3.15}$$

$$E_\psi = E_s \frac{\mathrm{d}s}{\mathrm{d}\psi} = -\frac{2\Phi_0 s}{2s\psi_0} = -\frac{\Phi_0}{\psi_0}. \tag{3.16}$$

All simulations discussed in this thesis which have a solid body rotation have used this rotation profile.

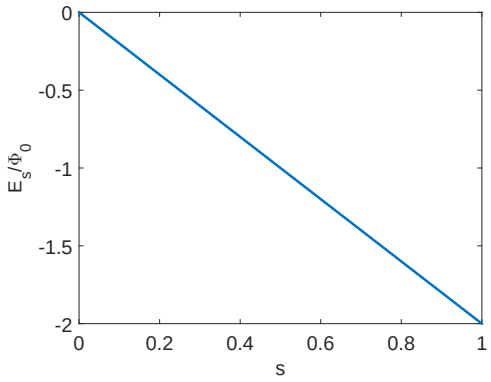

Figure 3.4: The electric field for potential profile 2.

3.9 Temperature and Density Profiles

Multiple input profiles are implemented in ORB5 and used in this thesis. The input profiles are usually specified in terms of a functional form and several parameters of this form. The functional form is chosen to be consistent across each species but their corresponding parameters may change. This allows the amplitude and gradients, for example, to vary between species.

The width of the profile, Δ_s, is only dependent upon the species and not upon the profile it is used in. a is the minor radius of the tokamak and therefore independent of the individual profiles. Finally, ρ_{peak} is the radius at which the temperature and density are normalized and that the gradients of the equilibrium properties are centred and peak. This normalization can be seen in figures 3.5 and 3.6 as the point for which $T_i/T_{i0} = 1$.

$L_{A,s}$ gives the gradient scale length chosen for an equilibrium quantity A and species s.

3.9.1 Profile 1

The first profile is a peaked pressure profile, defined so that $\frac{1}{A_s(\rho)}\frac{\mathrm{d}A_s}{\mathrm{d}\rho}$ has a peak at ρ_{peak} equal to $a/L_{A,s}$.

$$\frac{1}{A_s(\rho)}\frac{\mathrm{d}A_s}{\mathrm{d}\rho} = -\frac{a}{L_{A,s}}\cosh^{-2}\left(\frac{\rho-\rho_{peak}}{\Delta_s}\right) \tag{3.17}$$

$$\frac{A_s(\rho)}{A_s(\rho_{peak,s})} = \exp\left\{-\frac{a\Delta_s}{L_{A,s}}\tanh\left(\frac{\rho-\rho_{peak}}{\Delta_s}\right)\right\} \tag{3.18}$$

A is substituted for the temperature or density depending on the profile being

calculated. The shape of this profile can be seen in figure 3.5.

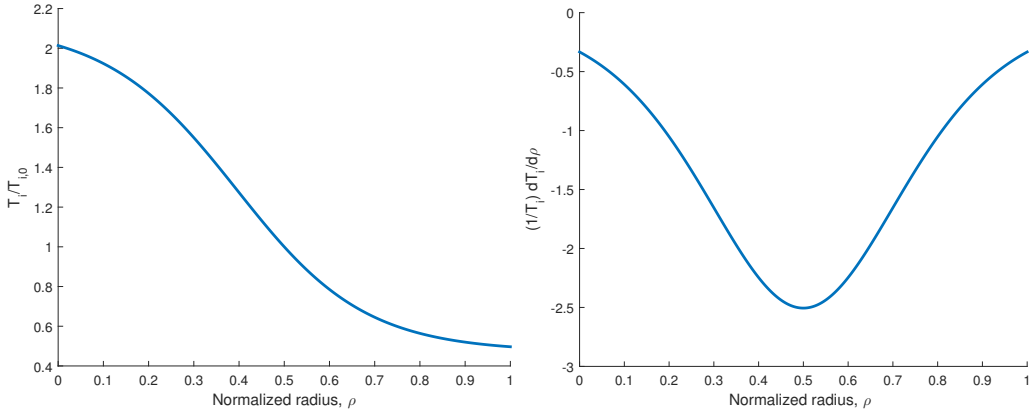

Figure 3.5: Temperature in a peaked pressure profile, with $\Delta_s = 0.3$, $\rho_{peak} = 0.5$ and $L_{T,s} = \frac{1}{2.5}$ in normalized units of a.

3.9.2 Profile 2

The second profile is referred to as a gradient plateau profile due to the large width which has constant value in $\frac{1}{A_s(\rho)}\frac{\mathrm{d}A_s}{\mathrm{d}\rho}$. This plateau is centred around ρ_{peak} with a width of $2\Delta_s$.

$$\frac{1}{A_s(\rho)}\frac{\mathrm{d}A_s}{\mathrm{d}\rho} = -\frac{a}{2L_{A,s}}\left[\tanh\left(\frac{\rho-\rho_{peak}+\Delta\rho}{\Delta_s}\right) - \tanh\left(\frac{\rho-\rho_{peak}-\Delta\rho}{\Delta_s}\right)\right] \tag{3.19}$$

$$\frac{A_s(\rho)}{A_s(\rho_{peak})} = \exp\left\{-\frac{a\Delta_s}{2L_{A,s}}\ln\left[\frac{\cosh\left(\frac{\rho-\rho_{peak}+\Delta\rho}{\Delta_s}\right)}{\cosh\left(\frac{\rho-\rho_{peak}-\Delta\rho}{\Delta_s}\right)}\right]\right\} \tag{3.20}$$

An example of this profile can be seen in figure 3.6.

3.10 Diagnostics

It is possible to evaluate various plasma quantities by taking moments of the distribution function. The general form for a moment $\mathbf{M}$ is given by:

$$\mathbf{M}(\mathbf{x},t) = \int f(\mathbf{x},\mathbf{v},t)\,\mathbf{g}(\mathbf{v})\,\mathrm{d}\mathbf{v} \tag{3.21}$$

where $g(\mathbf{v})$ is a function that varies depending on the moment of interest. Furthermore, similarly to the δf approach this moment can be split into equilibrium and

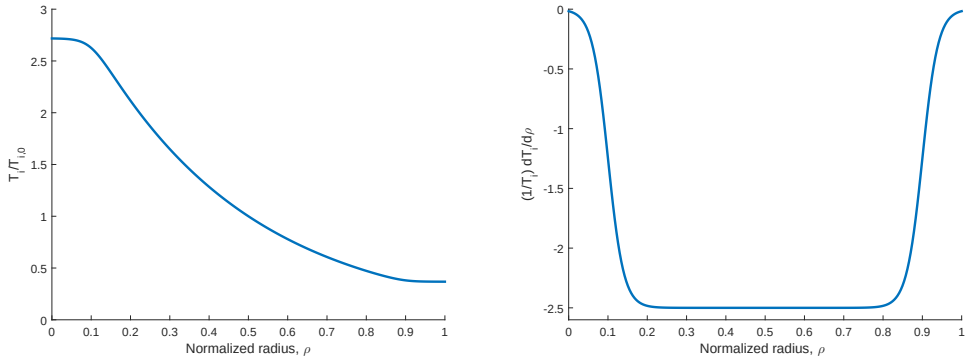

Figure 3.6: The temperature in a plateau profile with $\Delta_s = 0.04$, $\rho_{peak} = 0.5$ and $L_{T,s} = \frac{1}{2.5}$ in units of a.

perturbed moments.

$$\mathbf{M}(\mathbf{x}, t) = \mathbf{M}_0(\mathbf{x}) + \delta\mathbf{M}(\mathbf{x}, t) \tag{3.22}$$

$$\mathbf{M}_0(\mathbf{x}) = \int f_0(\mathbf{x}, \mathbf{v})\, \mathbf{g}(\mathbf{v})\, \mathrm{d}\mathbf{v} \tag{3.23}$$

$$\delta\mathbf{M}(\mathbf{x}, t) = \int \delta f(\mathbf{x}, \mathbf{v}, t)\, \mathbf{g}(\mathbf{v})\, \mathrm{d}\mathbf{v} \tag{3.24}$$

Usually, the flux surface average of a quantity will be desired. This is calculated by taking the volume average between ψ and $\psi + \mathrm{d}\psi$. In practice, this is performed with a binning in radius.

The flux surface averages are given by

$$\langle \mathbf{M}_0(\mathbf{x}) \rangle_\psi = \frac{1}{V_i} \sum \frac{V}{N} f_0\left(\mathbf{R}, v_\parallel, \mu\right) \mathbf{g}\left(v_\parallel, \mu\right) \tag{3.25}$$

$$\langle \delta\mathbf{M}_0(\mathbf{x}) \rangle_\psi = \frac{1}{V_i} \sum \frac{V}{N} w \mathbf{g}\left(v_\parallel, \mu\right) \tag{3.26}$$

where f_0 is the background equilibrium distribution function, w is the weight of the markers, V is the total volume between ψ and $\psi + \mathrm{d}\psi$, V_i is the bin volume and N is the total number of markers.

The radial heat flux Q, parallel momentum flux $\Gamma_\parallel$, and the radial particle flux P, all of which the $E \times B$ velocity dominates in simulations, are given by

$$\langle Q \rangle = \frac{1}{V} \int_V \mathrm{d}\mathbf{R} \int f\left(\mathbf{R}, v_\parallel, \mu, t\right) \frac{1}{2} m_i v^2 \frac{\langle \mathbf{E} \rangle \times \mathbf{B}}{B B_\parallel^*} \cdot \frac{\boldsymbol{\nabla}\psi}{|\nabla\psi|} B_\parallel^* \mathrm{d}v_\parallel \mathrm{d}\mu \mathrm{d}\alpha \tag{3.27}$$

$$\langle \Gamma_\parallel \rangle = \frac{1}{V} \int_V \mathrm{d}\mathbf{R} \int f\left(\mathbf{R}, v_\parallel, \mu, t\right) m_i v_\parallel \frac{\langle \mathbf{E} \rangle \times \mathbf{B}}{B B_\parallel^*} \cdot \frac{\boldsymbol{\nabla}\psi}{|\nabla\psi|} B_\parallel^* \mathrm{d}v_\parallel \mathrm{d}\mu \mathrm{d}\alpha \tag{3.28}$$

$$\langle P \rangle = \frac{1}{V} \int_V \mathrm{d}\mathbf{R} \int f\left(\mathbf{R}, v_\parallel, \mu, t\right) \frac{\langle \mathbf{E} \rangle \times \mathbf{B}}{B B_\parallel^*} \cdot \frac{\boldsymbol{\nabla}\psi}{|\nabla\psi|} B_\parallel^* \mathrm{d}v_\parallel \mathrm{d}\mu \mathrm{d}\alpha. \tag{3.29}$$

The dominant flux in simulations is the perturbed flux moment and not the background moment. In post-processing, the reconstructed temperature profile can be calculated from the flux surface averages of the velocities

$$\langle T \rangle = \frac{1}{3} \langle \left(\mathbf{v} - \langle v_\parallel \rangle \mathbf{b}\right)^2 \rangle = \frac{1}{3} \left(\langle {v_\parallel}^2 \rangle + \langle {v_\perp}^2 \rangle - \langle v_\parallel \rangle^2 \right). \tag{3.30}$$

where $\langle v_\parallel \rangle$, $\langle v_\parallel^2 \rangle$ and $\langle v_\perp^2 \rangle$ have been normalized with $\langle n \rangle$.

3.11 Equilibrium distribution function

In an unperturbed system, the distribution function will be given by $f = f_0$ and so the Vlasov equation, equation 2.3, will be

$$\frac{\mathrm{d}f_0}{\mathrm{d}t} = \frac{\partial f_0}{\partial t} + \frac{\partial f_0}{\partial v_\parallel} \frac{\mathrm{d}v_\parallel}{\mathrm{d}t} + \boldsymbol{\nabla} f_0 \cdot \frac{\mathrm{d}\mathbf{R}}{\mathrm{d}t} + \frac{\partial f_0}{\partial \mu} \frac{\mathrm{d}\mu}{\mathrm{d}t} = 0. \tag{3.31}$$

It is therefore a requirement that f_0 be defined so as to be constant with time. This is achieved in ORB5 by defining the background equilibrium distribution function as a function only of constants of motion, $f_0 = f_0(\psi_c, \epsilon, \mu)$.

In ORB5, the background distribution function, f_0, has been chosen to have the functional form of a Maxwellian, and before the introduction of density corrections due to strong flow terms was given by

$$f_0\left(\psi_c, \epsilon, \mu\right) = \left(\frac{m}{2\pi T\left(\psi_c\right)} \right)^{3/2} n_0\left(\psi_c\right) \exp\left\{ -\frac{1}{T\left(\psi_c\right)} \left(\epsilon - q\Phi\left(\psi_c\right)\right) \right\} \tag{3.32}$$

where

$$\epsilon = \frac{m}{2} \left(v_\parallel^2 + u_E^2 \right) + \mu B + q\Phi\left(\psi\right). \tag{3.33}$$

The term with background potential as a function of canonical momentum, $\Phi\left(\psi_c\right)$, had been added earlier as an attempt to ensure that a background potential did not make the effective equilibrium profiles deviate too far from the input profiles.

The effective equilibrium profiles, or reconstructed profiles, are found by taking the flux surface average moments with f_0. The background distribution is a function of ψ_c, and the temperature and density are therefore also functions of ψ_c in the distribution. As the parameter we use as an effective radial coordinate (ψ_c) has a small velocity dependence, a variation is expected from the initial input profiles which are functions of ψ only. The distribution is not exactly in thermal

equilibrium.

A poorly defined gyrokinetic equilibrium has previously been found to lead to the introduction of unphysical behaviour and it is therefore desirable to choose a background distribution function that will match the input profiles as closely as possible [44]. In addition, having the reconstructed equilibria of the distribution function close to the input profiles will allow the system to be more easily defined by the user.

One possibility is to consider a distribution function that is a function of poloidal flux, unfortunately though this would lead to a distribution function that changes with time, even in an unperturbed system. A second alternative that has been used in the past in ORB5 is to add a correction term to ψ_c; this additional term will be a constant and will therefore not break conservation [44]. However, neither of these methods have been used in the work covered by this thesis and instead a new density correction term has been used. It is due to the strong flows that we require the introduction of this particular density correction. However, it could be considered that the canonical potential in the exponential of equation 3.32 already serves to apply a density correction to the distribution function. We are therefore applying a modification to the already existing density correction.

3.11.1 Local Limit Expansion

To get a clearer picture of how the new strong-flow terms affect the reconstructed profiles we can expand $\Phi(\psi_c)$ in the local limit. This is done by taking a Taylor expansion of $\Phi(\psi_c)$ around ψ.

$$\Phi(\psi_c) \simeq \Phi(\psi) + \frac{mFv_\parallel}{qB}\frac{\partial\Phi}{\partial\psi} + \frac{m}{q}u_\zeta\frac{\partial\Phi}{\partial\psi} + \mathcal{O}\left(\epsilon^2\right) \tag{3.34}$$

where $\mathcal{O}(\epsilon^2)$ terms and higher will be neglected in further calculations. For convenience, we will define

$$H_\phi \equiv \epsilon - q\Phi(\psi_c) = \frac{m}{2}\left(v_\parallel^2 + u_E^2\right) + \mu B + q\Phi(\psi) - q\Phi(\psi_c)$$

so that the distribution is given by

$$f_0(\psi_c, \epsilon, \mu) = \left(\frac{m}{2\pi T(\psi_c)}\right)^{3/2} n_0(\psi_c) \exp\left\{-\frac{H_\phi}{T(\psi_c)}\right\}.$$

In the local limit, H_ϕ is given by

$$H_\phi \simeq \frac{m}{2}\left(v_\parallel^2 + u_E^2\right) + \mu B - \frac{m v_\parallel F}{B}\frac{\partial \Phi}{\partial \psi} - m u_\zeta \frac{\partial \Phi}{\partial \psi}. \tag{3.35}$$

We then write H_ϕ in the form

$$\begin{aligned} H_\phi &= \frac{m}{2}\left[v_\perp^2 + \left(v_\parallel - v_0\right)^2\right] + \mathcal{K} \\ &= \frac{m}{2}v_\perp^2 + \frac{m}{2}v_\parallel^2 - m v_\parallel v_0 + \mathcal{K} \end{aligned} \tag{3.36}$$

and by equating the $v_\parallel$ terms in equations 3.35 and 3.36, v_0 is found to be

$$v_0 = \frac{F}{B}\frac{\partial \Phi}{\partial \psi}. \tag{3.37}$$

Due to the form of equation 3.36, it is clear that this expression for v_0 gives an expected parallel flow in the local limit.

Equating the two equations again, we solve for $\mathcal{K}$

$$\begin{aligned} \mathcal{K} &= \frac{m}{2}u_E^2 - m u_\zeta \frac{\partial \Phi}{\partial \psi} - \frac{m}{2}\frac{F^2}{B^2}\left(\frac{\partial \Phi}{\partial \psi}\right)^2 \\ &= \frac{m}{2}u_E^2 - m\frac{|\nabla \psi|^2}{B^2}\left(\frac{\partial \Phi}{\partial \psi}\right)^2 - \frac{m}{2}\left(R^2 - \frac{|\nabla \psi|^2}{B^2}\right)\left(\frac{\partial \Phi}{\partial \psi}\right)^2 \\ &= \underbrace{\frac{m}{2}\left(u_E^2 - \frac{|\nabla \psi|^2}{B^2}\left(\frac{\partial \phi}{\partial \psi}\right)^2\right)}_{=0} - \frac{m}{2}R^2\left(\frac{\partial \Phi}{\partial \psi}\right)^2 \end{aligned} \tag{3.38}$$

where we have used $F^2 = B^2R^2 - |\nabla \psi|^2$, which follows from equation 3.4.

It is now possible to re-write the background distribution function, equation 3.32, as the distribution function in the local limit

$$\begin{aligned} f_0\left(\psi_c, \epsilon, \mu\right) \simeq \left(\frac{m}{2\pi T\left(\psi_c\right)}\right)^{3/2} n_0\left(\psi_c\right) \exp\Bigg\{ &- \frac{m}{2T\left(\psi_c\right)} \\ &\left(v_\perp^2 + \left(v_\parallel - \frac{F}{B}\frac{\partial \Phi}{\partial \psi}\right)^2 - R^2\left(\frac{\partial \Phi}{\partial \psi}\right)^2\right)\Bigg\}. \end{aligned} \tag{3.39}$$

Previously, a set of gyrokinetic equations and a background distribution function have been derived in the co-moving frame of the plasma for a strong rotation

case by Peeters [34]. The distribution function in the co-moving frame is

$$F_M = \frac{n_{R_0}}{(2\pi T/m)^{3/2}} \exp\left\{ -\frac{m\left(v_\parallel - u_\parallel\right)^2}{2T} - \frac{\mu B}{T} - \frac{Ze\langle\Phi\rangle}{T} + \frac{m}{2T}\Omega^2\left(R^2 - R_0^2\right) \right\} \tag{3.40}$$

where

$$u_\parallel = \frac{F}{B}\left(\omega_\phi\left(\psi\right) - \Omega\right), \tag{3.41}$$

Ω is the angular frequency of the co-moving frame and $\omega_\phi(\psi)$ is a radial function describing the angular frequency of the plasma in the laboratory frame. The parallel flow, $u_\parallel$ is the parallel flow in the co-moving frame, not the laboratory frame. Finally, n_{R_0} is the density at R_0 and is related to the flux surface for which $\Omega = \omega_\phi$ by

$$n_0 = n_{R_0} \exp\left\{ -\frac{Ze\langle\Phi\rangle}{T} + \frac{m\Omega^2\left(R^2 - R_0^2\right)}{2T} \right\}. \tag{3.42}$$

Comparing equation 3.40 with the background distribution function equation 3.39, we see that the two distributions have equivalent forms if equation 3.40 is considered in the lab frame. This would then imply that the rotation rate, ω_ϕ, is given by the partial derivative of the background potential. The toroidal rotation rate Ω_t is then defined as

$$\Omega_t \equiv \omega_\phi = \frac{\partial\Phi}{\partial\psi}. \tag{3.43}$$

Ω_t is explicitly derived in appendix B and is found to match this definition. Equation 3.42 suggests that the $R^2\left(\partial\Phi/\partial\psi\right)^2$ term in f_0 will cause a density variation.

3.11.2 Density Correction Term

Due to the variation of the equilibrium profiles caused by applying a background potential, a density correction term is introduced to the background equilibrium distribution function of ORB5. This correction is seen as the new R_0^2 exponent found in equation 3.44.

$$f_0\left(\psi_c, \epsilon, \mu\right) = \left(\frac{m}{2\pi T\left(\psi_c\right)}\right)^{3/2} n_0\left(\psi_c\right) \exp\left\{ -\frac{m}{2T\left(\psi_c\right)} R_0^2 \left(\frac{\partial\Phi(\psi_c)}{\partial\psi_c}\right)^2 \right\} \exp\left\{ -\frac{1}{T\left(\psi_c\right)}\left(\epsilon - q\Phi\left(\psi_c\right)\right) \right\} \tag{3.44}$$

The reason for this choice of density correction becomes more transparent when expanding equation 3.44 in the local limit, as before.

$$f_0 \simeq \left(\frac{m}{2\pi T(\psi)}\right)^{3/2} n_0(\psi) \exp\left\{-\frac{m}{2T(\psi)}\left[v_\perp^2 + \left(v_\parallel - \frac{F}{B}\frac{\partial\Phi(\psi_c)}{\partial\psi_c}\right)^2 - \left(R^2 - R_0^2\right)\left(\frac{\partial\Phi}{\partial\psi}\right)^2\right]\right\} \tag{3.45}$$

It can be seen from equation 3.45 that the new density correction term will subtract from the earlier found density modification in a rotating plasma. It is important to note that the correction term is actually implemented as a function of ψ_c and not ψ; this is to ensure the background distribution remains a function of the constants of motion only. It is expected that the inclusion of this term will help to reduce the variation of the reconstructed density and temperature from the input profiles, while still retaining any poloidal variation. The introduction of this density correction term is possible because of the freedom to choose any function as f_0.

Implementation of this term in ORB5 is done by storing $\frac{m}{2T}\left(\partial\Phi/\partial\psi\right)$ on the same 1D grid as the flux surface averaged background potential. In a similar fashion to background potential it is interpolated for the marker position each time the distribution function is calculated. It is required that this density correction term be finite at the axis.

3.11.3 Reconstructed equilibrium profiles

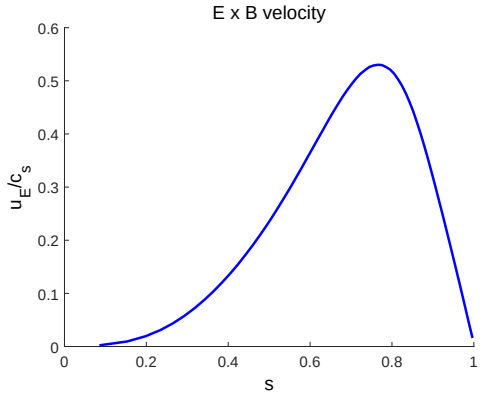

Figure 3.7: $E \times B$ velocity profile as a function of s. For these tests, u_E is chosen to be of order of the thermal velocity.

We now plot the changes to the reconstructed equilibrium profiles by running ORB5 for a single time step and taking moments of the temperature, density and

parallel flow. For this purpose, a series of simulations were run in ORB5 with $R_0 = 0.85$m, $R_0/a = 2$, $\bar{q} = 0.854 + 0.376\rho^2$, $T_i/T_e = 1$, $\rho_* = 1/140$. A background potential profile was also used, which was described earlier in section 3.8.1 (profile 1), that gave a peaked $E \times B$ profile as shown in figure 3.7. The ad-hoc equilibria was used for these simulations. The input temperature and density profiles used were the gradient plateau profiles shown in section 3.9.2, with $\Delta_s = 0.04$, $L_T = 1.5$ and $L_n = 0.807$ in units of a. These conditions are selected such that the inclusion of the strong-flow terms is justified. The weak and strong-flow equilibria can then be compared by turning on or off the strong-flow terms.

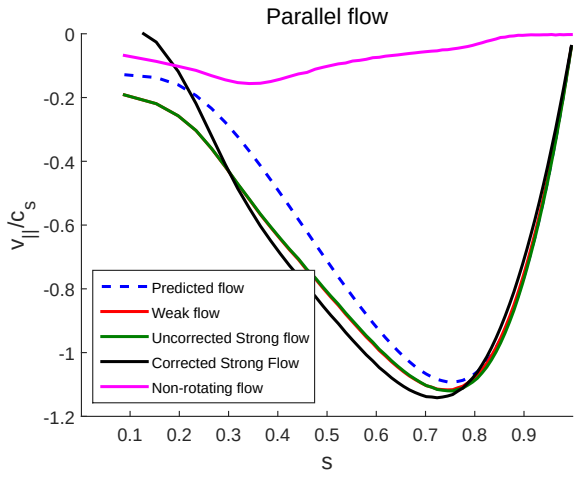

Figure 3.8: The reconstructed parallel flow profiles of the strong and weak-flow distributions. Also shown are the local limit predictions for the parallel flow, as expected from equation 3.37 and the parallel flow after the inclusion of the density correction, described in section 3.11.2.

The reconstructed parallel flow has been plotted in figure 3.8 which includes both the weak and strong-flow equilibria profiles (with and without correction) and also the predicted parallel flow as given by equation 3.37. It can be seen from this figure that the parallel flow as found in the local limit expansion has a reasonable match to the reconstructed parallel flow in both the weak and strong flow limit. Given the difference between the weak and strong flow plots, it can be seen that the strong-flow terms have little effect on the parallel flows. Additionally, figure 3.8 shows that the inclusion of the new density correction term will have an effect on the parallel flow, this change of parallel flow may cause some modifications in the physics but should still be within a reasonable threshold.

It can also be seen in the 'non-rotating' case plotted in figure 3.8 that there is a small parallel flow resulting from the profile gradients. This flow will still be

present in the rotating cases, and leads to some of the variation from the local limit prediction.

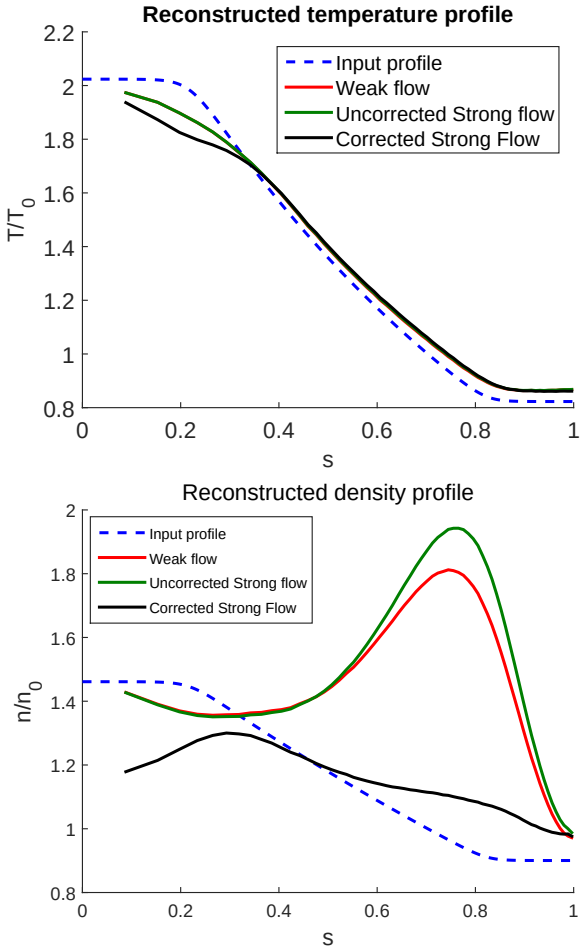

Figure 3.9: Reconstructed temperature and density profiles from an equilibrium distribution function which contains a radial electric field. Weak, strong-flow (corrected and uncorrected) and local profiles are shown. The input profiles are shown by the blue dashed line.

The flux surface average of temperature and density have both been plotted in figure 3.9 where it can be seen that the strong-flow terms make a significant change to the density. More importantly, this figure clearly displays the deviation of the equilibrium profiles from the input profiles. Even with the inclusion of the density correction, the density still deviates from the input noticeably (although less than with an uncorrected profile). However, it is to be expected that the density would not perfectly match the input, as the reconstructed equilibrium profiles of the canonical background distribution function are known in general to be flatter than

the input profiles [44].

3.11.4 Poloidal density variation

Although the density is input as a flux function and is commonly discussed as a flux surface average, the actual density does have a significant variation with poloidal angle when using a canonical distribution function. As a result, it is not accurate to consider it a flux function.

As expected, the reconstructed density of a local equilibrium distribution function can be seen in figure 3.10a to have no noticeable poloidal dependence, but this changes if the canonical equilibrium distribution function is used instead.

The poloidal variation can be seen in figures 3.10b and 3.10c to be substantial in both the weak and strong-flow form of equilibrium distribution function. As the density correction term is a flux function, the distribution function on the inboard and outboard side are affected in the same way. Once again, the density can be seen to be brought to noticeably lower levels with the inclusion of the density correction term; lowering a substantial peak in density on the outboard side. It is important that the density correction term not affect the poloidal dependence of the density, as a real system would also be expected to have a density which varies poloidally.

3.12 Implementation of Equations

3.12.1 Equations of Motion

$\mathrm{d}\mathbf{R}/\mathrm{d}t$ is implemented in ORB5 as linear and non-linear components in each direction, given by

$$\frac{\mathrm{d}A}{\mathrm{d}t} = \frac{\mathrm{d}\mathbf{R}}{\mathrm{d}t} \cdot \boldsymbol{\nabla} A \tag{3.46}$$

where A is the desired direction (s, θ_* or ζ).

The electric field is represented here as a background field, $\langle \mathbf{E} \rangle$, and a perturbed field $\langle \boldsymbol{\delta}\mathbf{E} \rangle$,

$$\langle \mathbf{E} + \boldsymbol{\delta}\mathbf{E} \rangle = \langle E_s + \delta E_s \rangle \boldsymbol{\nabla} s + \langle E_\theta + \delta E_\theta \rangle \boldsymbol{\nabla}\theta + \langle \delta E_\zeta \rangle \boldsymbol{\nabla}\zeta. \tag{3.47}$$

The relation

$$\mathbf{B} \times (\boldsymbol{\nabla} \times \mathbf{B}) = \mathbf{B} \times (\mu_0 \mathbf{j}) = -\mu_0 \boldsymbol{\nabla} p = -\mu_0 p'(\psi) \boldsymbol{\nabla}\psi \tag{3.48}$$

is used in the calculation of the equations of motion; where $p'(\psi)$ is the pressure gradient of the system.

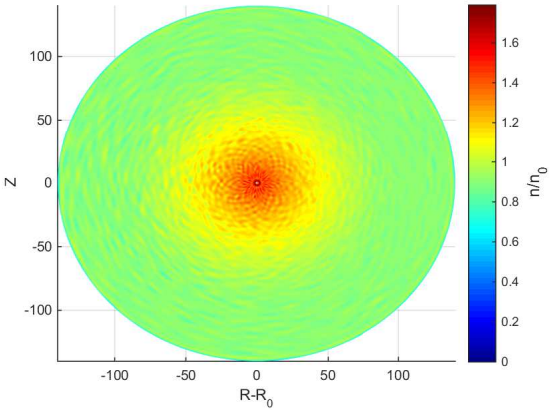

(a) Local distribution function (f_0 taken to be a function of ψ).

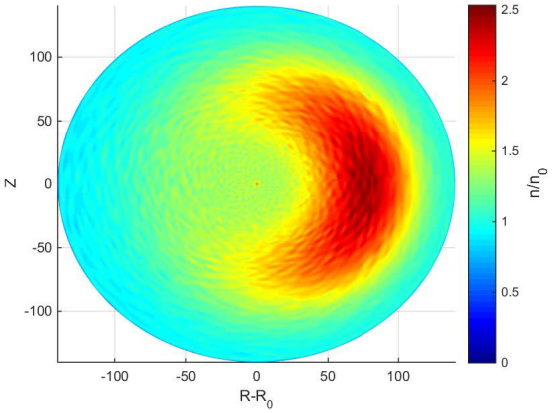

(b) Weak-flow form of distribution function. No modified density correction used.

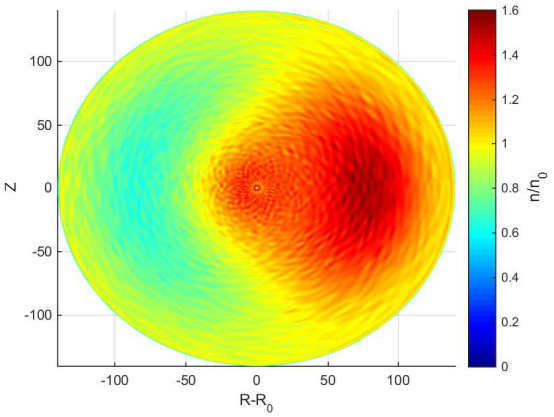

(c) The strong flow form of distribution function, with modified density correction term present.

Figure 3.10: The reconstructed 2D equilibrium density profiles for varying form of background distribution functions are shown. Only c) contains the modified density correction detailed in equation 3.44.

The form of the equations of motion used within ORB5 are given below, although it should be noted that the $\boldsymbol{\nabla} \times \mathbf{u}_E$ terms have not been fully expanded here due to their non-compact nature. Appendix C contains the full form of this component if desired.

The linear s-component of $\mathrm{d}\mathbf{R}/\mathrm{d}t$ is given by

$$\begin{aligned}\left.\frac{\mathrm{d}s}{\mathrm{d}t}\right|_0 =& \frac{m}{qBB^*_\parallel}\left(v_\parallel^2 + \frac{v_\perp^2}{2}\right)\frac{F}{J_{\theta_* s\zeta}}\frac{\partial B}{\partial \theta_*} - \langle E_{\theta_*}\rangle \frac{F(\psi)}{J_{\theta_* s\zeta}BB^*_\parallel} \\ &+ \frac{m}{2q}\frac{F}{BB^*_\parallel J_{\theta_* s\zeta}}\frac{\partial (u_E^2)}{\partial \theta_*} - \frac{mv_\parallel}{qB^*_\parallel}\left(\mathbf{b}\times[\mathbf{b}\times(\boldsymbol{\nabla}\times\mathbf{u_E})]\right)\cdot\boldsymbol{\nabla}s\end{aligned} \tag{3.49}$$

while the non-linear terms are

$$\left.\frac{\mathrm{d}s}{\mathrm{d}t}\right|_1 = \langle \delta E_\zeta\rangle \frac{\boldsymbol{\nabla}\psi\cdot\boldsymbol{\nabla}s}{R^2 BB^*_\parallel} - \langle \delta E_{\theta_*}\rangle \frac{F(\psi)}{J_{\theta_* s\zeta}BB^*_\parallel}. \tag{3.50}$$

Similarly, the linear θ_* component of $\mathrm{d}\mathbf{R}/\mathrm{d}t$

$$\begin{aligned}\left.\frac{\mathrm{d}\theta_*}{\mathrm{d}t}\right|_0 =& \frac{v_\parallel}{BJ_{\theta_*\psi\zeta}} - \frac{m}{qBB^*_\parallel}\left(v_\parallel^2 + \frac{v_\perp^2}{2}\right)\frac{F}{J_{\theta_* s\zeta}}\frac{\partial B}{\partial s} + \frac{mv_\parallel^2}{qB^3B^*_\parallel}\frac{F}{J_{\theta_*\psi\zeta}}\mu_0 p'(\psi) \\ &+ \langle E_s\rangle \frac{F(\psi)}{J_{\theta_* s\zeta}BB^*_\parallel} - \frac{m}{2q}\frac{F}{BB^*_\parallel J_{\theta_* s\zeta}}\frac{\partial (u_E^2)}{\partial s} - \frac{mv_\parallel}{qB^*_\parallel}\left(\mathbf{b}\times[\mathbf{b}\times(\boldsymbol{\nabla}\times\mathbf{u_E})]\right)\cdot\boldsymbol{\nabla}\theta_*\end{aligned} \tag{3.51}$$

and non-linear component

$$\left.\frac{\mathrm{d}\theta_*}{\mathrm{d}t}\right|_1 = \langle \delta E_\zeta\rangle \frac{\boldsymbol{\nabla}\psi\cdot\boldsymbol{\nabla}\theta_*}{R^2 BB^*_\parallel} + \langle \delta E_s\rangle \frac{F(\psi)}{J_{\theta_* s\zeta}BB^*_\parallel}. \tag{3.52}$$

Finally the components which describes the movement of particles in the toroidal direction are given by

$$\begin{aligned}\left.\frac{\mathrm{d}\zeta}{\mathrm{d}t}\right|_0 =& \frac{v_\parallel F}{BR^2} + \frac{m}{qR^2BB^*_\parallel}\left(v_\parallel^2 + \frac{v_\perp^2}{2}\right)\left[\frac{\partial B}{\partial s}(\boldsymbol{\nabla}\psi\cdot\boldsymbol{\nabla}s) + \frac{\partial B}{\partial \theta_*}(\boldsymbol{\nabla}\psi\cdot\boldsymbol{\nabla}\theta_*)\right] \\ &- \frac{mv_\parallel^2}{qB^3B^*_\parallel}\frac{|\nabla\psi|^2}{R^2}\mu_0 p'(\psi) - \langle E_s\rangle\frac{\boldsymbol{\nabla}\psi\cdot\boldsymbol{\nabla}s}{R^2BB^*_\parallel} - \langle E_{\theta_*}\rangle\frac{\boldsymbol{\nabla}\psi\cdot\boldsymbol{\nabla}\theta_*}{R^2BB^*_\parallel} \\ &+ \frac{m}{2q}\frac{1}{BB^*_\parallel R^2}\left(\boldsymbol{\nabla}\psi\cdot\boldsymbol{\nabla}s\frac{\partial(u_E^2)}{\partial s} + \boldsymbol{\nabla}\psi\cdot\boldsymbol{\nabla}\theta_*\frac{\partial(u_E^2)}{\partial\theta_*}\right) \\ &- \frac{mv_\parallel}{qB^*_\parallel}\left(\mathbf{b}\times[\mathbf{b}\times(\boldsymbol{\nabla}\times\mathbf{u_E})]\right)\cdot\boldsymbol{\nabla}\zeta\end{aligned} \tag{3.53}$$

and

$$\left.\frac{\mathrm{d}\zeta}{\mathrm{d}t}\right|_1 = -\langle \delta E_s \rangle \frac{\boldsymbol{\nabla}\psi \cdot \boldsymbol{\nabla} s}{R^2 B B^*_{\|}} - \langle \delta E_{\theta_*} \rangle \frac{\boldsymbol{\nabla}\psi \cdot \boldsymbol{\nabla}\theta_*}{R^2 B B^*_{\|}}. \tag{3.54}$$

The evolution of parallel velocity with time, including both linear and non-linear terms, is given by equation 3.55.

$$\begin{aligned}
\frac{\mathrm{d}v_{\|}}{\mathrm{d}t} =& -\frac{v_{\perp}^2}{2B^2 J_{\theta_* s\zeta}} \frac{\partial B}{\partial \theta_*} + \frac{m v_{\|} v_{\perp}^2}{2qB^*_{\|}} \frac{p'(\psi) F}{B^4 J_{\theta_* \psi\zeta}} \frac{\partial B}{\partial \theta_*} \\
&+ \left(\langle E_s + \delta E_s \rangle + \frac{m}{2q} \frac{\partial (u_E^2)}{\partial s} \right) \frac{v_{\|} F}{B^2 B^*_{\|} J_{\theta_* s\zeta}} + \left(\langle E_\theta + \delta E_\theta \rangle + \frac{m}{2q} \frac{\partial (u_E^2)}{\partial s} \right) \cdot \\
&\left\{ \frac{q}{mB J_{\theta_* \psi\zeta}} - \frac{v_{\|} F}{B^2 B^*_{\|} J_{\theta_* s\zeta}} \frac{\partial B}{\partial s} - \frac{v_{\|} p'(\psi) F}{B^3 B^*_{\|} J_{\theta_* \psi\zeta}} \right\} + \langle E_\zeta + \delta E_\zeta \rangle \left\{ \frac{qF}{mBR^2} \right. \\
&\left. + \frac{v_{\|}}{B^2 B^*_{\|} R^2} \left[\frac{\partial B}{\partial s} (\boldsymbol{\nabla} s \cdot \boldsymbol{\nabla}\psi) + \frac{\partial B}{\partial \theta_*} (\boldsymbol{\nabla}\psi \cdot \boldsymbol{\nabla}\theta_*) \right] + \frac{v_{\|} p'(\psi) |\nabla\psi|^2}{B^3 B^*_{\|} R^2} \right\} \\
&+ \boldsymbol{\nabla} s \cdot (\mathbf{b} \times [\mathbf{b} \times (\boldsymbol{\nabla} \times \mathbf{u_E})]) \left[\frac{1}{B^*_{\|}} \langle E_s + \delta E_s \rangle + \frac{\mu}{qB^*_{\|}} \frac{\partial B}{\partial s} + \frac{m}{2qB^*_{\|}} \frac{\partial (u_E^2)}{\partial s} \right] \\
&+ \boldsymbol{\nabla}\theta_* \cdot (\mathbf{b} \times [\mathbf{b} \times (\boldsymbol{\nabla} \times \mathbf{u_E})]) \left[\frac{1}{B^*_{\|}} \langle E_\theta + \delta E_\theta \rangle + \frac{\mu}{qB^*_{\|}} \frac{\partial B}{\partial \theta_*} + \frac{m}{2qB^*_{\|}} \frac{\partial (u_E^2)}{\partial \theta_*} \right] \\
&+ \boldsymbol{\nabla}\zeta \cdot (\mathbf{b} \times [\mathbf{b} \times (\boldsymbol{\nabla} \times \mathbf{u_E})]) \left[\frac{1}{B^*_{\|}} \langle \delta E_\zeta \rangle \right]
\end{aligned} \tag{3.55}$$

for which $\boldsymbol{\nabla} \times \mathbf{u}_E$ terms again remain un-expanded.

These equations are calculated for every marker at each time-step and used to evolve the system.

Pushing of markers

Most particles are pushed (evolved in time) in (s, θ_*) coordinates with the use of the equations of motion given above. However, at the magnetic axis, as $s \to 0$, a numerical instability is caused because $\mathrm{d}\theta_*/\mathrm{d}t \propto 1/s$ diverges. In order to solve this problem, a set of pseudo-Cartesian coordinates (ξ, η) are used which are defined as:

$$\xi = s \cos\theta_* \tag{3.56}$$

$$\eta = s \sin\theta_* \tag{3.57}$$

which give the equations of motion

$$\frac{\partial \xi}{\partial t} = \frac{\partial s}{\partial t}\cos\theta_* - s\frac{\partial \theta_*}{\partial t}\sin\theta_* \tag{3.58}$$

$$\frac{\partial \eta}{\partial t} = \frac{\partial s}{\partial t}\sin\theta_* - s\frac{\partial \theta_*}{\partial t}\cos\theta_*. \tag{3.59}$$

As $s\mathrm{d}\theta_*/\mathrm{d}t$ is not proportional to s, the singularity disappears. This new coordinate system is only used for markers with $s < s_{push}$, where s_{push} is an input parameter. All other particles still use the (s, θ_*) coordinate system.

The equations of motion and Vlasov equation are integrated in ORB5 with a fourth order Runge-Katta integrator.

Boundary Conditions

Markers that finish a time-step with $s > 1$ must be re-inserted into the plasma. This is done by reflecting the poloidal angle of the marker $\theta_* \to -\theta_*$. This may violate the conservation of the unperturbed invariants in an asymmetric up-down equilibria but will not do so in a symmetric up-down equilibria.

3.12.2 Vlasov Equation

The evolution of the distribution function follows from the description provided in section 2.7, but contains some deviations due to the definition of f_0 used in ORB5.

Here, the total electric field is given as $\mathbf{E_t}$, with background electric field as $\mathbf{E}$ and the perturbed electric field is $\boldsymbol{\delta}\mathbf{E}$:

$$\langle \mathbf{E_t} \rangle = -\boldsymbol{\nabla}\phi = -\boldsymbol{\nabla}\left(\Phi + \delta\phi\right)$$

$$\langle \mathbf{E} \rangle = -\boldsymbol{\nabla}\Phi$$

$$\langle \boldsymbol{\delta}\mathbf{E} \rangle = -\boldsymbol{\nabla}\left(\delta\phi\right)$$

which has components

$$\langle \mathbf{E} + \delta\mathbf{E} \rangle = \langle E_s + \delta E_s \rangle \boldsymbol{\nabla} s + \langle E_{\theta_*} + \delta E_{\theta_*} \rangle \boldsymbol{\nabla}\theta_* + \langle \delta E_\zeta \rangle \boldsymbol{\nabla}\zeta. \tag{3.60}$$

The distribution function used in ORB5, which contains the density correction term, is given by equation 3.44. We also note

$$\epsilon = \frac{m}{2}\left(v_\parallel^2 + u_E^2\right) + \mu B + q\Phi(\psi) - q\Phi(\Upsilon).$$

The equation for the weight evolution of a particle is derived from the Vlasov equation.

$$\frac{\mathrm{d}\delta f}{\mathrm{d}t} = -\frac{\mathrm{d}f_0}{\mathrm{d}t} = \tau\left(\mathbf{E_t}\right) = -\frac{\partial f_0}{\partial t} - \boldsymbol{\nabla} f_0 \cdot \frac{\mathrm{d}\mathbf{R}}{\mathrm{d}t} - \frac{\partial f_0}{\partial v_\parallel}\frac{\mathrm{d}v_\parallel}{\mathrm{d}t} - \frac{\partial f_0}{\partial \mu}\frac{\mathrm{d}\mu}{\mathrm{d}t} \tag{3.61}$$

$$\frac{\mathrm{d}\delta f}{\mathrm{d}t} = -\boldsymbol{\nabla} f_0 \cdot \frac{\mathrm{d}\mathbf{R}}{\mathrm{d}t} - \frac{\partial f_0}{\partial v_\parallel}\frac{\mathrm{d}v_\parallel}{\mathrm{d}t} \tag{3.62}$$

The background distribution function and the equations of motion have changed in ORB5 with the introduction of strong flows. As such, the weight evolution will also change from its weak-flow form.

We first take the derivatives of f_0 with respect to space and parallel velocity

$$\boldsymbol{\nabla} f_0 = f_0\kappa(\Upsilon)\boldsymbol{\nabla}\Upsilon - f_0\frac{m_i v_\perp^2}{2BT_i(\Upsilon)}\boldsymbol{\nabla}B - f_0\frac{m}{2T}\boldsymbol{\nabla}(u_E^2) + f_0\frac{q}{T(\Upsilon)}\langle\mathbf{E}\rangle \tag{3.63}$$

$$\frac{\partial f_0}{\partial v_\parallel} = f_0\kappa(\Upsilon)\frac{\partial\Upsilon}{\partial v_\parallel} - f_0\frac{mv_\parallel}{T} \tag{3.64}$$

for which $\kappa(\Upsilon)$ is defined as

$$\begin{aligned}\kappa(\Upsilon) &\equiv \frac{\partial f_0}{\partial\Upsilon} \\ &= \left(\frac{n_0'(\Upsilon)}{n_0(\Upsilon)} - \frac{3T_i'(\Upsilon)}{2T_i(\Upsilon)} + \frac{\epsilon}{T_i(\Upsilon)^2}T_i'(\Upsilon) + \frac{q}{T(\Upsilon)}\frac{\partial\Phi(\Upsilon)}{\partial\Upsilon}\right)\end{aligned} \tag{3.65}$$

where n_0' and T_i' denote the partial derivatives of n_0 and T_i with respect to Υ.

Using equations 3.63 and 3.64, we can calculate the change of δf with time as

$$\begin{aligned}\frac{\mathrm{d}\delta f}{\mathrm{d}t} =& -f_0\kappa(\Upsilon)\left\{\boldsymbol{\nabla}\Upsilon\cdot\frac{\mathrm{d}\mathbf{R}}{\mathrm{d}t} + \frac{\partial\Upsilon}{\partial v_\parallel}\frac{\mathrm{d}v_\parallel}{\mathrm{d}t}\right\} + f_0\frac{m}{2T}\boldsymbol{\nabla}(u_E^2)\cdot\frac{\mathrm{d}\mathbf{R}}{\mathrm{d}t} \\ &- f_0\frac{q}{T}\langle\mathbf{E}\rangle\cdot\frac{\mathrm{d}\mathbf{R}}{\mathrm{d}t} + f_0\frac{\mu}{T}\boldsymbol{\nabla}B\cdot\frac{\mathrm{d}\mathbf{R}}{\mathrm{d}t} + f_0\frac{mv_\parallel}{T}\frac{\mathrm{d}v_\parallel}{\mathrm{d}t}.\end{aligned} \tag{3.66}$$

By expanding the last two terms of equation 3.66, it is possible to simplify the

weight evolution of the markers further. The expansion will give

$$\begin{aligned}\frac{\mathrm{d}\delta f}{\mathrm{d}t} =& - f_0\kappa(\Upsilon)\left\{\boldsymbol{\nabla}\Upsilon\cdot\frac{\mathrm{d}\mathbf{R}}{\mathrm{d}t}+\frac{\partial\Upsilon}{\partial v_\parallel}\frac{\mathrm{d}v_\parallel}{\mathrm{d}t}\right\}+f_0\frac{m}{2T}\boldsymbol{\nabla}(u_E^2)\cdot\frac{\mathrm{d}\mathbf{R}}{\mathrm{d}t}-f_0\frac{q}{T}\langle\mathbf{E}\rangle\cdot\frac{\mathrm{d}\mathbf{R}}{\mathrm{d}t}\\ &+f_0\frac{1}{T}\left\{v_\parallel\mu\mathbf{b}\cdot\boldsymbol{\nabla}B-\frac{m}{qBB_\parallel^*}\mu v_\parallel^2\boldsymbol{\nabla}B\cdot[\mathbf{b}\times(\mathbf{b}\times[\boldsymbol{\nabla}\times\mathbf{B}])]\right.\\ &+\mu\langle\mathbf{E_t}\rangle\cdot\frac{\mathbf{B}\times\boldsymbol{\nabla}B}{BB_\parallel^*}-\frac{m\mu}{2qB_\parallel^*}\boldsymbol{\nabla}(u_E^2)\cdot(\mathbf{b}\times\boldsymbol{\nabla}B)\\ &\left.-\frac{mv_\parallel\mu}{qB_\parallel^*}\boldsymbol{\nabla}B\cdot[\mathbf{b}\times(\mathbf{b}\times[\boldsymbol{\nabla}\times\mathbf{u_E}])]\right\}-f_0\frac{mv_\parallel}{T}\left\{\frac{\mathbf{b}}{m}+\frac{v_\parallel}{qBB_\parallel^*}\mathbf{b}\times\boldsymbol{\nabla}B\right.\\ &\left.-\frac{v_\parallel}{qBB_\parallel^*}\mathbf{b}\times[\mathbf{b}\times(\boldsymbol{\nabla}\times\mathbf{B})]-\frac{1}{qB_\parallel^*}\mathbf{b}\times[\mathbf{b}\times(\boldsymbol{\nabla}\times\mathbf{u_E})]\right\}\cdot\\ &\left\{\mu\boldsymbol{\nabla}B-q\langle\mathbf{E_t}\rangle+\frac{m}{2}\boldsymbol{\nabla}(u_E^2)\right\}\end{aligned} \tag{3.67}$$

which simplifies to give equation 3.68.

$$\begin{aligned}\frac{\mathrm{d}\delta f}{\mathrm{d}t} =& - f_0\kappa(\Upsilon)\left\{\boldsymbol{\nabla}\Upsilon\cdot\frac{\mathrm{d}\mathbf{R}}{\mathrm{d}t}+\frac{\partial\Upsilon}{\partial v_\parallel}\frac{\mathrm{d}v_\parallel}{\mathrm{d}t}\right\}+f_0\frac{m}{2T}\boldsymbol{\nabla}(u_E^2)\cdot\frac{\mathrm{d}\mathbf{R}}{\mathrm{d}t}-f_0\frac{q}{T}\langle\mathbf{E}\rangle\cdot\frac{\mathrm{d}\mathbf{R}}{\mathrm{d}t}\\ &+f_0\frac{\mu}{T}\langle\mathbf{E}+\boldsymbol{\delta}\mathbf{E}\rangle\cdot\frac{\mathbf{B}\times\boldsymbol{\nabla}B}{BB_\parallel^*}-f_0\frac{m\mu}{2qB_\parallel^*T}\boldsymbol{\nabla}(u_E^2)\cdot(\mathbf{b}\times\boldsymbol{\nabla}B)-f_0\frac{mv_\parallel}{T}\left\{\frac{\mathbf{b}}{m}\right.\\ &\left.+\frac{v_\parallel}{qBB_\parallel^*}\mathbf{b}\times\boldsymbol{\nabla}B-\frac{v_\parallel}{qBB_\parallel^*}\mathbf{b}\times[\mathbf{b}\times(\boldsymbol{\nabla}\times\mathbf{B})]-\frac{1}{qB_\parallel^*}\mathbf{b}\times[\mathbf{b}\times(\boldsymbol{\nabla}\times\mathbf{u_E})]\right\}\cdot\\ &\left\{-q\langle\mathbf{E}+\boldsymbol{\delta}\mathbf{E}\rangle+\frac{m}{2}\boldsymbol{\nabla}(u_E^2)\right\}\end{aligned} \tag{3.68}$$

By comparing the last dot product in equation 3.68 with $\mathrm{d}\mathbf{R}/\mathrm{d}t$ it is possible to re-write as

$$\begin{aligned}\frac{\mathrm{d}\delta f}{\mathrm{d}t} =& - f_0\kappa(\Upsilon)\left\{\boldsymbol{\nabla}\Upsilon\cdot\frac{\mathrm{d}\mathbf{R}}{\mathrm{d}t}+\frac{\partial\Upsilon}{\partial v_\parallel}\frac{\mathrm{d}v_\parallel}{\mathrm{d}t}\right\}+f_0\frac{m}{2T}\boldsymbol{\nabla}(u_E^2)\cdot\frac{\mathrm{d}\mathbf{R}}{\mathrm{d}t}-f_0\frac{q}{T}\langle\mathbf{E}\rangle\cdot\frac{\mathrm{d}\mathbf{R}}{\mathrm{d}t}\\ &-f_0\frac{m}{2T}\boldsymbol{\nabla}(u_E^2)\cdot\frac{\mathrm{d}\mathbf{R}}{\mathrm{d}t}+f_0\frac{q}{T}\langle\mathbf{E}+\boldsymbol{\delta}\mathbf{E}\rangle\cdot\frac{\mathrm{d}\mathbf{R}}{\mathrm{d}t}\\ &+f_0\frac{1}{BB_\parallel^*}\frac{m}{2T}\underbrace{\left\{\boldsymbol{\nabla}(u_E^2)\cdot(\langle\mathbf{E}\rangle\times\mathbf{B})-\langle\mathbf{E}\rangle\cdot\left(\mathbf{B}\times\boldsymbol{\nabla}(u_E^2)\right)\right\}}_{=0},\end{aligned} \tag{3.69}$$

thus giving equation 3.70 and subsequently equation 3.71.

$$\frac{\mathrm{d}\delta f}{\mathrm{d}t} = -f_0\kappa(\Upsilon)\left\{\boldsymbol{\nabla}\Upsilon\cdot\frac{\mathrm{d}\mathbf{R}}{\mathrm{d}t} + \frac{\partial\Upsilon}{\partial v_\parallel}\frac{\mathrm{d}v_\parallel}{\mathrm{d}t}\right\} + f_0\frac{q}{T}\langle\boldsymbol{\delta}\mathbf{E}\rangle\cdot\left.\frac{\mathrm{d}\mathbf{R}}{\mathrm{d}t}\right|_0 \tag{3.70}$$

$$\frac{\mathrm{d}\delta f}{dt} = \tau(\mathbf{E}_t) = -f_0\kappa(\Upsilon)\frac{\mathrm{d}\Upsilon}{\mathrm{d}t} + f_0\frac{q}{T}\langle\delta\mathbf{E}\rangle\cdot\left.\frac{\mathrm{d}\mathbf{R}}{\mathrm{d}t}\right|_0 \tag{3.71}$$

Equation 3.71 shows the final form of the weight evolution equation which ORB5 will use to calculate the change of particle weights.

It is also possible to derive the weight evolution equation through a ψ_c and ϵ based calculation, with the rate of change of the Hamiltonian being evaluated directly.

3.12.3 Loading of the initial conditions

Before the particles can be moved and the fields calculated, the markers must first be loaded into the system itself. This process involves placing the markers in phase space (assigning a position and velocities to each) and assigning the initial weights of the markers.

Discretisation of markers

In ORB5, the perturbed distribution function, δf, is discretised in phase space with N markers.

$$\delta f = \frac{N_{ph}}{N}\sum_{p=1}^{N}\frac{1}{2\pi B_\parallel^*}w_p(t)\delta\left(\mathbf{R}-\mathbf{R}_p(t)\right)\delta\left(v_\parallel - v_{\parallel,p}(t)\right)\delta\left(\mu-\mu_p(t_0)\right) \tag{3.72}$$

Here, N_{ph} is the number of physical particles represented by the simulation and $w_p(t)$ is the weight of the p^{th} marker, which also has position $\mathbf{R}_p(t), v_{\parallel,p}(t), \mu_p(t_0)$ in phase space at time t. The time at the beginning of the simulation is defined as t_0. Although the perturbed distribution function should be continuous in phase space, this form represents the distribution function with delta functions and so is not smooth.

Over a small volume in phase space, Ω_p, the perturbed distribution function is assumed to be constant. Integrating over this volume and using the Vlasov equation, equation 2.81, it can be found that

$$\delta f_p\Omega_p = \frac{N_{ph}}{N}w_p(t)$$

$$\frac{\mathrm{d}w_p(t)}{\mathrm{d}t} = \frac{N}{N_{ph}}\tau_p\Omega_p \tag{3.73}$$

where τ_p is a function representing the right hand side of the Vlasov equation for the p^{th} marker, as shown in 3.61. The phase space volume is given by

$$\Omega_p = B_{\parallel}^{*}\frac{\mathrm{d}\mathbf{R}\mathrm{d}v_{\parallel}\mathrm{d}v_{\perp}}{\mathrm{d}N} \tag{3.74}$$

and $\mathrm{d}N$ is the number of markers found in an infinitesimal volume of phase space and can be freely specified.

$$\mathrm{d}N = \frac{N}{N_{ph}}f_L\left(\mathbf{R}, v_{\parallel}, \mu\right)J\left(s, \theta_*, \zeta\right)\mathrm{d}s\mathrm{d}\theta_*\mathrm{d}v_{\parallel}\mathrm{d}v_{\perp}\mathrm{d}\alpha \tag{3.75}$$

ORB5 uses a scheme known as specified loading for which:

$$f_L(\mathbf{R}) = f_L(s) = K\left[1 - f_g + f_g\exp\left(\frac{s - s_0}{\Delta s}\right)\right] \equiv Kp(s) \tag{3.76}$$

where s_0 and Δs are input parameters. f_g is also an input parameter with value between 0 and 1. K is a normalization constant defined by

$$K = \frac{1}{\int p(s)J_{s\theta_*\zeta}\left(s, \theta_*\right)\mathrm{d}s\mathrm{d}\theta_*\mathrm{d}\zeta}. \tag{3.77}$$

The specified loading has the advantage that it loads more markers around s_{peak}, which is the location of the peak gradient of the temperature profile and therefore the point of strongest drive in the ITG mode. In this thesis, $f_g = 0$ has been used, which leads to uniform loading of the markers.

Within ORB5, the velocities are loaded uniformly in phase space up to a cut-off defined by $v_{max} = \kappa_v c_s$, where $\kappa_v = 5$ and c_s is the thermal velocity of the nominal ion species used in normalization.

Weight Initialisation

As well as loading the markers in phase space, the weights of each marker must also be initialised. The simplest method for this is white noise initialisation, where all markers have a weight assigned psuedo-randomly. However, this has the downside that any physical modes will take a long time to develop in the initial stages of the simulation. Therefore, more advanced weight initialization methods assign weights so that the resulting configuration is close to that of a physical mode. The simulation will still need time to develop, but the process will be substantially quicker.

Several of these methods have been implemented in ORB5. The 'GENE' perturbation is a commonly used weight initialization which is given by

$$\delta f(t_0) = \sum_{n_j=n_{min}}^{n_{max}} A_0 \cos\left\{n_j\left[\zeta(t_0) - q\theta_*(t_0)\right]\right\} \times \exp\left\{-\frac{1}{2}\left[\left(\frac{\rho(t_0)-0.5}{\Delta_G}\right)^2 + \left(\frac{4n_j}{n_{max}}\right)^2 + \left(\frac{4\theta_*(t_0)}{\pi}\right)^2\right]\right\} \tag{3.78}$$

where A_0 is the size of the initial perturbation and Δ_G, chosen to be $\Delta_G = 0.225a$, is the radial width of the Gaussian shaped perturbation. It is also possible to apply a tilt to the perturbation in the $s-\zeta$ plane; although this has not been used in this thesis. n_{min} and n_{max} are input parameters which represent the lowest and highest toroidal modes to have an initial perturbation applied. If this method is used, the initial perturbation of the system will already be close to the physical modes. The initial perturbation of the system, before any modes have begun to grow, will also be independent of the number of markers.

3.12.4 Poisson Equation

The Poisson equation in ORB5 is solved with the use of a finite elements method [57]. The fundamental idea is to discretised the perturbed potential (given here as ϕ) on a 3D (s, θ_*, ζ) grid:

$$\phi(\mathbf{x}, t) = \sum_{\mu} \phi_\mu(t)\Lambda_\mu(\mathbf{x}) \tag{3.79}$$

where $\phi_\mu(t)$ are real numbers, μ represents the indexes (j, k, l) and $\Lambda_\mu(\mathbf{x})$ are the tensor products of 1D B-splines

$$\Lambda_\mu(\mathbf{x}) = \Lambda_j^p(s)\Lambda_k^p(\theta_*)\Lambda_l^p(\zeta). \tag{3.80}$$

B-splines are polynomial functions of a specified order and in ORB5 can be either linear, quadratic or cubic. They are defined on a (N_s, N_θ, N_ζ) grid, known as the field grid. It is important to consider the appropriate size of field grid to use, as the spacing of the grid changes the resolution of field fluctuations which are kept in simulations. Fluctuations on a scale smaller than the space between grid points will not be retained when evolving the system. However, too many grid points will greatly slow the simulation for little benefit. Generally, the field grid will also scale with the system size ρ_* as a larger system requires more grid points if it is to keep

a sufficient field resolution. With the use of the Galerkin method, a linear system can be gained from equation 3.79 [58]. This gives a system:

$$\sum_{\mu} A_{\mu\nu}\phi_{\mu}(t) = b_{\nu}(t) \tag{3.81}$$

where

$$A_{\mu\nu} = \int \frac{n_0(\psi)}{Z_i T_e(\psi)} \left[\Lambda_{\mu}(\mathbf{x})\Lambda_{\nu}(\mathbf{x}) - \bar{\Lambda}_{\mu}(s)\bar{\Lambda}_{\nu}(s)\right] \mathrm{d}\mathbf{x} + \frac{n_0(\psi)}{B\Omega_{ci}} \boldsymbol{\nabla}_{\perp}\Lambda_{\mu}(\mathbf{x}) \cdot \boldsymbol{\nabla}_{\perp}\Lambda_{\nu}(\mathbf{x}) \tag{3.82}$$

$$b_{\nu}(t) = \frac{N_{ph}}{N} \sum_{p=1}^{N} \frac{w_p(t)}{2\pi} \int_0^{2\pi} \Lambda_{\nu}\left(\mathbf{R}_p + \boldsymbol{\rho}_{L,i,p}(\alpha)\right) \mathrm{d}\alpha. \tag{3.83}$$

Note that $A_{\mu\nu}$ is a real, symmetrical matrix which allows for the use of relatively cheap numerical methods when solving.

The construction of $b_{\nu}(t)$ is known as charge assignment, and the projection onto the finite element basis is the main source of numerical noise in simulations, due to the particle discritisation of δf. Higher order splines give a reduction of this statistical noise. The perpindicular gradients seen in equation 3.82 can be approximated as lying on the poloidal plane, so that $\boldsymbol{\nabla}_{\perp} \simeq \boldsymbol{\nabla}_{pol} = \boldsymbol{\nabla} s \frac{\partial}{\partial s} + \boldsymbol{\nabla}\theta_* \frac{\partial}{\partial \theta_*}$ [59]. As the system is axisymmetric, the equation given after this approximation can be decoupled in ζ and a discrete Fourier transform can be applied to ϕ_{μ} and b_{ν} in equation 3.81 to give, in Fourier space:

$$\sum_{\mu} A_{\mu\nu}\hat{\phi}_{\mu}^{(n)}(t) = \frac{\hat{b}_{\nu}^{(n)}(t)}{M^{(n),p}}. \tag{3.84}$$

Here, (μ, ν) now stand for 2D indices and $\hat{\phi}_{\mu}^{(n)}$ and $\hat{b}_{\nu}^{(n)}$ are Fourier coefficients of ϕ_{μ} and b_{ν}. $M^{(n),p}$ is defined by

$$M^{(n),p} = \sum_{l'=1}^{N_{\zeta}} \int \Lambda_{l'}^{p}(\zeta)\Lambda_{l}^{p}(\zeta) \exp\left(\frac{2\pi i}{N_{\zeta}} n(l'-l)\right) \mathrm{d}\zeta \tag{3.85}$$

and can be computed analytically for any spline of order p.

The Dirichlet boundary condition is imposed at the edge so that

$$\phi(s = 1, \theta_*, \zeta, t) = 0$$

and the regularity condition is applied at the axis

$$\phi(s=0,\theta_*=0,\zeta,t)=\phi(s=0,\theta_*,\zeta,t).$$

This system of equations may then be solved using a direct solver, LAPACK [60]. Alternatively, to reduce the memory storage, the parallel solver ScaLAPACK [61] routines have been implemented in ORB5.

Field-aligned Fourier filter

By applying a Fourier filter on the discretised perturbed density, we can reduce the noise in the simulation. Additionally, this allows us to select a single toroidal mode in the linear simulations. The advantage of a Fourier filter is that physically irrelevant modes can be removed from the simulation. A Fourier filter is applied by first performing a 2D Fourier transform and then applying a filter, $\mathcal{F}$, which acts to remove the unwanted modes.

$$\mathcal{F}\rho(\mathbf{R},\mathbf{v},t)=\sum_{m,n}\hat{\mathcal{F}}_{m,n}\hat{\rho}_{m,n}(s,t)e^{im\theta_*}e^{in\zeta} \tag{3.86}$$

One of the simplest filters is a square filter that filters out any modes that do not lie within a window, $[n_{min}:n_{max}]\times[m_{min}:m_{max}]$, however this type of filter is inconsistent with the gyrokinetic ordering [62]. Therefore, a field-aligned Fourier filter is used which suppresses high $k_\parallel$ modes and keeps poloidal modes with $m=(-nq(s)\pm\Delta m)$, where $\Delta m=5$. This field-aligned filter is given by

$$\hat{\mathcal{F}}_{m,n}(s)=\mathcal{H}\left(m-[-nq(s)-\Delta m]\right)\mathcal{H}\left([-nq(s)+\Delta m]-m\right)\mathcal{H}\left(n-n_{min}\right)\mathcal{H}\left(n_{max}-n\right) \tag{3.87}$$

where $\mathcal{H}$ is the Heaviside function.

It can be shown that the noise in a simulation scales with the square root of the number of modes in the system [19]. As this filter reduces the number of modes in the system, it also acts to reduce the noise.

3.13 Sources and noise control

Global gyrokinetic simulations, such as those performed by ORB5, suffer from statistical noise which can make it difficult to make valid quantitative predictions [63]. Therefore, some method to control and minimise the noise generated during the course of the simulations is desired, but it is also extremely important that these

methods used do not affect the physical results that are found from the simulation.

The measurement of the noise in simulations is inherent to the field-aligned Filter ($\mathcal{F}$) used to solve the Poisson equation. After performing a poloidal and toroidal Fourier transform of the perturbed density δn_i, the components within the filter can be summed over the magnetic surfaces and then normalised to give a measurement of the signal. Similarly, the noise can be measured by summing the components outside the filter.

$$\text{Signal} = \frac{\frac{1}{a}\int_0^a \sum_{(n,m)\in\mathcal{F}} |\delta n^{(n,m)}(r)|^2}{\sum_{(n,m)\in\mathcal{F}}} \tag{3.88}$$

$$\text{Noise} = \frac{\frac{1}{a}\int_0^a \sum_{(n,m)\notin\mathcal{F}} |\delta n^{(n,m)}(r)|^2}{\sum_{(n,m)\notin\mathcal{F}}} \tag{3.89}$$

There are two methods of noise control that have been implemented in ORB5. The first method, the Krook operator, adds a source term to the Vlasov equation which introduces an artificial damping that allows the distribution function to relax towards its equilibrium state. However, to prevent the damping of the zonal flows a correction term is also added. This method and its introduction to ORB5 are detailed by McMillan [64]. A source operator, S, is added to the Vlasov equation as

$$\frac{\mathrm{d}\delta f\left(\mathbf{R}, v_\parallel, \mu, t\right)}{\mathrm{d}t} = \tau\left(\mathbf{E}\right) + S\left(\mathbf{R}, v_\parallel, \mu\right) \tag{3.90}$$

which acts on all flux surfaces to modify the marker weights. One major disadvantage of the Krook method is that it only works for collision-less simulations.

This noise control scheme is not utilised in this thesis but the form given in equation 3.90 is also valid for the addition of other sources to simulations, such as a heat source which introduces a term that is dependant upon a user-defined parameter γ_H. More discussion of this subject is later presented in section 6.2.2.

The second method of noise control within ORB5, and the one used for simulations in this thesis, is the coarse-graining method. It was first proposed by Brunner [65] and later expanded upon by Vernay [66]. The full details of the coarse-graining method utilized by ORB5 are detailed in a second paper published by Vernay [63]. The method works to reduce the numerical noise by filtering the high-k modes in 5D space for collisionless runs and by reducing the weight spreading in collisional simulations. At each time step all markers are binned in the 5D gyrokinetic phase space and then the weights of the markers are averaged with the other markers present in the same bin. An upper limit is effectively imposed on

the bin sizes as this is an unphysical effect and it should therefore only be imposed on scales smaller than those relevant to the turbulence of the system. Additionally, there is a lower limit on the number of markers within each bin at the end of each time-step imposed. This is because there must be at least two markers within each bin when the averaging is performed. However, in practice this marker limit can be reduced by not performing the coarse-graining every time-step. Often, the coarse-graining is performed only every ten time steps which reduces the required number of markers to one tenth of what it would otherwise be. It has been found that the coarse-graining noise control scheme enables a higher signal-to-noise ratio than the Krook operator when a similar effective unphysical damping is used with each method.

3.14 Shielding of potential at tokamak edge

At the plasma edge, the condition $\phi = 0$ is imposed for solutions of the Poisson equation. Unfortunately, in non-linear simulations when there is a particle flux in the region near to the last closed flux surface this can lead to instabilities. The particle flux can cause particles to move towards the boundary of the simulation domain. When markers move to the edge it will lead to non-zero weights in the edge domain, which will in turn lead to the Poisson equation not being solved exactly. This results in the generation of spurious electric fields at the edge. To help reduce this issue, an artificial shielding term is introduced to the density in the Poisson equation which will reduce the calculated potential. This density shielding term raises the effective background density near the edge, reducing the importance of any fluctuations.

The density is modified as

$$n_0(\psi) \rightarrow n_0(\psi) n_{sh}. \tag{3.91}$$

The shielding term, n_{sh}, is given by

$$n_{sh} = 1 + \kappa_{sh} \sinh\left(\frac{\psi}{\Delta_{sh}}\right) \left[\sinh\left(\frac{1}{\Delta_{sh}}\right)\right]^{-1} \tag{3.92}$$

where Δ_{sh} and $\kappa_{sh} = \frac{a}{L_{n,sh}}$ are input parameters. This shielding term will be 1 for most of the simulation domain but for a small region at the edge which is defined by Δ_{sh}. The shielding is shown in figure 3.11.

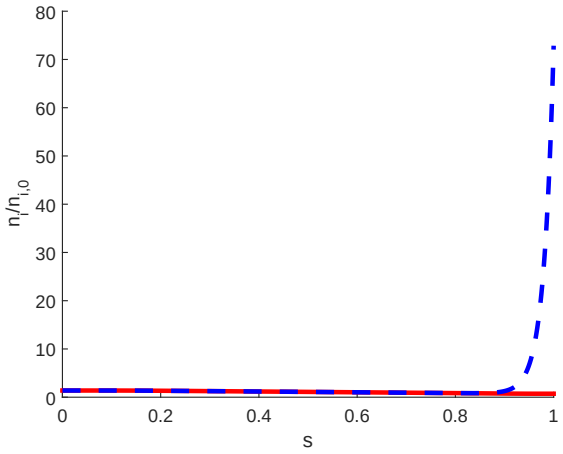

Figure 3.11: Normalized density plotted without (solid red line) and with (dashed blue line) the density shielding term present. The parameters for the shielding term used here are $\kappa_{sh} = 100$ and $\Delta_{sh} = 0.02$.

3.15 Conserved Properties

After modification of the equations of motion, it is important to check that the motion of the particles in an unperturbed system still behaves as expected. One of the most effective ways to do this is to check the change of the simulations constants of motion over time. If the variation is not acceptably small then it is apparent that the implementation has an error.

3.15.1 Conservation of particle quantities

Each individual particle (or marker) should conserve the three constants of motion from Hahm's gyrokinetic equations; magnetic moment, μ, particle energy, ϵ and the toroidal canonical momentum, ψ_c. The magnetic moment will automatically be conserved as this quantity is explicitly set to a constant for each marker and the energy conservation follows from the gyrokinetic Lagrangian and Noether's theorem [67].

We first confirm that ϵ and ψ_c should remain constant with time in an unperturbed system. Here, the equations of motion have been split into their unperturbed and perturbed components, denoted with a 0 or 1 respectively. The nonlinear components of the equations of motion contain any terms dependant on the perturbed electric potential, $\delta\phi$, while the background potential, Φ, appears in both the linear

and non-linear components.

$$\frac{\mathrm{d}\mathbf{R}}{\mathrm{d}t} = \left.\frac{\mathrm{d}\mathbf{R}}{\mathrm{d}t}\right|_0 + \left.\frac{\mathrm{d}\mathbf{R}}{\mathrm{d}t}\right|_1, \qquad \frac{\mathrm{d}v_\parallel}{\mathrm{d}t} = \left.\frac{\mathrm{d}v_\parallel}{\mathrm{d}t}\right|_0 + \left.\frac{\mathrm{d}v_\parallel}{\mathrm{d}t}\right|_1$$

The Hamiltonian (energy) of each particle is given by

$$\epsilon = \frac{m}{2}\left(v_\parallel^2 + u_E^2\right) + \mu B + q\Phi\left(\psi\right). \tag{3.93}$$

By taking the time derivative of ϵ we find how it evolves with time,

$$\begin{aligned}\frac{\mathrm{d}\epsilon}{\mathrm{d}t} &= mv_\parallel\frac{\mathrm{d}v_\parallel}{\mathrm{d}t} + \frac{m}{2}\frac{\mathrm{d}\left(u_E^2\right)}{\mathrm{d}t} + \mu\frac{\mathrm{d}B}{\mathrm{d}t} + q\frac{\mathrm{d}\Phi}{\mathrm{d}t} \\ &= mv_\parallel\frac{\mathrm{d}v_\parallel}{\mathrm{d}t} + \frac{m}{2}\boldsymbol{\nabla}\left(u_E^2\right)\cdot\frac{\mathrm{d}\mathbf{R}}{\mathrm{d}t} + \mu\boldsymbol{\nabla}B\cdot\frac{\mathrm{d}\mathbf{R}}{\mathrm{d}t} + q\boldsymbol{\nabla}\Phi\cdot\frac{\mathrm{d}\mathbf{R}}{\mathrm{d}t} \\ &= mv_\parallel\frac{\mathrm{d}v_\parallel}{\mathrm{d}t} + \left\{q\boldsymbol{\nabla}\Phi + \mu\boldsymbol{\nabla}B + \frac{m}{2}\boldsymbol{\nabla}\left(u_E^2\right)\right\}\cdot\frac{\mathrm{d}\mathbf{R}}{\mathrm{d}t}\end{aligned} \tag{3.94}$$

where the evolution of a quantity that is only dependant on space is given by

$$\frac{\mathrm{d}\mathbf{A}}{\mathrm{d}t} = \boldsymbol{\nabla}A\cdot\frac{\mathrm{d}\mathbf{R}}{\mathrm{d}t}.$$

However, our interest is in the unperturbed system. The unperturbed evolution of ϵ is given by

$$\left.\frac{\mathrm{d}\epsilon}{\mathrm{d}t}\right|_0 = mv_\parallel\left.\frac{\mathrm{d}v_\parallel}{\mathrm{d}t}\right|_0 + \left\{q\boldsymbol{\nabla}\Phi + \mu\boldsymbol{\nabla}B + \frac{m}{2}\boldsymbol{\nabla}\left(u_E^2\right)\right\}\cdot\left.\frac{\mathrm{d}\mathbf{R}}{\mathrm{d}t}\right|_0. \tag{3.95}$$

Expansion of the first term in equation 3.95 is given by equation 3.96,

$$\begin{aligned}mv_\parallel\left.\frac{\mathrm{d}v_\parallel}{\mathrm{d}t}\right|_0 = -\left\{q\boldsymbol{\nabla}\Phi + \mu\boldsymbol{\nabla}B + \frac{m}{2}\boldsymbol{\nabla}\left(u_E^2\right)\right\}\cdot\Bigg(&v_\parallel\mathbf{b} + \frac{mv_\parallel^2}{qBB_\parallel^*}\left(\mathbf{b}\times\boldsymbol{\nabla}B\right) \\ &-\frac{mv_\parallel^2}{qBB_\parallel^*}\mathbf{b}\times\left[\mathbf{b}\times\left(\boldsymbol{\nabla}\times\mathbf{B}\right)\right] - \frac{mv_\parallel}{qB_\parallel^*}\mathbf{b}\times\left[\mathbf{b}\times\left(\boldsymbol{\nabla}\times\mathbf{u_E}\right)\right]\Bigg)\end{aligned} \tag{3.96}$$

which when substituted back in will cancel with many of the components in the second term of equation 3.95 to give equation 3.97.

$$\begin{aligned}\left.\frac{\mathrm{d}\epsilon}{\mathrm{d}t}\right|_0 = \left\{q\boldsymbol{\nabla}\Phi + \mu\boldsymbol{\nabla}B + \frac{m}{2}\boldsymbol{\nabla}\left(u_E^2\right)\right\}\cdot\Bigg(&\frac{\mu}{qB_\parallel^*}\mathbf{b}\times\boldsymbol{\nabla}B + \frac{1}{B_\parallel^*}\mathbf{b}\times\boldsymbol{\nabla}\Phi \\ &+\frac{m}{2qB_\parallel^*}\mathbf{b}\times\boldsymbol{\nabla}\left(u_E^2\right)\Bigg)\end{aligned} \tag{3.97}$$

Expansion of equation 3.97 gives

$$\begin{aligned}\left.\frac{\mathrm{d}\epsilon}{\mathrm{d}t}\right|_0 = &\frac{\mu}{B}\Big\{\boldsymbol{\nabla}\Phi\cdot(\mathbf{b}\times\boldsymbol{\nabla}B)+\boldsymbol{\nabla}B\cdot(\mathbf{b}\times\boldsymbol{\nabla}\Phi)\Big\}\\ &+\frac{m}{2B_\parallel^*}\Big\{\boldsymbol{\nabla}\Phi\left(\mathbf{b}\times\boldsymbol{\nabla}\left(u_E^2\right)\right)+\boldsymbol{\nabla}\left(u_E^2\right)\cdot(\mathbf{b}\times\boldsymbol{\nabla}\Phi)\Big\}\\ &+\frac{m\mu}{2qB_\parallel^*}\Big\{\boldsymbol{\nabla}B\cdot\left(\mathbf{b}\times\boldsymbol{\nabla}\left(u_E^2\right)\right)+\boldsymbol{\nabla}\left(u_E^2\right)\cdot(\mathbf{b}\times\boldsymbol{\nabla}B)\Big\}.\end{aligned} \tag{3.98}$$

It is possible to show that each set of brackets in equation 3.98 is equal to 0, thus confirming that ϵ in an unperturbed system is expected to remain constant.

$$\left.\frac{\mathrm{d}\epsilon}{\mathrm{d}t}\right|_0 = 0 \tag{3.99}$$

It is also possible to show the same for the toroidal canonical momentum, equation 2.73, by again taking the derivative with respect to time for an unperturbed system.

$$\left.\frac{\mathrm{d}\psi_c}{\mathrm{d}t}\right|_0 = \boldsymbol{\nabla}\psi_c\cdot\left.\frac{\mathrm{d}\mathbf{R}}{\mathrm{d}t}\right|_0 + \frac{\partial\psi_c}{\partial v_\parallel}\left.\frac{\mathrm{d}v_\parallel}{\mathrm{d}t}\right|_0 \tag{3.100}$$

where

$$\frac{\partial\psi_c}{\partial v_\parallel} = \frac{m}{q}\frac{F}{B} \tag{3.101}$$

$$\boldsymbol{\nabla}\psi_c = \left(1+\frac{mF'v_\parallel}{qB}\right)\boldsymbol{\nabla}\psi - \frac{mFv_\parallel}{qB^2}\boldsymbol{\nabla}B + \frac{m}{q}\boldsymbol{\nabla}u_\zeta. \tag{3.102}$$

Substitution into equation 3.100 leads to

$$\begin{aligned}\left.\frac{\mathrm{d}\psi_c}{\mathrm{d}t}\right|_0 = &\frac{mF}{qB}\left.\frac{\mathrm{d}v_\parallel}{\mathrm{d}t}\right|_0 + \left(1+\frac{mF'v_\parallel}{qB}\right)\boldsymbol{\nabla}\psi\cdot\left.\frac{\mathrm{d}\mathbf{R}}{\mathrm{d}t}\right|_0\\ &-\frac{mFv_\parallel}{qB^2}\boldsymbol{\nabla}B\cdot\left.\frac{\mathrm{d}\mathbf{R}}{\mathrm{d}t}\right|_0 + \frac{m}{q}\boldsymbol{\nabla}u_\zeta\cdot\left.\frac{\mathrm{d}\mathbf{R}}{\mathrm{d}t}\right|_0.\end{aligned} \tag{3.103}$$

Similarly to $\mathrm{d}\epsilon/\mathrm{d}t|_0$, it is found that expansion of equation 3.103 will results in all terms cancelling, thus leading to

$$\left.\frac{\mathrm{d}\psi_c}{\mathrm{d}t}\right|_0 = 0. \tag{3.104}$$

We can therefore test the accuracy of the newly implemented terms by checking the conservation of these quantities in an unperturbed simulation.

3.15.2 Testing

For the purposes of testing conservation in ORB5, a series of un-phyically large rotation profiles were used. By defining $\mathbf{u}_E$ independently of the background electric potential, the new terms introduced to the equations of motion were checked. This included introducing extremely large $E \times B$ drifts in the s, θ_* and ζ directions separately to ensure that each component behaved as expected. These simulations were useful to look for obvious errors, but did not allow comparison to the conservation of quantities in the weak-flow limit.

Therefore, a further set of simulations were performed. Although these were performed using parameters that gave a higher B_p/B than would be expected in actual experimental studies, the simulations had parameters much closer to existing tokamaks than the "extreme" conditions used before. A major radius of $R_0 = 0.85m$

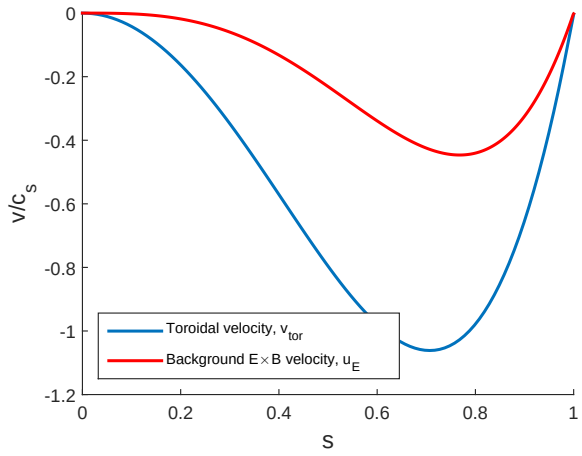

Figure 3.12: The toroidal velocity and background $E \times B$ velocity used for testing of the conservation of ψ_c and ϵ.

and minor radius $a = 0.425m$ were used, giving an aspect ratio $a/R = 0.5$. The safety profile is given by

$$\bar{q}(\rho) = 0.854 + 0.446\rho^2 \tag{3.105}$$

with a time-step size of $\mathrm{d}t = 10\Omega_{ci}^{-1}$. As these are linear simulations that are intended to study the conservation for individual markers, the total number of markers in the simulation was irrelevant and therefore kept low. Rotation profile 1, seen in section 3.8.1, was used; the resulting velocity profile can be seen in figure 3.12.

Variations of ψ_c and ϵ is expected to remain consistent across each marker. Figures 3.13 and 3.14 show the change of ψ_c and ϵ for a single selected marker in a region of high flow. Comparing results from strong and weak-flow limits it

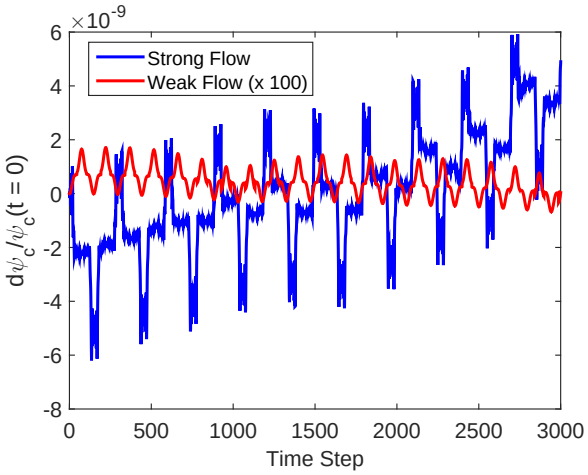

Figure 3.13: Variation of the toroidal canonical momentum with time from its initial value at t=0. The weak-flow variation has been multiplied by 100 in this figure.

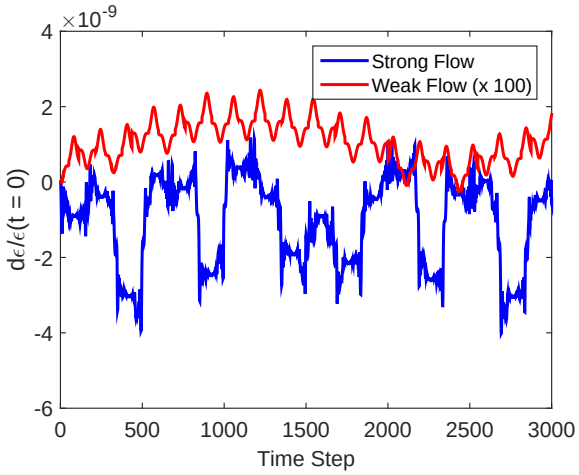

Figure 3.14: Variation of the particle energy with time from its initial value at t=0. The weak-flow variation has been multiplied by 100 in this figure.

is clear that the conservation of the canonical momentum and energy was superior before strong-flow terms were introduced. However, the variations were still of order $1 \times 10^{-7}\%$ for both ϵ and ψ_c. Therefore, although larger errors have been introduced, the relative changes of ψ_c and ϵ are expected to be too small to cause noticeable differences across most simulations.

It is also important to note that although ψ_c appears to be tending towards a higher value over time, longer simulations have found that this is related to a slow sinusoidal-like variation and its average value remains zero over long time-scales.

3.16 Summary

In this chapter, we have introduced many of the important elements of ORB5. We have also discussed how various quantities are stored, calculated and used to evolve the markers in a simulation.

More in depth discussion of the equilibrium state and the definition of equilibrium distribution function used in ORB5 has been given because of the modifications that were made to allow for strongly rotating plasmas. It was shown with a local limit expansion of the distribution function, that the effects of a centrifugal force from the toroidal rotation are reflected in the equilibria and give rise to a modified equilibrium density. This modification takes the form of a build up in density on the outboard side. As we desire equilibria close to the input profiles, a density correction term was found and added to the equilibrium distribution function of ORB5. This correction changes the flux-surface average density to one closer to the input profile while maintaining the poloidal variation of the density.

The implementation of the Vlasov equation, the equations of motion and Poisson equation are then described for the strong-flow version of ORB5. Finally a series of tests are performed to confirm that ORB5 is still working as intended. Several simulations were run which checked that the conservation of toroidal canonical momentum and gyrokinetic Hamiltonian was maintained with the inclusion of the strong flow terms. It was found that these new terms had a larger error but they were still within an acceptable threshold.

Chapter 4

Geodesic Acoustic Modes

4.1 Introduction and Background

The Geodesic Acoustic Mode (GAM) was first postulated in a paper published by Winsor [68], and has since been found experimentally in both helical systems and tokamaks[69]. The GAM is an n=m=0 potential perturbation, which is a consequence of poloidal zonal flows that causes an m=1 density oscillation between the top and bottom of the tokamak. The electric field of the zonal flow ($\mathbf{E}_r = -\boldsymbol{\nabla}\Phi$) is expected to remain constant on a flux surface but the flow, $\mathbf{v}_E = \mathbf{E}_r \times \mathbf{B}/B^2$, differs on the outboard (low field) side and the inboard (high field) side. Additionally, the smaller volume for the fluid to flow through on the inboard side contributes to a larger inboard poloidal flux. If the parallel ion flow along the field lines cannot compensate for this poloidal flow, an increasing density differential between the top and bottom of the tokamak develops.

This density differential subsequently creates a pressure build up at the top or bottom of the device. A restoring force is created by this poloidal pressure gradient which leads to the density oscillating at a frequency inversely proportional to the major radius and proportional to the sound speed.

The original derivation by Winsor begins with an ideal MHD model, neglecting time variations in $\mathbf{B}$, for which the perturbations obey

$$\rho \frac{\partial \tilde{\mathbf{v}}}{\partial t} = \tilde{\mathbf{J}} \times \mathbf{B} - \boldsymbol{\nabla}\tilde{p} \tag{4.1}$$

$$\frac{\partial \tilde{\rho}}{\partial t} + \boldsymbol{\nabla} \cdot \rho\tilde{\mathbf{v}} = 0 \tag{4.2}$$

$$\boldsymbol{\nabla}\tilde{\phi} = \tilde{\mathbf{v}} \times \mathbf{B} \tag{4.3}$$

$$\boldsymbol{\nabla} \cdot \tilde{\mathbf{J}} = 0 \tag{4.4}$$

$$\rho^{-\Gamma} \frac{\partial \tilde{p}}{\partial t} - \Gamma p \rho^{-\Gamma-1} \frac{\partial \tilde{\rho}}{\partial t} + \tilde{\mathbf{v}} \cdot \boldsymbol{\nabla} \left(p \rho^{-\Gamma} \right) = 0 \tag{4.5}$$

A tilde has been used here to denote perturbed quantities, which include a perturbed potential $\tilde{\phi}$, pressure $\tilde{p}$, velocity $\tilde{\mathbf{v}}$, current density $\tilde{\mathbf{J}}$ and charge density $\tilde{\rho}$. A plane wave solution is assumed for all perturbed quantities. In equation 4.5, Γ is the adiabatic index. All terms without a tilde represent equilibria quantities.

It is possible to break the perturbed velocity, $\tilde{\mathbf{v}}$, down into components perpendicular to the flux surface $\tilde{v}_\psi$, parallel to the magnetic field $\tilde{v}_B$, and a final component which is perpendicular to both other components and lies within the flux surface $\tilde{v}_s$.

$$\tilde{\mathbf{v}} = \left(\tilde{v}_\psi \frac{\boldsymbol{\nabla}\psi}{|\nabla\psi|^2} + \tilde{v}_s \frac{\mathbf{B} \times \boldsymbol{\nabla}\psi}{B^2} + \tilde{v}_B \frac{\mathbf{B}}{B} \right) \exp\left(-i\omega t\right) \tag{4.6}$$

Assuming an ideal case, the components of equation 4.3 parallel to $\mathbf{B}$ suggest the perturbed electrostatic potential is a function of ψ only. By looking at the component of equation 4.3 along $\boldsymbol{\nabla}\psi$, we can conclude that $\tilde{v}_s = \mathrm{d}\tilde{\phi}/\mathrm{d}\psi$ and $\tilde{v}_\psi = 0$. We now know the third term of equation 4.5 to be zero, and thus the equation reduces to

$$\tilde{p} = \left(\frac{\Gamma p}{\rho} \right) \tilde{\rho}. \tag{4.7}$$

Solving for $\tilde{\mathbf{J}}$, the divergence theorem converts the volume integral of equation 4.4 into a surface integral

$$\int \tilde{J}_\psi \mathcal{J} \mathrm{d}S = 0 \tag{4.8}$$

where $\mathcal{J}$ is the Jacobian. Using $\tilde{J}_\psi$, found from equation 4.1 by taking the component in the $\mathbf{B} \times \boldsymbol{\nabla}\psi$ direction, we can determine

$$\tilde{v}_s = -\frac{i\Gamma p}{\omega \rho^2} \int \frac{\mathbf{B} \times \boldsymbol{\nabla}\psi \cdot \boldsymbol{\nabla}\tilde{\rho}}{B^2} \mathcal{J} \mathrm{d}S \Big/ \int \frac{|\nabla\psi|^2}{B^2} \mathcal{J} \mathrm{d}S \tag{4.9}$$

and similarly, by looking in the direction parallel to the magnetic field

$$\tilde{v}_B = -\frac{i\Gamma p}{\omega \rho^2} \mathbf{B} \cdot \boldsymbol{\nabla}\tilde{\rho}. \tag{4.10}$$

By expanding equation 4.2 and multiplying by $\tilde{\rho}^* \mathcal{J} \mathrm{d}S$, we find equation 4.11.

$$\frac{\partial \tilde{\rho}}{\partial t} \tilde{\rho}^* \mathcal{J} \mathrm{d}S = \left(-\boldsymbol{\nabla}\rho \cdot \tilde{\mathbf{v}} - \rho \boldsymbol{\nabla} \cdot \tilde{\mathbf{v}} \right) \tilde{\rho}^* \mathcal{J} \mathrm{d}S \tag{4.11}$$

The $\boldsymbol{\nabla}\rho \cdot \tilde{\mathbf{v}}$ term on the right hand side is equal to zero, as the perturbed velocity lies within the flux surface and $\rho = \rho(\psi)$.

Substituting the non-zero velocity components into equation 4.11, it becomes

$$\begin{aligned}\frac{\partial \tilde{\rho}}{\partial t}\tilde{\rho}^* \mathcal{J}\mathrm{d}S = &-\rho\boldsymbol{\nabla}\cdot\left[\left(-\frac{i\Gamma p}{\omega\rho^2}\int \frac{\mathbf{B}\times\boldsymbol{\nabla}\psi\cdot\boldsymbol{\nabla}\tilde{\rho}}{B^2}\mathcal{J}\mathrm{d}S\Big/\int\frac{|\nabla\psi|^2}{B^2}\mathcal{J}\mathrm{d}S\right)\frac{\mathbf{B}\times\boldsymbol{\nabla}\psi}{B^2}\right.\\ &\left.-\frac{i\Gamma p}{\omega\rho^2}\mathbf{B}\cdot\boldsymbol{\nabla}\tilde{\rho}\frac{\mathbf{B}}{B}\right]\tilde{\rho}^*\exp\left(-i\omega t\right)\mathcal{J}\mathrm{d}S.\end{aligned} \tag{4.12}$$

If this is integrated by parts with respect to time, the divergence operators are expanded and we assume steady state conditions, then the time integral of the perturbed density will average to 0. The equation becomes

$$\begin{aligned}\omega^2\int|\tilde{\rho}|^2\mathcal{J}\mathrm{d}S = &\frac{\Gamma p}{\rho}\left(\int\tilde{\rho}\frac{\mathbf{B}\times\boldsymbol{\nabla}\psi\cdot\boldsymbol{\nabla}B^2}{B^4}\mathcal{J}\mathrm{d}S\Big/\int\frac{|\nabla\psi|^2}{B^2}\mathcal{J}\mathrm{d}S\right.\\ &\left.+\int\frac{|\mathbf{B}\boldsymbol{\nabla}\rho|^2}{B^2}\mathcal{J}\mathrm{d}S\right)\end{aligned} \tag{4.13}$$

where the second term of this wave equation is the ion acoustic mode and the first term, which is dependent on the curvature of $\mathbf{B}$ in the $\mathbf{B}\times\boldsymbol{\nabla}\psi$ surface, is known as the Geodesic Acoustic Mode.

The solution is dependent upon the geometry of the flux surfaces, but in the simplest case of circular concentric flux surfaces and large aspect ratio $r \ll R_0$, the dispersion relation for the GAM is given by

$$\omega_G^2 = \frac{2c_s^2}{R_0^2}\left(1+\frac{1}{2q^2}\right) \tag{4.14}$$

with sound speed $c_s = \sqrt{\Gamma p/\rho}$.

This original derivation that utilises a fluid MHD model is still one of the simplest methods to show the origins of the GAM, but there have also been derivation which use a kinetic model instead [70]. These kinetic models give a slightly different dispersion relation and it is therefore important that this is taken into account for simulations made with ORB5 which uses a gyrokinetic set of equations.

4.2 Benchmarking

As modifications have been made to ORB5, we first must ensure that it is still working as intended. This is important as the implementation of some common

features, such as the equilibrium distribution function, are now handled differently within ORB5 and errors could have effects on all simulations and not just cases with a toroidally rotating plasma.

In the first part of this chapter, the code was benchmarked against analytic predictions. Similar benchmarking has previously been performed in ORB5 by Biancalani [71].

4.2.1 Dispersion relation

The analytical prediction of dispersion relation used in this thesis for the non-rotating case was derived by Sugama and Watanabe [70].

$$\omega_{GAM} = \sqrt{\frac{7}{4} + \tau_e}\frac{v_{ti}}{R}\sqrt{1 + \frac{46 + 32\tau_e + 8\tau_e^2}{(7 + 4\tau_e)^2 q^2}} \tag{4.15}$$

Here, the ratio of electron to ion temperature $\tau_e = T_e/T_i$, $v_{Ti} = \sqrt{2T_i/m_i}$ is the ion thermal velocity and q is the safety factor. It is important to note that while the GAM frequency in ORB5 is expected to match with equation 4.15, the dispersion relation has been derived with the assumption of high q and as such simulations with low q may show deviations from predictions.

We have looked at the variation of GAM frequency with τ_e as well as the scaling with safety factor q. The GAM frequency, ω_G, and damping rate, γ_G, can be calculated from the simulations by fitting a damped sinusoid to the perturbed electric field. These simulations use the Fourier filter to allow only $n = m = 0$ modes to develop.

Simulations used flat temperature and density profiles and nearly flat q profiles. For the sake of convenience, when the safety factor q is discussed here we refer to its value at mid-radius $\rho = 0.5$. This matches the profiles used in previous studies by Biancalani, which were originally chosen for the benchmarking of ORB5 against local analytical theory [71]. The ad-hoc magnetic equilibrium, with circular concentric flux surfaces has been used for these simulations with a large aspect ratio, $a/R_0 = 0.1$.

Typical simulations performed here have a time step size of $20\Omega_{ci}^{-1}$, and last between 1.7×10^5 and 1.9×10^5 Ω_{ci}^{-1}. The system size was set to $\rho_* \equiv \rho_i/a = 1/160$ and 5 million ion markers were used. Electrons within simulations were adiabatic. A field grid size of $N_s \times N_\theta \times N_\zeta = 64 \times 64 \times 32$ was used as this was found to be sufficient in earlier investigations [71]. In order to excite a GAM, a deuterium density perturbation of the form $\sin\left[k_r\left(r - r_{min}\right)/\left(r_{max} - r_{min}\right)\right]$, which is independent of

poloidal and toroidal angle but has a radial variation, is introduced and the system is evolved linearly. Here, $r_{min} = 0.2a$ and $r_{max} = a$ (which are the upper and lower radial boundaries of the simulation domain) and the radial wave number is chosen to be $k_r \rho_i = 0.02\sqrt{\tau_e}$.

Any GAMs observed are natural modes of the system modelled by the simulation, but are excited by the initial perturbation we apply.

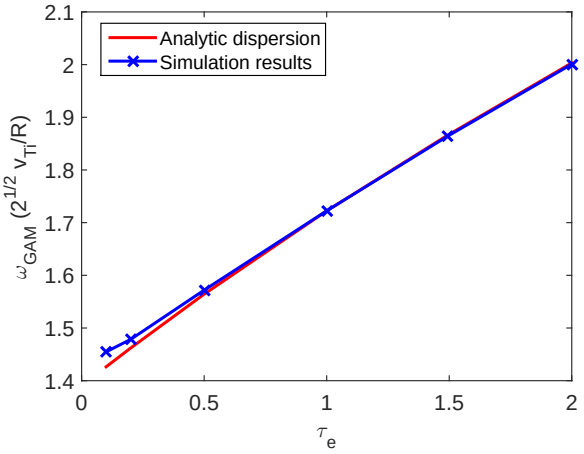

Figure 4.1: GAM frequency plotted as a function of τ_e. q remains at a constant value between simulations.

For the first tests, the safety factor was set to $q = 3$, while a scan across τ_e was performed. The results can be seen in figure 4.1, along with the predictions made by the analytical theory. Excellent agreement has been found between the analytical dispersion relation, equation 4.15, and the numeric results. Only at very low τ_e do the simulations begin to deviate from predicted values, but even then the variation is small.

The second benchmark of GAM frequency was a scan across safety factor q. In each run, the safety profile has been kept linear and nearly flat at an approximately set value, the electron to ion temperature ratio in these simulations was kept at $\tau_e = 1$. Figure 4.2 compares the analytical prediction from equation 4.15 with the frequency found from simulations. It can be seen that for higher values of q the predictions match closely, but as q tends towards zero the dispersion relation begins to lose accuracy; however, equation 4.15 was derived assuming high q and so this behaviour is not surprising. This also matches observations made by Biancalani and thus we can be reasonably confident that ORB5 is still operating as expected for the non-rotating cases.

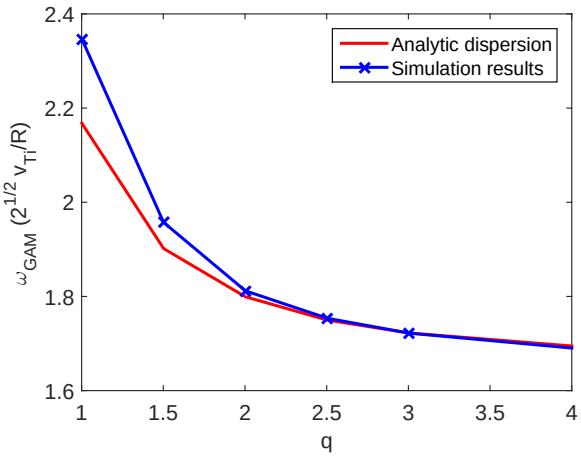

Figure 4.2: GAM frequency plotted as a function of q. τ_e remains constant between simulations.

4.2.2 Damping Rate

Numerous attempts have been made to derive an equation which describes the damping rate of GAMs in a tokamak, but the relation used here in equation 4.17 is taken from a paper by Sugama and Watanabe [72], which is in turn a correction of the earlier article which derives equation 4.15 [70].

$$\hat{\omega}_G = q\sqrt{\frac{7}{4}+\tau_e}\sqrt{1+\frac{46+32\tau_e+8\tau_e^2}{(7+4\tau_e)^2\,q^2}} \tag{4.16}$$

$$\begin{aligned}\gamma_{GAM} = &-\frac{\sqrt{\pi}}{2}q\frac{v_{Ti}}{R_0}\left[1+\frac{46/4+8\tau_e+2\tau_e^2}{q^2(\frac{7}{2}+2\tau_e)^2}\right]^{-1}\left[\exp(-\hat{\omega}_G^2)\left\{\hat{\omega}_G^4+(1+2\tau_e)\hat{\omega}_G^2\right\}\right.\\ &\left.+\frac{1}{4}\left(\frac{k_r v_{Ti} q}{\Omega_i}\right)^2\exp(-\hat{\omega}_G^2/4)\left\{\frac{\hat{\omega}_G^6}{128}+\frac{1+\tau_e}{16}\hat{\omega}_G^4+\left(\frac{3}{8}+\frac{7}{16}\tau_e+\frac{5}{32}\tau_e^2\right)\hat{\omega}_G^2\right\}\right]\end{aligned} \tag{4.17}$$

The k_r term in equation 4.17 relates to the finite orbit width effect on the damping and becomes particularly significant as q grows above ~ 1.5.

Using the same simulations that were performed in section 4.2.1 we can also study the damping rate dependence. The damping rate of the varying q simulations have been plotted in figure 4.3. It can be seen in figure 4.3 that the damping rate prediction is reasonably accurate for lower q (less than ~ 1.5), but as the finite orbit width effect becomes more significant at larger q, predictions from equation 4.17 deviate from the simulations. There is a weak relation between the behaviour of damping rate in simulation and prediction at these values, but equation 4.17

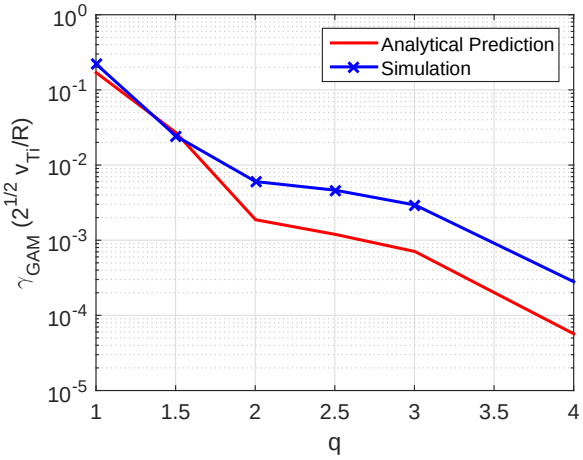

Figure 4.3: Simulation results for the change in damping rate of the GAMs with the variation of the safety factor q.

underestimates the damping rates by nearly an order of magnitude.

The variation of the damping rate with τ_e has not been plotted here. This is because we can conclude from figure 4.3 that simulations with $q \sim 3$ (as was used in the τ_e scan) would not be expected to match analytical predictions for any value of τ_e.

These observations on the behaviour of damping rate seem to match earlier observations made by Biancalani [71], but it is clear that the damping rate of a gyrokinetic code is difficult to accurately predict, in large part because of the finite orbit width effect (which would not effect fluid based simulations).

4.3 Radial eigenmodes

4.3.1 Introduction

The dispersion relation given in equation 4.15 finds the local GAM frequency for cases with radial wavenumber $k_r\rho_i = 0$. However, in reality, plasma waves may be excited with a non-zero k_r and therefore, there are a variety of GAM frequencies possible at each radius. Additionally, the derivation of the dispersion relation given in equation 4.15 only considers that particles move along a flux surface, but radial motion of particles arises from gyro-motion and trapped particle banana orbits. This leads to a modification of wave frequency as the wavelength becomes comparable to the gyro-scale or the banana orbits. As tokamaks have parameters which vary radially, a local derivation will not give a sufficient description of plasma motion in

a global simulation.

As the temperature in a tokamak changes radially, it would be expected that the frequency, ω_G, of the GAM would also change with radius. However, experiments have shown that GAMs are found with a common frequency over a substantial radial width [73, 74]. This implies that GAMs appears in tokamaks as an eigenmode.

An article by Itoh has been published which discusses Geodesic acoustic eigenmodes and derives an equation for the perturbed potential, corresponding to oscillations in the presence of a temperature gradient [75]. Local oscillations on different magnetic surfaces will interfere with each other due to the finite ion gyroradius, and give rise to the eigenmodes. It is also found that the oscillations propagate outwards if the temperature is decreasing towards the edge and the characteristic wavelength is found to scale as $\rho_i^{2/3} L_T^{1/3}$, where ρ_i is the ion gyroradius and L_T is the temperature gradient scale length. This derivation uses a modified form of the Wentzel-Kramers-Brillouin (WKB) approximation, a method of finding approximate solutions for linear differential equations which have spatially varying components, and should only be considered accurate for low k_r [76, 77].

The derivation begins by balancing the cross-field current $\tilde{J}_{D,r}$ (caused by the magnetic field curvature) and the ion polarization current $\tilde{J}_{\rho,r}$ in the presence of an electrostatic potential of form

$$\tilde{\phi} \exp(ik_r r - i\omega t)$$

in leading order [75]. Here, k_r is the radial wavelength of the potential perturbation. In order to make the analytic study of the radial eigenmode clear the derivation is performed in the collisionless limit; so that $T_e \gg T_i$ and $k_r \rho_i \ll 1$.

In this limit, the relation $v_{th,i}/R \ll \omega$ holds for $\omega \sim \omega_G$ and $\tilde{J}_{D,r}$ is not significantly effected by the finite gyro-radius effect, as it is dominated by the electron response. However, the ion polarization current $\tilde{J}_{\rho,r}$, which is in proportion to ω, is screened due to the finite gyro-radius effect by a factor of $(1 - k_r^2 \rho_i^2)$. The relation $\tilde{J}_{\rho,r} + \tilde{J}_{D,r} = 0$ therefore leads to

$$\left(1 - k_r^2 \rho_i^2\right) \omega^2 = \omega_G^2 \tag{4.18}$$

where only the lowest order finite gyro-radius effect is included. Here, ω is the frequency of the perturbations and ω_G is the GAM frequency calculated for the case in which $k_r \rho_i = 0$.

When considering a temperature that decreases radially, we can select the radius r_0 for which the relation $\omega^2 = \omega_G^2(r_0)$ holds. Taking the radial gradient of

the temperature into account, we can give an estimate for the temperature profile centred around r_0 with

$$T(r) = T(r_0)\left[1 - \frac{r - r_0}{L_T}\right] \tag{4.19}$$

which in turn leads to an estimated radially dependent dispersion relation

$$\omega_G^2(r) = \omega_G^2(r_0)\left[1 - \frac{r - r_0}{L_T}\right]. \tag{4.20}$$

By combining equations 4.18 and 4.20, the dispersion relation can be rewritten as an eigenmode equation

$$\rho_i^2 \frac{\mathrm{d}^2}{\mathrm{d}r^2}\phi(r) + \frac{r - r_0}{L_T}\phi(r) = 0, \tag{4.21}$$

using the replacement of $\rho_i^2 k_r^2 \rightarrow -\rho_i^2 \mathrm{d}^2/\mathrm{d}r^2$. Equation 4.21 has a characteristic length scale $\lambda = \rho_i^{2/3} L_T^{1/3}$ and can be normalized to

$$\frac{\mathrm{d}^2}{\mathrm{d}x^2}\phi(x) + x\phi(x) = 0 \tag{4.22}$$

where $x = (r - r_0)\lambda^{-1}$. Equation 4.22 can be readily solved with an Airy function

$$\phi(x) = \mathrm{Ai}(-x). \tag{4.23}$$

This solution will peak near the point at which $r = r_0$ and will propagate in the lower temperature region ($r > r_0$). Equation 4.23 describes the form a perturbed potential representing a radial eigenmode will take, if our simulations contain radial eigenmodes then similarly shaped potentials would be expected.

Simulation Parameters

The initial density perturbation used to excite the modes in these simulations is given by

$$\delta f = \delta f_0 \sin\left(k_r\left[\frac{r - r_{min}}{r_{max} - r_{min}}\right]\right) \tag{4.24}$$

where δf_0 is the size of the perturbation at the initial time-step and $r_{min} = 0$ and $r_{max} = a$ are input parameters denoting the radial domain size.

The simulations in this section were performed with circular concentric flux surfaces, and $\mathrm{d}\ln A/\mathrm{d}t$ of temperature and density had a constant value across a substantial radial width, as shown in section 3.9.2. For this simulation, $T_e/T_i = 5.0$, $a/L_T = 2.5$, $a/L_n = 0.807$, $\Delta\rho = 0.5a$, $\Delta_T = \Delta_n = 0.04a$ and $\rho_{peak} = 0.5$. The

aspect ratio of the simulation is $a/R = 0.1$ and a pseudo-safety profile of

$$\bar{q}(\rho) = 3.5 + \rho^2, \tag{4.25}$$

was used. The ratio between the nominal Larmor radius ρ_s and the minor radius a is taken as $\rho^* = \rho_s/a = 1/160$. An adiabatic electron response is also assumed. These parameters have been chosen to ensure a substantial density gradient and also to keep the simulation in the collisionless limit.

The simulations had 100 million (100M) markers with a time step size of $20\Omega_{ci}^{-1}$. Each simulation was run for approximately $8 \times 10^4 \Omega_{ci}^{-1}$. The resolution of the field grid was $N_s \times N_\theta \times N_\zeta = 128 \times 32 \times 32$ and the Fourier filter was set to only allow modes of $n = 0$ and m between -4 and 4 to develop. This field grid has a high resolution in the s-direction but lower resolution in the θ and ζ directions because we would expect fluctuations in the field to largely be in the radial direction if produced by GAMs.

Simulation Analysis

In a real system it would not be expected for only a single eigenfunction to develop, and in fact previously published results have identified several bands of frequency with a finite radial width appearing simultaneously [73, 74]. Therefore, we would expect the perturbed electrostatic potential of simulations in ORB5 to be a superposition of numerous modes. We assume that under the chosen conditions, the GAMs will be the dominant modes excited in these simulations.

We consider the flux-surface averaged perturbed electric potential ϕ; a function of radius and time. By taking the derivative of ϕ with respect to radius, $\mathrm{d}\phi/\mathrm{d}\rho$, some of the irrelevant fluctuations that are present in ϕ can be reduced. A singular value decomposition (SVD) is taken of this derivative, which lets us separate and identify the individual modes which compose the perturbed potential [78]. The SVD decomposes a matrix A:

$$A = U\Sigma V^* \tag{4.26}$$

where, in our analysis, $A = \frac{\mathrm{d}\phi(s,t)}{\mathrm{d}\rho}$. Σ is a diagonal matrix of non-negative numbers containing the singular values that can represent the relative sizes of each mode. If $\phi(\rho, t)$ is a matrix of dimensions m in the radial direction measured at n points in time, Σ is an $m \times n$ matrix. U is an $m \times m$ unitary matrix, the columns of which contain the eigenfunctions of each mode. Similarly, V is an $n \times n$ unitary matrix which has columns describing the variation of each eigenmode with time. In the case that $m > n$, then a full SVD will have $(m - n)$ 'extra' columns in U that are

not required to reconstruct A. The advantage of an SVD method is that it does not require A to be a square matrix.

The frequency and damping rate of each identified mode may be found by fitting a damped sinusoid to each modes individual time series $V_i(t)$, where i is an index labelling each mode and V_i is the i^{th} column of V. For analysis in section 4.3.2, only the frequency and damping rate of the most prominent mode ($i = 1$) has been plotted.

4.3.2 k_r dependence

Equation 4.23 was derived using an assumed dispersion relation, equation 4.18. Before we test predictions of the eigenfunctions, we perform simulations to investigate the accuracy of the dispersion relation which the predictions rely upon.

The k_r dependence was tested with a scan which uses a density perturbation of varying radial wavenumber to excite the GAMs inherent to the system. When decomposing $\mathrm{d}\phi/\mathrm{d}\rho$ with the SVD, the mode with the highest singular value was selected and analysed in each simulation. During the fitting to find the frequency and damping rate, the early time-steps were ignored to allow for relaxation of the initial perturbation.

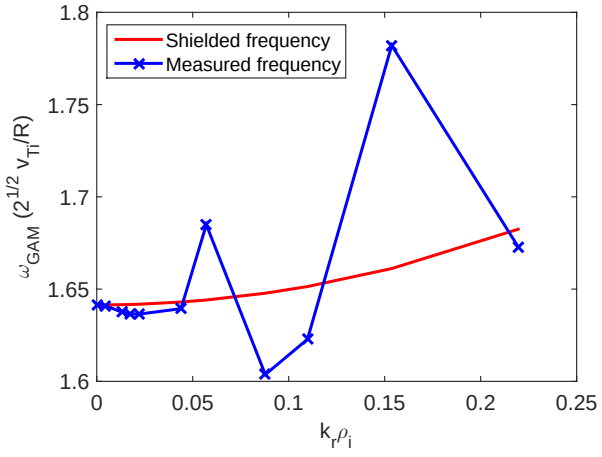

Figure 4.4: GAM frequency plotted as a function of $k_r\rho_i$.

It can be seen by looking at figure 4.4 that the dependence on k_r is not particularly reliable; although it should be noted that at least some of this result can be attributed to a poor fitting when calculating GAM frequency. The GAM frequency does stay largely constant for simulations with very small radial wavenumber, but varies substantially above $k_r\rho_i = 0.05$. This erratic behaviour can also be seen with

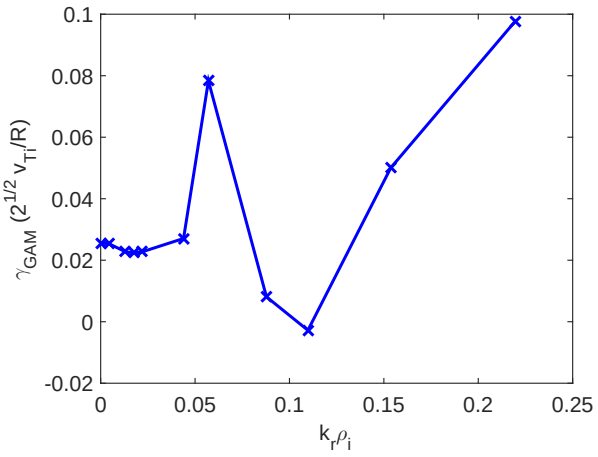

Figure 4.5: GAM damping rate plotted as a function of $k_r\rho_i$.

the damping rate, figure 4.5.

The 'shielded frequency' shows the variation predicted by equation 4.18. For the plotting of the shielded frequency, the GAM frequency observed for the lowest $k_r\rho_i$ perturbation has been used in place of ω_G. A full analytical prediction, using equation 4.15 to calculate ω_G has not been plotted due to the low reliability of this dispersion relation at high τ_e.

Data has only been plotted for simulations with $k_r\rho_i$ up to ~ 0.23 as the Singular Value Decomposition did not seem to recover individual modes from higher k_r runs.

It was decided that for $k_r\rho_i < 0.05$ the frequencies were close enough to expectations to continue the investigation of GAM eigenmodes. Due to the method of derivation, predictions were already expected to be valid only for low k_r. For radial wavenumbers higher than this cut-off, the eigenfunctions should not be expected to have a form similar to the Airy function.

4.3.3 Results

We now turn our interest to the GAM eigenfunctions found from the SVD. The dominant modes are plotted against ρ and compared to analytical predictions given by equation 4.23. The appropriate value of r_0 is not immediately apparent and must be found by observation. Furthermore, following the boundary condition described in section 3.12.4, we know that any eigenfunctions existing in simulations should have $\phi = 0$ at the last closed flux surface, $s = 1$. Therefore, any predicted eigenfunction of equation 4.23 must also be subject to the same restriction.

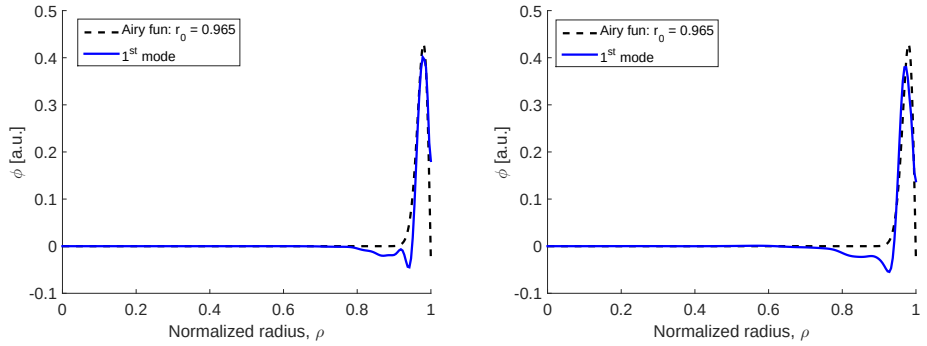

Figure 4.6: Potential of the most prominent eigenfunction and its predicted form in runs with $k_r\rho_i = 4.44 \times 10^{-3}$ and $k_r\rho_i = 5.71 \times 10^{-2}$ on the left and right respectively. Airy fit and simulation results have been resized so that they have matching amplitudes.

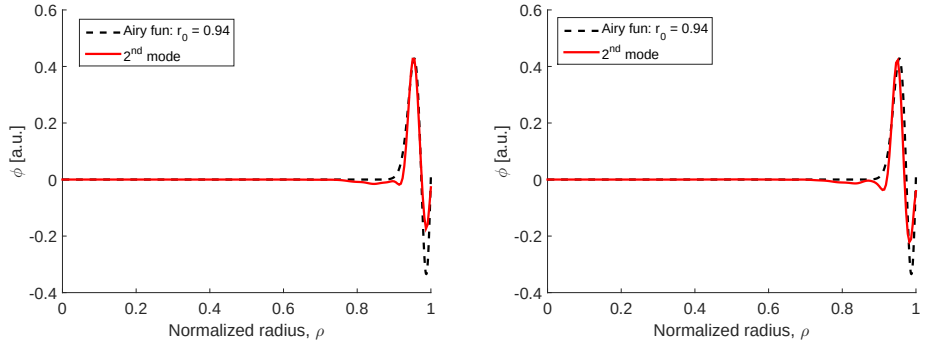

Figure 4.7: Potential of the second most prominent eigenfunction and its predicted form in runs with $k_r\rho_i = 4.44 \times 10^{-3}$ and $k_r\rho_i = 5.71 \times 10^{-2}$ on the left and right respectively. Airy fit and simulation results have been resized so that they have matching amplitudes.

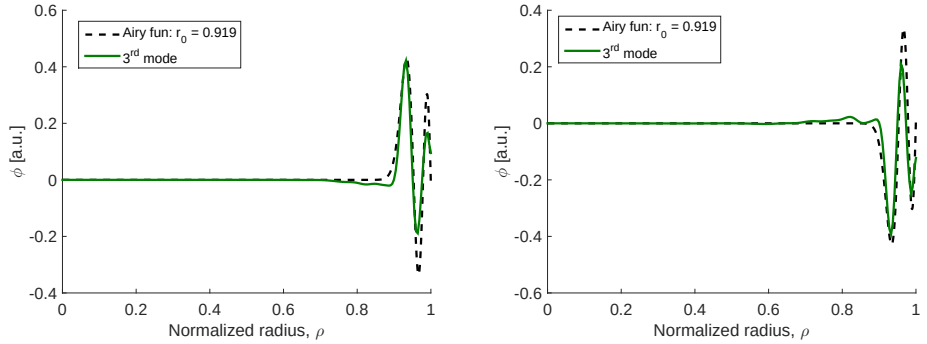

Figure 4.8: Potential of the third most prominent eigenfunction and its predicted form in runs with $k_r\rho_i = 4.44 \times 10^{-3}$ and $k_r\rho_i = 5.71 \times 10^{-2}$ on the left and right respectively. Airy fit and simulation results have been resized so that they have matching amplitudes.

Figures 4.6, 4.7 and 4.8 show the three most most prominent modes found in simulations. The same eigenmodes appear in each simulation, independent of the initial perturbation, which indicates that they are modes inherent to the system. However, it can also be seen that the analytical predictions deviate from observations as k_r increases.

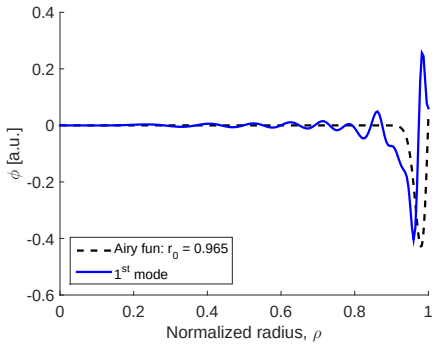

Figure 4.9: Potential of the most prominent eigenfunction in a run with $k_r\rho_i = 0.1537$ and its predicted form. Airy fit and simulation results have been resized so that they have matching amplitudes.

The higher the spatial frequency of the initial perturbation to the system, the more the modes of the simulations move away from the expected Airy function. By $k_r\rho_i = 0.1537$, figure 4.9, the Airy solution is seen to provide a much weaker match. This could be due to the SVD not successfully isolating single modes, but it is also possible that for simulations with larger $k_r\rho_i$, the GAM eigenmodes are no longer dominant and other modes are becoming more significant.

Despite the poor predictions for waves with large k_r, there are clear eigenmodes present in many of the simulations performed. For low k_r, we can conclude that radial GAM eigenmodes are observed in simulations which match the predictions made by Itoh [75].

4.4 Rotating plasma

4.4.1 Introduction

In addition to investigations of GAM eigenmodes, research has also been undertaken to investigate the behaviour of GAMs under a toroidal rotation. There have been many previous studies predicting the behaviour of Geodesic Acoustic modes and zonal flows using both kinetic and fluid approaches [79, 80, 81, 82, 83, 84, 85].

A dispersion relation has been derived by Wahlberg for GAMs in the presence

of a toroidal rotation by solving the Frieman-Rotenberg eigenvalue equation [84]. This derivation also finds that a second low frequency GAM will form in the presence of rotation, but this has not been a point of focus in this thesis. The derived GAM dispersion relation is given as

$$\begin{aligned}\omega_G^2 =&\omega_s^2\Bigg[1+\frac{1}{2q^2}+\frac{\mathcal{M}^2\left(\mathcal{M}^2+4\right)}{\Gamma}\\&+\sqrt{\left(1+\frac{1}{2q^2}+\frac{\mathcal{M}^2\left(\mathcal{M}^2+4\right)}{\Gamma}\right)^2-\frac{2\mathcal{M}^4}{q^2\Gamma}\left(1-\frac{1}{\Gamma}\right)}\Bigg]\end{aligned} \tag{4.27}$$

where

$$\omega_s^2=\frac{\Gamma T_i}{R_0^2} \tag{4.28}$$

is the sound frequency. The adiabatic index Γ is taken to be

$$\Gamma=\left(\frac{7}{4}+\tau_e\right)$$

as used by Sugama and Watanabe in their derivation of a dispersion relation using a kinetic approach, equation 4.15 [70]. This change in GAM frequency, shown by equation 4.27, is caused by the centrifugal effects of a rotating plasma.

The toroidal mach number of the plasma is given by

$$\mathcal{M}=\sqrt{\frac{\Omega_t^2R_0^2}{2T}}\sim\mathcal{O}(1) \tag{4.29}$$

where Ω_t is the toroidal rotation rate of the plasma. This is the same as the toroidal velocity normalized with the thermal velocity.

The dispersion relation given in equation 4.27 has been derived assuming circular concentric flux surfaces in a large aspect ratio device, as such this relation would not be valid in simulations with MAST-like parameters. ω_G is only ever dependant on $\mathcal{M}^2$ and never $\mathcal{M}$, this suggests that the direction of toroidal rotation will have no effect on the change in GAM frequency.

Here, investigations have used flat temperature and density profiles with a system size $\rho_*=1/160$. Other parameters of the simulations were $\tau_e=1$, $R_0=1.3$, $a=0.13$, 10 million $(10M)$ ion markers and an approximately flat q profile with value $q\sim 2$. The field grid size was $N_s\times N_\theta\times N_\zeta=128\times32\times32$ with time steps of $10\Omega_{ci}^{-1}$. Only modes with $n=0$ and $m=-4$ to 4 were allowed to develop. A solid body rotation of varying size was applied to these simulations. Finally, an initial perturbation matching that shown in equation 4.24 with $k_r\rho_i=6.25\times10^{-4}\pi$ was

used.

4.4.2 Results

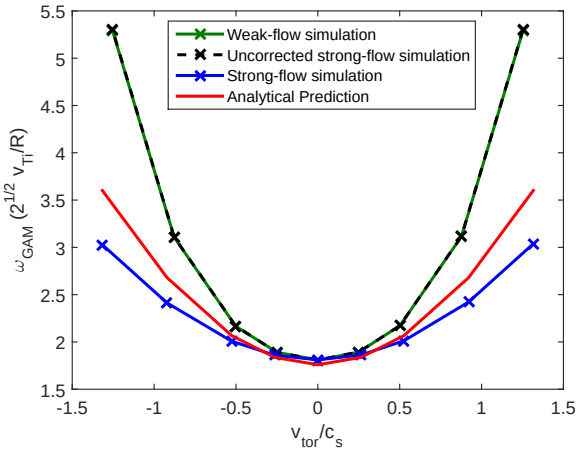

Figure 4.10: GAM frequency as a function of toroidal velocity.

As can be seen in figure 4.10, the direction of toroidal rotation of the plasma has negligible effect on the change in frequency. This is as predicted by equation 4.27 and discussed earlier. In addition to the results of simulations which use the strong-flow modifications, the figure also contains results which use the weak-flow formalism and results from simulations which use the strong-flow formalism but do not include the density correction term (this is labelled as the uncorrected strong-flow case in figures).

The frequency prediction for $v_{tor}/c_{si} = 0$ appears to have been accurate to within a good margin, which suggests that the adiabatic index selected is valid here. It can be seen that the analytical predictions do however overestimate the change in frequency that occurs with rotation rate in strong-flow simulations. This overestimation is not substantial at low toroidal velocity, but as the Mach number approaches unity the differences between prediction and simulation becomes more pronounced.

It is apparent from these results that the density correction term has a much more substantial impact on GAM frequency than the introduction of the strong-flow terms. This suggests that the ion density plays an important role in changes to GAM frequency. It also appears that the modifications made to ORB5 as part of this thesis bring the variation of GAM frequency closer to analytical predictions.

No predictions were made for the damping rate and it can be seen in figure

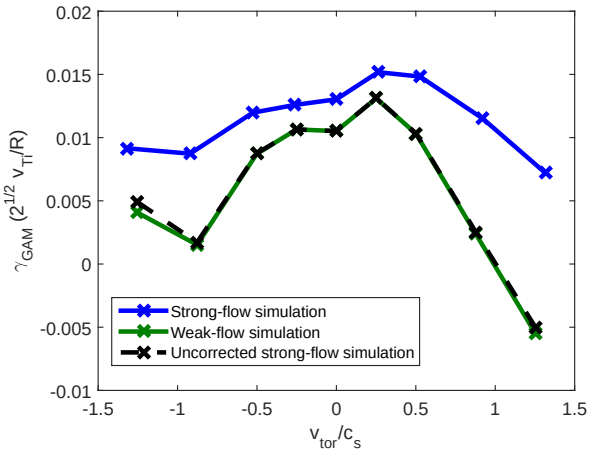

Figure 4.11: Damping rate of GAM as a function of toroidal velocity.

4.11 that there is a poor trend found in the results; although there may be a weak decrease in damping rate with larger rotation. However, as the damping is already small, any fluctuations of potential may lead to sizeable variations in the damping rate from our analysis. Observations from both weak and strong-flow simulations however do show a general trend of lowered GAM damping rate with increasing magnitude of toroidal velocity.

It was found in early benchmarking tests performed by Biancalani that measurement of damping rate in a simulation requires a much larger number of markers to achieve reasonable results in comparison to those required for recovering frequency [71]. Therefore, future investigations into the damping of GAMs with toroidal rotation will likely need many more markers in simulations to measure the damping rate with any real confidence.

4.5 Summary

In this chapter, Geodesic Acoustic Modes were introduced and a series of benchmarking tests were performed. Although these tests had been performed before [71], they were repeated here to ensure the introduction of strong-flow terms had not introduced errors into simulations. A good match was found between the dispersion relation and results, but the predictions of damping rate were found to not agree in situations for which the finite-orbit width became important.

Prompted by experimental observations of GAMs with the same frequency across a substantial radial width, simulations were performed to investigate the presence of GAMs as radial eigenmodes. Earlier work published by Itoh [75] was

used as a basis for these simulations. Despite finding poor predictions of GAM frequency dependence with radial wavenumber, eigenfunctions were observed which had a very close resemblance to those predicted by Itoh.

Finally, the effects of toroidal rotation on GAMs were investigated. Simulations found that the magnitude of the toroidal velocity was important, but direction had little impact. This was found to be in agreement with a dispersion relation derived by Wahlberg for GAMs in a rotating plasma [84].

Chapter 5

Linear simulations

5.1 Introduction

In addition to $n = 0$ modes, we are also interested in the behaviour of the toroidal modes with $n \neq 0$. For linear studies, it is possible to isolate and allow only one toroidal mode to develop in each simulation through the use of a surface-dependent filter. This is used to perform a scan over varying toroidal number n while keeping the other simulation parameters constant. It is required that each mode be investigated individually as the linear modes couple and will therefore affect each other if not isolated.

For these scans over a varying toroidal number, an average poloidal wavenumber can be calculated as

$$k_\theta \rho_i = \frac{n q_0}{r_{mid}} = \frac{2 n q_0}{a} \tag{5.1}$$

where $q_0 = q(\rho = 0.5)$ and $r_{mid} = 0.5a$. This has a relation to the toroidal wavenumber of

$$k_\zeta \rho_i = \frac{n}{R} = \frac{B_p}{B_t} k_\theta \rho_i. \tag{5.2}$$

Simulation Parameters

The linear simulations performed in this chapter have used a radial, electric field applied to a plasma with parameters matching the CYCLONE base case [86, 87] in an ad-hoc circular concentric equilibrium. The CYCLONE case is based off of the local parameters for an ITER-relevant Doublet III-D (DIII-D) high confinement shot (shot #81499) at radius, $r = 0.5a$ and time, $t = 4000ms$ [88]. This is a commonly used case for benchmarking gyrokinetic particle-in-cell codes and many CYCLONE case ORB5 simulations have previously been performed [89, 63, 19].

For the CYCLONE base case, the main parameters of the system are $B = 1.91T$, minor radius $a = 0.625m$, major radius $R_0 = 1.7m$ and normalised gyro-radius $\rho_* = 1/180$. In these liner simulations, peaked gradient profiles have been used (shown earlier as equilibrium profile 1 in section 3.9.1). This differs from the usual global CYCLONE profiles which have R/L_T and R/L_n with a nearly constant value across most of the radial domain. This use of peaked profiles is to ensure that the modes which form are well localised to the area of interest (the radius at which the profiles peak, $r = 0.5a$). Density and temperature gradient scale lengths are related by the ratio $\eta_i = L_n/L_T = 3.114$ in the CYCLONE case which leads to $R/L_T = 6.92$ and $R/L_n = 2.22$ with $\Delta_i = \Delta_e = 0.3$ and $\rho_{peak} = 0.5$. At mid-radius, the safety factor and magnetic shear are $q(0.5) = 1.4$ and $\hat{s} = \frac{r}{q}\frac{\mathrm{d}q}{\mathrm{d}r} = 0.8$ respectively. This is given by the safety factor profile

$$q(\rho) = 0.86 - 0.16\rho + 2.52\rho^2 \tag{5.3}$$

which is implemented within ORB5 as a pseudo-safety factor,

$$\bar{q}(\rho) = 0.854 + 2.184\rho^2. \tag{5.4}$$

The background electric field is such that it applies a uniform toroidal rotation to the system, as first described in section 3.8.2, although the small toroidal velocity present in even the 'non-rotating' case caused by the profile gradients will mean that this rotation rate is not in reality homogeneous. This choice of constant E_ψ should allow for the investigation of strong-flow terms in a global simulation of a rotating solid-body plasma. This would be expected to exhibit behaviour which can largely be attributed to the centrifugal and Coriolis forces in the plasma, as discussed later in section 5.3 of this thesis.

Additional parameters used in these simulations include time-steps of size 20 Ω_{ci}^{-1} and a field grid of size $N_s \times N_\theta \times N_\zeta = 128 \times 512 \times 256$. The resolution of the field grid has here been increased from previous investigations in chapter 4 because we are now investigating modes which we would expect to fluctuate in the poloidal and toroidal directions. Adiabatic electrons have been used for these simulations and the ratio of ion to electron temperature is given as $\tau = T_i/T_e = 1$. Simulations were run for $8 \times 10^4 \Omega_{ci}^{-1}$ and a GENE perturbation was used which applied an initial perturbation with $n_{min} = 2$ and $n_{max} = 90$.

Rotation Profiles

A solid body rotation rate applied to the linear simulations gives a constant flux-surface averaged toroidal velocity. The variously sized profiles used are shown in figure 5.1a. However, due to the equilibrium profile gradients, there is a non-zero toroidal velocity already present in the simulations even for the 'non-rotation' case. This leads to an equilibrium toroidal velocity that has a variation from the applied toroidal velocity. The reconstructed toroidal velocities for the linear simulations can be seen in figure 5.1b.

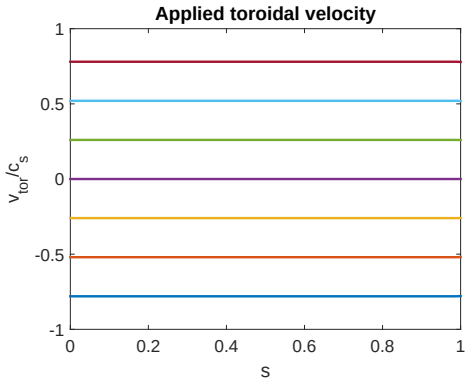

(a) A solid body toroidal rotation rate is applied, which gives a constant flux-surface averaged toroidal velocity.

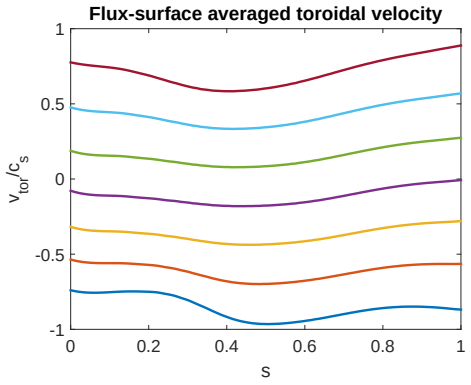

(b) The flux-surface averaged toroidal velocity reconstructed from the velocity profiles.

Figure 5.1: Flux-surface averaged toroidal velocity as a function of s.

As a result, there will be some toroidal velocity gradient within simulations which may have a stabilizing effect from the velocity shear. When toroidal velocities are discussed in this chapter, the applied toroidal velocity at mid-radius is implied.

The diamagnetic flows which are present in all simulations vary radially, peaking at approximately $s = 0.45$ with a value of $v_{tor}/c_s = -0.18$.

5.2 Convergence with marker number

In order to have confidence in the results found in any simulations, we must first be able to confirm that the simulations converge to a solution. This can be simply checked in the linear case by comparing the ratio of signal to noise, using the definitions given in section 3.13. Unlike the non-linear simulations, linear simulations do not require as rigorous noise control to remain physically relevant. Apart from the use of the field-aligned filter that was described in section 3.12.4, the noise can be kept to a reasonable level through an appropriate choice of the number of

markers. We desire as high a signal to noise ratio as possible but noise is known to scale with marker number as $N^{-1/2}$, where N is the number of markers. Due to the computational cost of global PIC simulations, a balance must therefore be made between the gains from adding markers and the computational resources required for the simulation.

By looking at the signal to noise ratio for a simulation containing a single mode, the convergence of linear simulations with marker number can be easily checked. The toroidal mode chosen for these tests has an average poloidal wavenumber of $k_\theta \rho_i = 0.316$, which was found to be the fastest growing mode in a non-rotating case. The model used in ORB5 will be more accurately represented with a higher number of markers, and therefore the simulations should converge on a single growth rate.

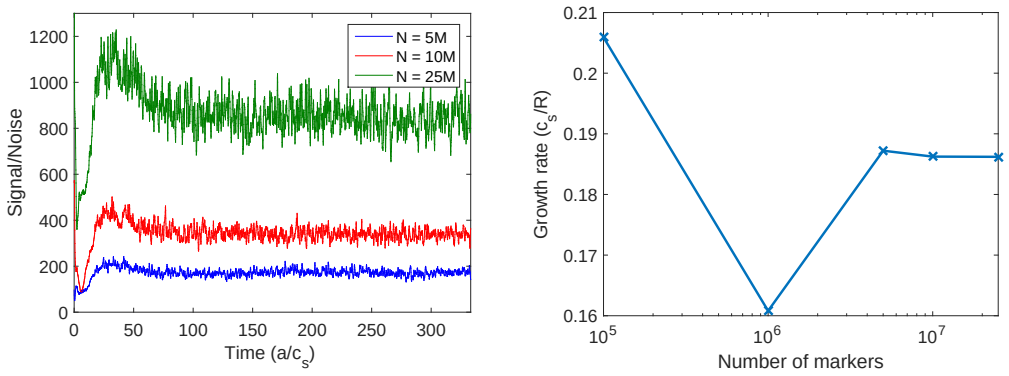

Figure 5.2: Signal to noise ratio for a non-rotating simulation containing a mode with $k_\theta \rho_i = 0.316$. The signal does not include the zonal-flows as it would dominate over the other modes.

Figure 5.2a shows the change of signal to noise ratio with time for simulations of varying marker number. It can be seen in the early stages of all simulations the signal to noise ratio is much lower than at later time steps. At initial time-steps the modes of interest are still small but they will grow exponentially, leading to the more stable S/N ratio seen at later times.

It can be seen from figure 5.2b, that the growth rate of the selected mode converges on a value as more markers are added to the simulations. Low marker numbers in particular give a large variation of growth rate, but given that the average signal to noise ratio for the lowest simulation was approximately $S/N \sim 4$ this is not at all surprising. An accurate representation of the gyrokinetic model used within ORB5 would not be expected for simulations with $S/N < 10$ [90].

In the case of these simulations, the signal to noise ratio was found to con-

sistently increases more than would be expected from the corresponding increase in marker number. It was found that a boost in S/N proportional to N instead of the expected $N^{1/2}$ occurred; however it would not be reasonable to assume a similar increase in all simulations.

Following these tests, a marker number of 10M was chosen for the CYCLONE case linear simulations. This achieves the desired balance between signal to noise ratio and computing cost. For 10M markers, each of the linear simulations used 512 cores for approximately 2 hours.

5.3 Rotational effects

To discuss the effects that a toroidal rotation may have on the modes and transport of simulations, it is convenient to consider the plasma in a co-moving frame (which rotates at the same rate as the plasma) instead of the laboratory frame. A series of papers published by Peeters have derived a set of gyrokinetic equations in a co-moving frame, while allowing for strong rotational effects, in the local limit [91, 34]. Subsequently, investigations have been performed for strongly rotating plasmas in local gyrokinetic code GKW [92, 35, 36].

In a frame which rotates with the plasma, the effects of a toroidal rotation can be characterised as inertial forces: the centrifugal and Coriolis forces.

The centrifugal force acts through a centrifugal drift. In addition to this, the centrifugal force will cause particles to lose an increased amount of parallel velocity as they move from the outboard to the inboard side of the tokamak. As a result, the centrifugal force enhances the trapping of particles and a poloidal density variation will also arise giving a larger density on the outboard side. For simulations with kinetic electrons, it would therefore be expected to see an enhancement to the trapped electron mode from the centrifugal force. As the centrifugal drift is dependent upon the plasma flow and not the particle velocity, its effect is the same across all particles of the same species.

The centrifugal force should have little contribution to the toroidal momentum transport outside of changes which arise from the density variation along the flux surfaces. Using a low-field side gyro-fluid model Peeters has found that the effects of the centrifugal drift can lead to a change in the frequency of each mode. This frequency change is positive and increases with rotation rate. It can be viewed as a Doppler shift resulting from the centrifugal effects [34].

The Coriolis force enters the gyrokinetic equations through the Coriolis drift, which acts in the same direction as the drifts caused by the magnetic inhomogeneity.

It will contribute no change to energy. With a gyro-fluid model in a co-moving frame Peeters has shown that the toroidal momentum flux in a rotating plasma will have a diffusive contribution and a Coriolis pinch term [91]. This toroidal momentum pinch acts to generate a radial gradient in the toroidal velocity profile, potentially leading to an increasing $E \times B$ shearing rate. The toroidal pinch velocity always acts to enhance the absolute value of the velocity gradient. It is also found that the pinch velocity will decrease with $k_\theta \rho_i$.

However, further studies have suggested that this inwards momentum flux is expected to be small with adiabatic electrons. Again, using a gyro-fluid model it was found that the parallel dynamics will act to compensate for the Coriolis pinch and lead to a zero parallel momentum flux [93, 94]. There will be some differences in a gyrokinetic model, meaning we may still observe some momentum flux, but we expect that the Coriolis pinch effect will not be the dominant mechanism.

We can show that the centrifugal and Coriolis drifts are approximately retained in the laboratory frame within the magnetic curvature drift. To do this, we consider the parallel velocity of a particle (in the lab frame), $v_\parallel$, to be composed of two parts: the parallel flow, v_0, and a particles parallel velocity relative to the flow, $u_\parallel = v_\parallel - v_0$. The parallel flow is the same flow given in equation 3.37.

In a standard simulation with no toroidal rotation (and neglecting any parallel flow that results from the profile gradients) the markers would only have a particle specific parallel velocity $u_\parallel$, and so this value is dependent on the individual markers. $u_\parallel$ could also be considered the markers parallel velocity in a frame moving with the same speed as the parallel flow. The parallel flow on the other hand is a radially dependent term.

By substituting

$$v_\parallel \rightarrow v_0 + u_\parallel$$

into the equation for the curvature drift, we get

$$\frac{mv_\parallel^2}{qB_\parallel^*}\frac{\mathbf{B}\times\boldsymbol{\nabla}B}{B^2} = \frac{mu_\parallel^2}{qB_\parallel^*}\frac{\mathbf{B}\times\boldsymbol{\nabla}B}{B^2} + \frac{mv_0^2}{qB_\parallel^*}\frac{\mathbf{B}\times\boldsymbol{\nabla}B}{B^2} + \frac{2mu_\parallel v_0}{qB_\parallel^*}\frac{\mathbf{B}\times\boldsymbol{\nabla}B}{B^2}. \tag{5.5}$$

We can consider the first term here to be the curvature drift in a co-moving frame, or a simulation with no rotation. The second and third terms are then new drifts that only occur in a rotating plasma. Inclusion of the background $E \times B$ drift, $\mathbf{u}_E$, is required to fully recover the Coriolis and centrifugal drifts within the laboratory frame.

By once again comparing to previous work in a co-moving frame performed

by Peeters [34], we see that these new terms can be approximately considered a centrifugal, v_{cf}, and Coriolis drift, v_{co}, respectively.

$$v_{cf} = \frac{mv_0^2}{qB_{\|}^*} \frac{\mathbf{B} \times \boldsymbol{\nabla} B}{B^2} \tag{5.6}$$

$$v_{co} = \frac{2mu_{\|}v_0}{qB_{\|}^*} \frac{\mathbf{B} \times \boldsymbol{\nabla} B}{B^2} \tag{5.7}$$

Although it is important to remember that the centrifugal and Coriolis forces are 'fictitious' forces and equations 5.7 and 5.6 are technically not new drifts, but still part of the lab frame curvature drift.

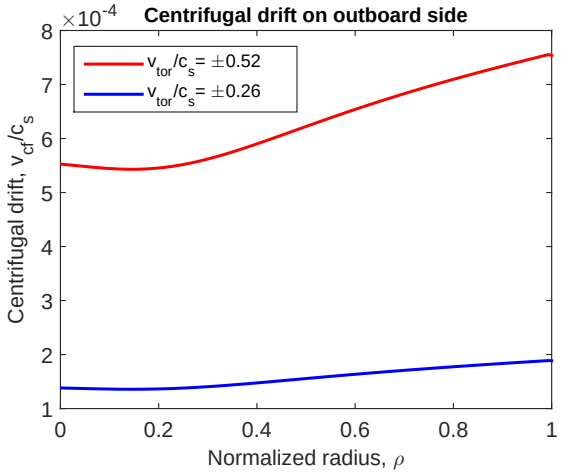

Figure 5.3: Centrifugal drift on the outboard side the tokamak as a function of radius, for several applied rotation rates.

As the centrifugal drift, equation 5.6, is proportional to only the parallel flow and not parallel velocity of each marker, we may calculate the size of the centrifugal drift on the outboard side of the plasma for the ions. The centrifugal drift resulting from the application of a background electric potential upon the plasma can be seen in figure 5.3 for several different imposed toroidal velocities. Due to the squared v_0 term in equation 5.6, the resulting direction of the drift can be expected to remain the same regardless of the direction of the applied toroidal rotation. Therefore, any stabilising effects of the centrifugal drift may be expected to be roughly symmetric with the direction of toroidal rotation

It is expected that the combination of the Coriolis and centrifugal drifts will together have a stabilising effect on the ITG mode. This has been observed in previous linear studies in a local gyrokinetic code [35].

Flow Shear Stabilization

It has been well documented and studied that a sheared flow can reduce, and sometimes completely suppress turbulence and the micro-instabilities which drive them [95, 96, 97, 98, 99, 100, 101]. In a basic picture, the flows act on either end of a radial mode structure differently which causes a tilting of the mode in the poloidal plane. As the mode is tilted, its growth rate is also reduced. A comprehensive review of turbulence supression caused by sheared flows has been written by Terry [102].

Although they are not a subject of interest in this thesis, the flows that arise spontaneously from profile variations may be large enough to cause some stabilisation as a result of shearing.

5.4 Frequency

To calculate the frequency of the mode present in a simulation, we read the perturbed electric potential at mid-radius on the outboard side. This gives a known perturbed potential for a defined position in the poloidal plane, but with varying ζ and time coordinates; $\phi_{s\theta}(\zeta, t)$.

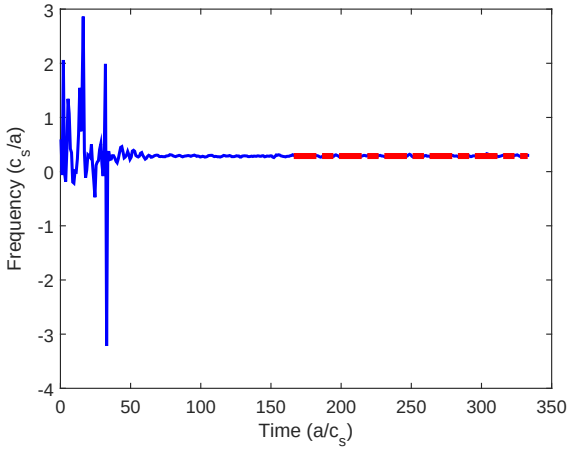

Figure 5.4: Calculated frequency changes with time. The blue line represents frequency calculated at each time step and the red line shows the mean taken across the last half of the simulation. A non-rotating case with n=24 is depicted above.

By taking the Fourier transform of this potential in the toroidal direction, we find a complex amplitude that is a function of the toroidal mode number, n, and time, t. As only one toroidal mode has been allowed to grow in each simulation, the corresponding mode can be easily isolated. The perturbed potential for the selected

toroidal mode would be expected to be of the form

$$\phi(m,n,t) \propto e^{-i(m\theta+n\zeta)}e^{-i\omega t}. \tag{5.8}$$

The exponential which is dependent upon m and n will remain constant in time. We can therefore identify a frequency by calculating the phase difference of the complex Fourier transformed potential between each adjacent time-step (giving $\omega\delta t$) and then dividing by the time-step size, δt. This will calculate a time-dependent frequency, as shown in figure 5.4.

Taking the mean of this series gives the frequency of the mode. However, the mean is only taken across the second half of the simulation as the signal to noise ratio in the early time-steps is poor.

As the plasma in the system is rotating toroidally as a solid body, this observed frequency will be subject to a Doppler shift which must be accounted for.

5.4.1 Doppler shifted frequency

The Doppler effect is a well known phenomenon that occurs when an observer is moving relative to the source of a wave. Therefore, in the case of a rotating plasma inside a tokamak, any frequency found in the laboratory frame would be expected to have been subject to this shift. The Doppler shift is given by

$$\omega_{measured} = \omega_{source} - \frac{\Delta v}{v_p}\omega_{source} \tag{5.9}$$

where v_p is the velocity of the wave in the plasma, Δv is the difference between the velocity of the waves source and the observer. ω_{source} and $\omega_{measured}$ are the frequency of the wave at the origin and the frequency as it appears to the observer (in the lab frame).

The origin of the wave is the rotating plasma and therefore the relative velocity between the source and observer is given by the toroidal velocity of the plasma. By taking advantage of the relation between frequency and wave number, we do not need to know v_p, since $k = \omega/v_p$. Additionally, since the desired frequency is ω_{source}, equation 5.9 can be rearranged to

$$\omega_{source} = \omega_{measured} + \Delta v k_\zeta. \tag{5.10}$$

Since $\Delta v = v_{tor}$, the desired frequency of the toroidal modes in a rotating plasma is given by

$$\omega_{source} = \omega_{measured} + v_{tor}k_\zeta \tag{5.11}$$

which can then be put into a more convenient form.

$$\omega_{source} = \omega_{measured} + n\Omega_t \tag{5.12}$$

where Ω_t is the toroidal rotation rate.

5.4.2 Results

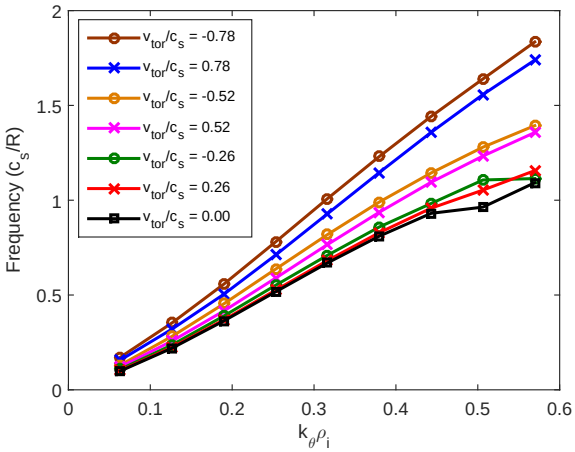

(a) Frequency as a function of $k_\theta \rho_i$, various solid body rotation rates were used.

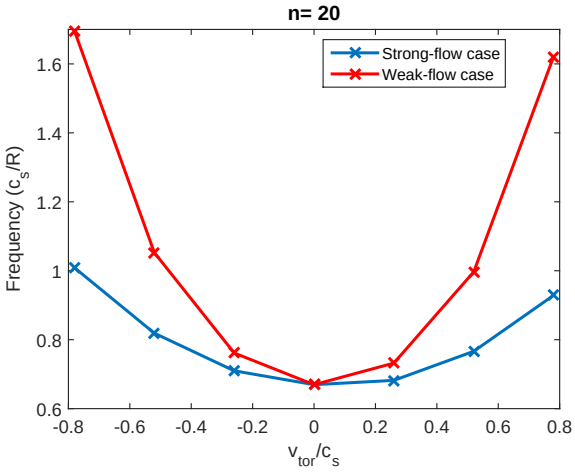

(b) Frequency as a function of applied toroidal velocity for $k_\theta \rho_i = 0.32$.

Figure 5.5: Frequency of the linear modes under various rotation rates.

The frequency measured for varying rotation rates is shown in figure 5.5a, plotted as a function of $k_\theta \rho_i$. As a sanity check, we can see that the non-rotating

case roughly matches previous simulations performed within ORB5 [89]. Results from each set of scans show a very consistent linear dependence upon $k_\theta \rho_i$. The gradient of this fit seems to increase with the magnitude of the toroidal velocity of the plasma. At large $k_\theta \rho_i$, the frequency was seen to change more unexpectedly, however this appears to be related to the growth rate of these modes approaching zero. As such, the these near-zero growth modes have not been plotted.

Further investigations are made by isolating results of the fastest growing mode in the non-rotation case, $k_\theta \rho_i = 0.316$. The frequency dependence upon toroidal velocity for this mode can be seen in figure 5.5b where results from equivalent weak-flow simulations have also been included. The results produce a very smooth curve describing the frequency, which is approximately symmetrical with the magnitude of v_{tor}. It can be clearly seen that the modifications made as part of this thesis once again act to greatly reduce the change in mode frequency with toroidal velocity. This was previously seen in section 4.4 and suggests that a change in density has a large effect on mode frequency. As noted earlier, there is a small toroidal flow present in even the non-rotating case from the profile gradients. It appears that this is the cause of the asymmetry we observe. The difference of frequency between $v_{tor}/c_{si} = 0$ and 0.26 is relatively small in the strong-flow case, which is likely because the actual toroidal velocity first decreases to 0 between these points before rising again.

The approximately symmetric dependence on toroidal velocity, is consistent with predictions that the centrifugal drift will be responsible for a change in frequency [34]. These results also show strong similarity to the variation of GAM frequency with toroidal velocity studied in section 4.4.

5.5 Growth Rates

The growth rate of the linear modes is found by analysis of the signal; which is as described in section 3.13.

For a linear simulation with only one toroidal mode, the signal can be used analogously with the field-energy of the desired mode. The signal is an exponential that grows with time and so we take a log (base 10) of the signal and fit a straight line. The gradient of this straight line is twice the growth rate of the mode. The growth rate is calculated this way instead of with a direct fitting to the signal because the noise also grows exponentially which can be detrimental to the fitting algorithms. A fit of the exponential signal therefore usually results in an inferior fitting when compared to a logarithmic fit.

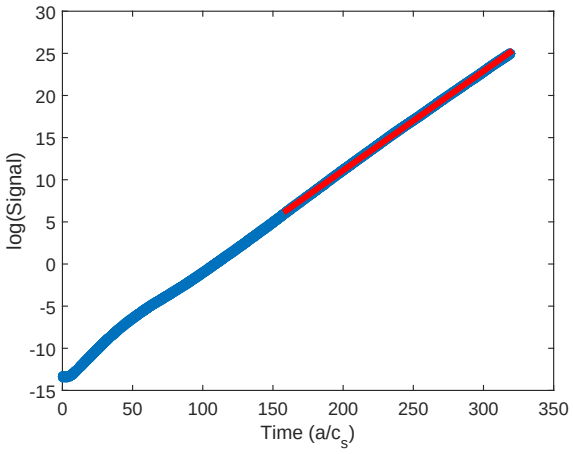

Figure 5.6: Mode growth rate is calculated by taking the gradient of a logged signal plotted against time. The red line indicates the linear fit found for the signal shown. This signal is taken from a non-rotating simulation with toroidal mode n=28.

To ensure an accurate value for growth rate is found, only the latter half of the simulation signal is used for the fitting. This is done to remove the early results where the signal to noise ratio is still low in comparison to the later time-steps. An example of a typical fit can be seen in figure 5.6, which shows early time fluctuations.

5.5.1 Results

It can be seen from figure 5.7a, that the introduction of a constant toroidal rotation in fact destabilises the plasma and causes a larger growth rate of the linear modes; although with an asymmetry depending on the direction of the applied toroidal rotation. A reasonable assumption may be that this asymmetry is caused by the flow generated from the profile gradients, however, this would likely not entirely account for the behaviour seen. It is likely that there is an already present stabilising effect from the profile gradient flow shear which the inertial terms are counter-acting.

Figure 5.7a also shows that there is a small shift in the wavenumber of peak growth as a function of rotation.

By again, focusing our attention on a single mode we may develop a clearer picture of the behaviour of the growth rate with a changing toroidal velocity. Figure 5.7b plots the growth rate against toroidal velocity for a mode with $k_\theta \rho_i = 0.32$. Here, we can see that a toroidal rotation initially causes the growth rate to increase, although not symmetrically with v_{tor}, however as the magnitude of v_{tor}/c_{si} approaches one there is a change and instead the rotation begins to reduce the growth rate. The reason for this behaviour is not immediately obvious but analysis of the

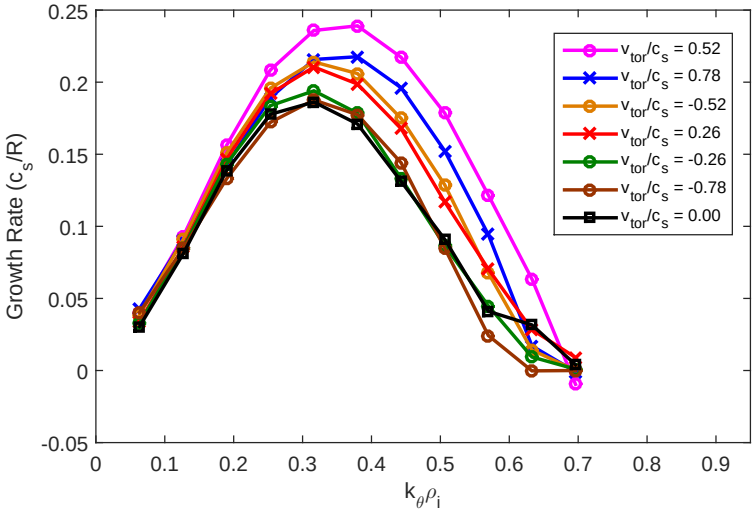

(a) Growth rate as a function of $k_\theta \rho_i$ for simulations with different toroidal velocities.

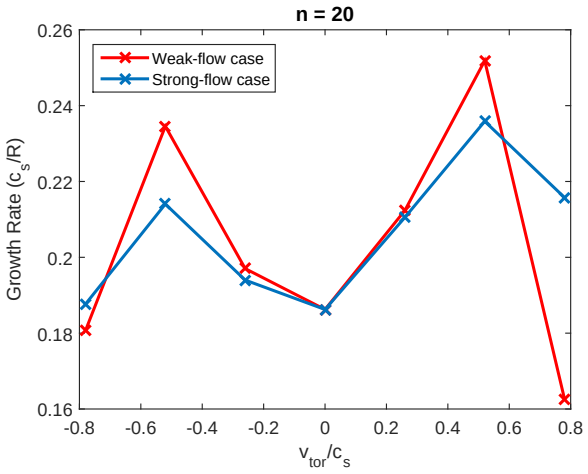

(b) Growth rate as a function of toroidal velocity for a mode with $k_\theta \rho_i = 0.32$.

Figure 5.7: The growth rate of linear modes plotted for differing $k_\theta \rho_i$ and v_{tor}.

mode structures in the poloidal plane will make this behaviour more transparent. This (initial) destabilisation suggests that the mode structures tilt, which will be analysed in section 5.6, is in fact being reduced in these simulations and lessening an already present turbulence suppression. Similar behaviour is seen in the weak-flow simulations, but with larger variation of growth rate.

5.6 Mode structures

The modes of a system can be seen in the perturbed potential to form structures, or eddies, in the poloidal plane. Tilting of these structures can occur for flow velocities that differ with radius, due to the plasma on either end of the eddies moving at different rates to each other. An eddy lying purely in the radial direction would be expected to grow more quickly than an eddy of an equivalent mode that is tilted poloidally. A simple picture could consider that as the two ends of an eddy move faster in relation to each other, the mode is tilted and then breaks apart. As this happens to each mode present in the tokamak, the result is a 'smoothing' effect.

The stabilization from tilting a mode structure is largely dependent upon the magnitude of this tilting angle, which we will label χ.

As can be seen in figure 5.8, when plotting the perturbed potential on the poloidal plane there are clear structures of high and low value. A modification of the toroidal velocity is seen to cause the tilting of these structures (or straightening) as well as lengthening (or contracting) in the radial direction.

5.6.1 Analysis

Using the same simulations as in section 5.5, we look at the tilting of individual modes and can relate the results to the modes stability. The method used here to analyse the mode tilting measured the angle which the mode structure on the outboard side ($\theta_* = 0$) makes with R, as shown in figure 5.9b. As the system is assumed axisymmetric, all measurements were made at the same toroidal angle.

This angle has been calculated by first identifying all peaks (and troughs) at a radius s_{low}; thus identifying each mode structure on the poloidal plane. If any of these mode structures have poloidal coordinate $\theta_* \sim 0$, the poloidal position of the same structure is then measured at a higher radius s_{high}. The coordinates of both ends of a single mode structure $(s_{low}, 0)$ and $(s_{high}, \theta_{peak})$ are then known. From these coordinates, the angle χ may be calculated with simple trigonometry; shown in figure 5.9b. Angle χ is defined so that a negative value indicates a structure that is tilted downward, and a positive value indicates an upwards tilt.

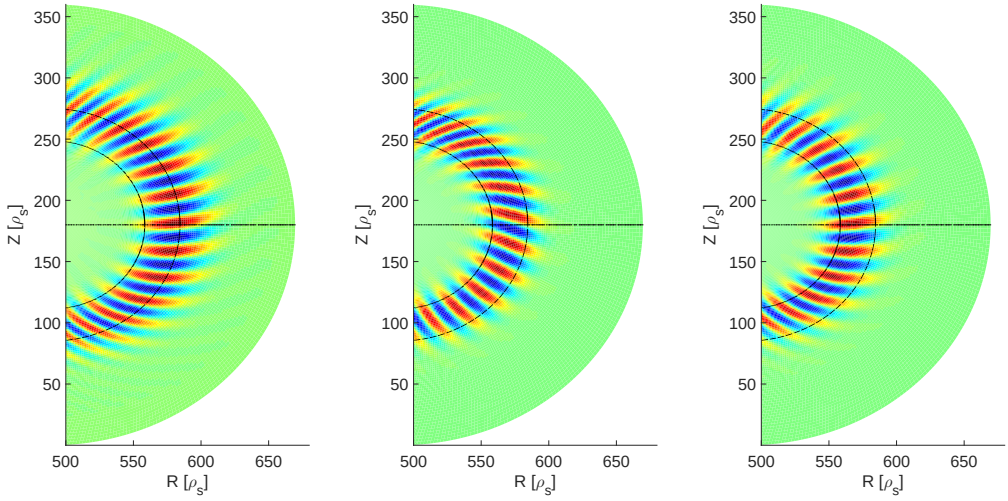

Figure 5.8: Poloidal cross-section of the perturbed electrostatic potential for different toroidal velocities. From left to right: $v_{tor} = -0.78c_s$, $0c_s$ and $0.78c_s$. A tilting is already present in the non-rotating case and the radial length of the structures also appears to vary with toroidal velocity.

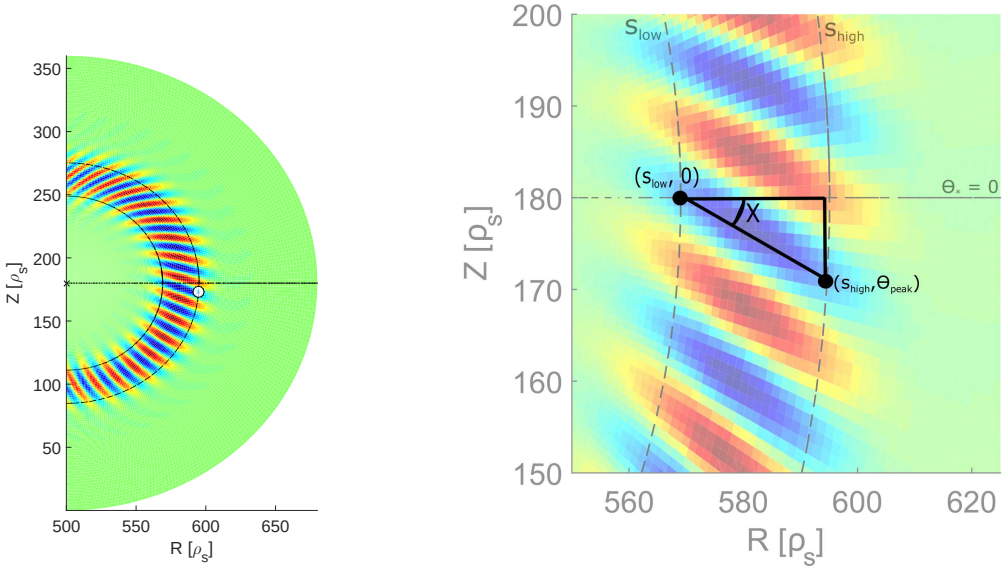

(a) A mode structure with coordinates $\theta_* \sim 0$ at s_{low} is measured at higher radius. A peak is found as shown by the white marker.

(b) Tilting angle χ is calculated with simple trigonometry from two known sets of coordinates. A downwards tilting is defined as negative and upwards tilting mode has positive χ.

Figure 5.9: Tilting angle χ is calculated from measurements taken at two radial positions s_{low} and s_{high}.

To account for cases where the tilting is so large that the peak closest to $\theta_* = 0$ at s_{high} does not correspond to the mode structure of interest, a mid point s_{mid} may be used to assist in identify the actual peak of interest at s_{high}.

This process is repeated for each time-step and a time-average is then taken of χ across the last half of the simulation. The time-average should help mitigate any other small fluctuations present in the perturbed potential.

The radii at which measurements were taken, s_{low} and s_{high}, were the radial positions at which the magnitude of the perturbed potential along $\theta_* = 0$ dropped to one quarter of its peak value (the potential was first integrated in the toroidal direction to provide a smooth curve). This ensured that measurements were taken at equivalent points on the mode structure in every simulation.

5.6.2 Results

Variation of χ as a function of the applied toroidal velocity is shown in figure 5.10 for the fastest growing mode, $k_\theta \rho_i = 0.32$. Very similar behaviour can be seen from the results with different $k_\theta \rho_i$; the relative size of χ shows some small variation. It can be seen that the application of a solid body rotation here acts to increase χ (tilt the mode upwards), regardless of the sign of rotation. This results matches earlier findings of growth rates in section 5.5 which showed an increase with larger applied toroidal rotation. As χ initially approaches zero the growth rate increases, but when χ gains a positive value the toroidal rotation begins to act to reduce the growth rate.

It can bee seen from figure 5.8 and figure 5.10 that the 'non-rotation' case has an already present tilting of mode structure in the poloidal plane ($\chi \sim -0.3$). This is a result of the equilibrium profile radial gradients present in the simulation, which lead to a tilting of modes and a stabilising effect upon the ITG mode. Similar observations have been made within ORB5 previously, with a similar diamagnetic shear causing an asymmetry in the effects of an $E \times B$ shear stabilisation [19, 103]. Since a local code maintains equilibrium profiles which are constant with radius, this is an effect which would not be observed in a local simulation and is only retained within a global code.

This suggests that the inertial forces, and their drifts, act to tilt the mode structures. Though, for cases with an already present mode tilting (a negative χ) they must first act to reduce this angle to zero. Results from figure 5.10 show that large rotation rates may be required before any benefit can be found from the inertial forces added by a rotation. For a CYCLONE-like system, even the effect of inertial terms when $v_{tor}/c_{si} \sim 0.8$ are not enough to outweigh the benefit given by

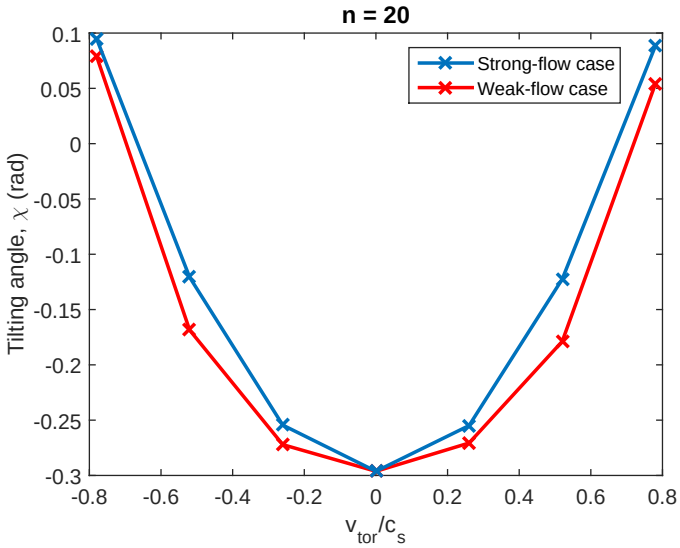

Figure 5.10: Tilting angle as a function of toroidal velocity for mode with $k_\theta \rho_i = 0.32$. $\chi < 0$ indicates a mode tilted 'downwards'.

the inherent diamagnetic shear.

Further comparison of figures 5.7b and 5.10 reveal an apparent discrepancy. It can be seen that the growth rate of the $k_\theta \rho_i = 0.32$ mode is lower for the simulation which has $v_{tor}/c_s = -0.78$ than the positive rotation equivalent. However, figure 5.10 shows that χ is of a similar size in each case. Clearly, the tilting of the mode does not fully describe the stabilising effect of the inertial forces.

This apparent discrepancy can be explained by the radial length of the structures. Figure 5.8 shows that the simulation for a negatively rotating plasma has eddies which cover a wider radial region than the positively rotating case. An increase in the radial length of a mode structure is also known to provide a stabilizing effect. The reasons for this increased stability are very similar to the increased stability with growing χ. As the radial length of the mode structure rises, the distance between either end of the mode structure increases. As a result, the mode structure undergoes a more substantial shearing effect. This helps explain the lower peak growth rate found in the negative direction, as the mode structures will have different lengths when lying along the $\theta_* = 0$ axis.

Furthermore, the weak-flow results that are also shown in figure 5.7b show very similar tilting angles to the strong-flow simulations. This seems to indicate that the larger variation in growth rate previously observed for the weak-flow case (when compared to the strong-flow simulations), may once again be related to a change in particle density.

This behaviour suggests that both the Coriolis and centrifugal forces contribute to the stabilisation of modes in linear simulations through a mode tilting effect.

In experiments this could lead to a reduced stabilising effect when a sheared radial electric field is applied to a tokamak. The change in growth rate as a result of solid body rotational effects would likely not exceed any sheared flow effects in experimental studies.

5.7 Toroidal Momentum Pinch

Investigations into the toroidal momentum pinch effect can be made by considering the quasi-linear fluxes. We look for an inward toroidal momentum flux as a result of the Coriolis force (which appears in a co-moving frame)[96, 91].

The toroidal momentum flux (Γ_ζ) is approximated here with the parallel momentum flux ($\Gamma_\parallel$) and is normalized by the heat flux (Q). This approximation is valid because we are performing investigations of a large aspect ratio device, for which the parallel direction is approximately the same as the toroidal direction. A different diagnostic routine may be required for investigations of the toroidal momentum flux in a spherical tokamak. Observations of the momentum flux are taken as a time average across the last half of the simulation and then averaged across a radial width of $0.2a$, centred around $\rho = 0.5$.

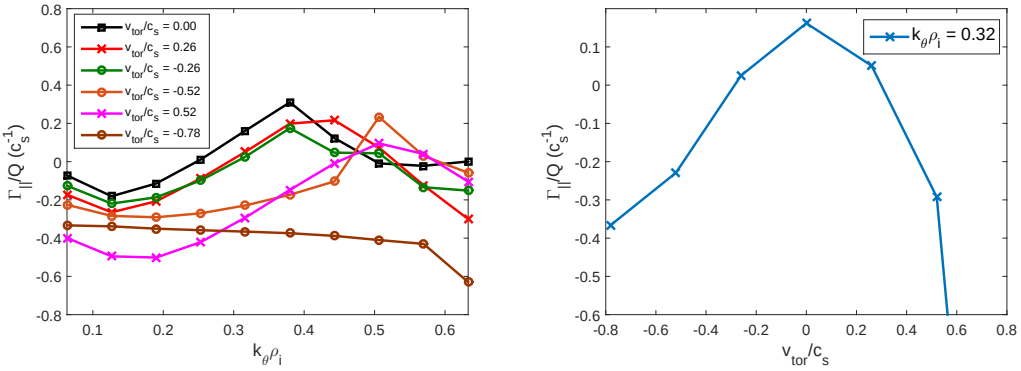

(a) Γ_ζ/Q as a function of $k_\theta\rho_i$ for various toroidal velocities.

(b) Ratio of parallel momentum flux to heat flux as a function of toroidal velocity for mode with $k_\theta\rho_i = 0.32$.

Figure 5.11: Toroidal momentum flux is approximated as parallel momentum flux.

Figure 5.11a shows that as $k_\theta\rho_i$ increases, the momentum transport tends to grow causing a larger outward momentum transport. However, it can also be

seen that a toroidal rotation has an effect upon the size and direction of momentum transport. Momentum transport has a peak value in $k_\theta \rho_i$ which moves to higher k_θ as toroidal velocity increase. Simulations with $v_{tor}/c_{si} = 0.78$ were also performed but have not been plotted here due to their negative toroidal momentum flux with a very large magnitude (approximately -2).

By again selecting the fastest growing mode (in a non-rotating case) $k_\theta \rho_i = 0.32$, we can develop a clearer image of the effects of a toroidal rotation upon momentum transport. Figure 5.11b illustrates that a toroidal rotation (in either direction) first decreases the momentum transport to zero and then leads to an inwards pinch effect on the toroidal momentum. It appears from these results that the gyro-fluid model predictions made by Peeters, which suggest that adiabatic electrons will result in no pinch, may not be completely accurate [93, 94]. Although the pinch does seem small, observations do show an increase in inwards pinch with higher rotation rates.

In a non-linear simulation this may result in an increase in the magnitude of v_{tor} towards the core region, and may introduce an $E \times B$ shear that will in turn act to reduce heat transport in the system.

The reason for the asymmetry of the pinch effect is not immediately apparent, and the large inward momentum pinch for high positive toroidal velocity is an unexpected result which suggests some other unknown effect may be causing changes to the toroidal momentum transport. This asymmetry has not been observed in local gyrokinetic codes, which suggests that it is caused by the additional flows that arise from the profile gradients. This seems a reasonable conclusion when also considering the similar asymmetry observed for the frequency and growth rate of modes found previously.

5.8 Summary

In this section, linear investigations of strongly rotating plasmas have been performed in the global limit. To this end, the expected behaviour of rotational terms were first outlined by considering a co-moving frame. Predictions have previously been made in a series of papers by Peeters [91, 34] for a co-moving frame in the local limit, which show that the rotational effects can largely be described by a centrifugal and Coriolis force acting on the plasma.

Linear simulations have been performed with parameters matching the CYCLONE base case and measurements of the frequency and growth rate have been taken for individual toroidal modes. Reasonably good agreement was found for

changes of mode frequency between global simulations performed in ORB5 and predictions made in the local limit, however, flows which arise from the profile gradients were found to cause substantial deviations of the growth rates from predictions. An already present stabilising effect was found as a result of the diamagnetic flows in global simulations which counteracted stabilising effects of the inertial terms.

Due to the existence of these profile gradient flows, investigations have concluded that there may be substantial differences between local and global codes in regards to the growth of linear modes for a strongly rotating plasma.

Comparisons between strong and weak-flow forms of ORB5 reveal a substantial difference between the scaling of mode frequency and growth rate with changes of toroidal velocity. However, it is important to note that a significant amount of this change may come from the introduction of a density correction term along with the strong-flow modifications.

Furthermore, an inwards toroidal momentum pinch effect was observed despite predictions that there should not be one for simulations with adiabatic electrons. However, it is not clear whether this pinch is entirely caused by the Coriolis force.

Chapter 6

Collisionless non-linear simulations

6.1 Introduction

We now move on to perform non-linear simulations, which provide a more detailed view of the development of turbulence in a tokamak. In a linear simulation, the non-linear term in the Vlasov equation which couples the perturbed distribution with the perturbed electric field is ignored, but this is retained in non-linear simulations.

Toroidal Fourier modes couple together non-linearly and so a simulation must include toroidal modes of numbers within a significant range to be consistent. Most importantly the n=0 modes are required (zonal flows) as these regulate the turbulence and are important in determining the nonlinear saturation state.

All of the nonlinear simulations performed in this chapter were performed with CYCLONE like parameters similar to those used in chapter 5, but with different temperature and density profiles. For these non-linear simulations the plateau profiles, equilibrium profile 2 in section 3.9.2, with gradient scale lengths $R/L_T = 6.92$, $R/L_n = 2.22$ and temperature ratio $T_e/T_i = 1$ were used for the tuning simulations. R/L_T and R/L_n were increased from section 6.3 onwards by 20% to ensure that sufficient turbulence arose for analysis. The other parameters were $\Delta T = \Delta n = 0.04$ and $\Delta r = 0.4a$ with a domain centred around $r = 0.5a$ and radial width a.

For these simulations, a toroidal wedge corresponding to half of the tokamak is considered, which means every second toroidal mode is kept in the simulation. Toroidal modes up to $n = 90$ are included in these simulations, corresponding to $k_\theta \rho_i = 1.41$. The system size was $\rho_* = 1/180$ with $a = 0.625m$ and $R_0 = 1.7m$. The

field grid size was $N_s \times N_\theta \times N_\zeta = 128 \times 512 \times 256$ and the safety factor is given by

$$q(\rho) = 0.86 - 0.16\rho + 2.52\rho^2 \tag{6.1}$$

which gives $q = 1.41$ and $\hat{s} \sim 0.8$ at $r = 0.5a$.

The initial conditions of a non-linear simulation can have a large impact upon the final state that the system reaches and so the initial perturbation remained consistent between all non-linear tests performed. The GENE perturbation was used, as given by equation 3.78, acting on toroidal modes of value ranging from 2 to 90. An initial perturbation was therefore applied to each mode present in the simulation, with the exception of the zonal modes. This exclusion was made to allow the zonal flows to grow non-linearly in the simulation naturally.

Typically, a non-linear simulation in ORB5 can be expected to go through two or three different phases. The first is the linear phase during which the various modes present in the simulation grow exponentially until they reach an amplitude at which they saturate. This saturation amplitude is not known prior to the simulation. The length of this linear phase varies depending upon the growth rate of the mode and its saturation amplitude, and as such the time that the linear modes spans is also unknown apriori. In the simulations presented in this chapter, the linear phase was typically found to be approximately $10 - 35[a/c_s]$. Following this, there may be an "over-shoot" period if the $n = 0$ zonal flow takes longer to reach its saturated amplitude than the other modes (the length of this period can vary, if it is present at all). If this occurs then the other modes will subsequently be damped by the zonal flow, leading to a reduction in the amplitude of the turbulence.

After the over-shoot period, the simulation should reach a quasi-equilibrium steady state. It is at this point in the simulation which comparisons with experiments are usually made or the transport caused by the turbulence is considered. It is often useful when looking at information from the quasi-steady state of a non-linear simulation to take the time-average of the desired quantity. A requirement is then that the simulation continues for a significant time after reaching this final state to allow an averaging over a substantial time window.

6.2 Tuning and noise reduction

Non-linear simulations in ORB5 can be extremely sensitive to physical or numerical variations of parameters and as such it is important that several different input parameters are adjusted to give optimum results from each simulation. Unfortunately, many of these inputs must be adjusted manually and so it can require a substantial

amount of computing time to set up a series of non-linear runs.

The most significant result that comes from this fine-tuning of the simulation parameters is an improvement of the signal to noise ratio (S/N) in the subsequent non-linear simulations. It is vital that this ratio is appropriately high as it has previously been found that a simulation must have a signal to noise ratio of at least 10 in order to contribute useful and reliable results; although the higher the ratio the better [90]. Global particle-in-cell simulations in particular have a known problem with the generation of noise over a simulation long enough for the turbulence to reach a quasi-steady state [64]. By using the equations given for signal and noise, in section 3.13, it is possible to plot the development of this ratio with time.

Numerous simulations are performed in this section with the purpose of improving the signal to noise ratio for the rotating non-linear simulations. This tuning has been performed in the past for non-linear simulations in a CYCLONE-like case but they are repeated here to ensure that they still work as intended after modifications to ORB5.

6.2.1 Marker number

An obvious first step to achieving a high S/N ratio in a particle-in-cell code is ensuring that a sufficient number of markers are used in the simulation. However, simulations become more computationally expensive with increasing number of markers and so care must be taken to find a balance between a marker number high enough to accurately represent the gyrokinetic model of ORB5 and low enough to run complete simulations within a reasonable time. The scaling of noise to marker number is given to be $N^{-1/2}$, where N is marker number. Therefore, increasing the signal to noise ratio by a factor of 2 would theoretically require a 4 times increase in the number of particles. From this relation, it can be seen how increasing the accuracy of simulations can quickly become extremely computationally expensive.

The dependence upon the number of markers in a non-linear simulation and the size of the S/N ratio has been investigated and the results are shown in figure 6.1. These simulations were performed for 50 million and 100 million markers. For reasons discussed in section 6.2.2, a heating term $\gamma_H = 0.02c_s/R$ has also been used in these simulations to maintain a larger signal at late time. No coarse-graining was used in these simulations; largely because of the relation between the number of bins and the number of markers discussed in section 6.2.3.

It can be seen in figure 6.1 that an increase in the number of markers significantly increases the S/N ratio. The increase found here was an approximate doubling of S/N ratio, which notably exceeds the improvements of $\sqrt{2}$ times that

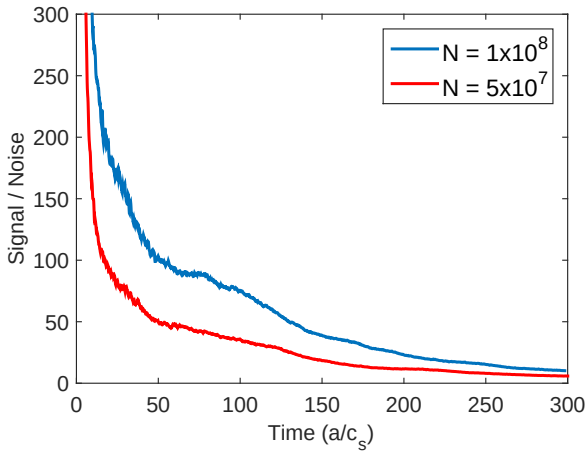

Figure 6.1: Dependence upon the number of markers for signal to noise ratio was plotted for two different cases. Both cases have a heating rate of $\gamma_H = 0.02[c_s/R]$ and made no use of noise control schemes.

would be expected. However, such a substantial increase will not always occur with increasing marker number, and it is fortunate that such a large boost can be applied in this case.

Following the analysis of these simulations, it was decided that $N = 100M$ provides a suitable level of accuracy and so all further simulations described in this chapter will have 100 million ion markers. Although the signal to noise ratio shown here is lower than would generally be desired, it will later be seen that the coarse-graining can make a large improvement without requiring more markers, and therefore keeping the computational cost reasonable. Similar to the linear simulations, the non-linear simulations used 512 cores but ran for close to 16 hours in order to achieve the desired accuracy given by 100M markers.

6.2.2 Heating Operator

In non-linear simulations, the anomalous radial heat flux from the turbulence will cause a relaxation of the profiles which will inhibit the drive for the micro-instabilities that are generating the turbulence. In order to counteract this profile relaxation, a source of heating may be introduced into the system without affecting the physics. The heating source is introduced by adding a new term to the Vlasov equation:

$$\frac{\mathrm{d}\delta f}{\mathrm{d}t} = \tau\left(\mathbf{E}\right) + S_H\left(\epsilon, s\right) \tag{6.2}$$

where S_H is a heating source which is given by

$$S_H(\epsilon, s) = -\gamma_H \left\{ \delta f(\epsilon, s) - f_0(\epsilon, s) \frac{\int d\mathbf{v} \delta f(\epsilon, s)}{\int d\mathbf{v} f_0(\epsilon, s)} \right\}. \tag{6.3}$$

This works by applying a poloidally independent source across each flux surface acting to damp the perturbed distribution function. The second term in equation 6.3 is a correction to the heating term used to conserve density, since

$$\int d\mathbf{v} S_H(\epsilon, s) = 0. \tag{6.4}$$

This source term is added only to reduce profile relaxation in the simulations. Although this thesis investigates rotation profiles, there is no source of momentum included in the simulations. The toroidal rotation is already included in the original state of the system.

The input parameter, γ_H, must be manually adjusted and is typically taken to be about one tenth the size of the maximum linear growth rate, which will depend on the physical parameters of the system [63, 64]. This ensures that the time scale over which the heating term affects the temperature is an order of magnitude smaller than the linear phase. The relaxation of profiles that occurs in the absence of a heating term is undesirable because we wish to define the profiles studied in the quasi-steady state ourselves. Additionally, a profile that continues to change throughout the quasi-steady state will cause variation in the resulting fluxes. As the heating term should not directly affect the physics of the simulation, it is expected that signal to noise ratio should have little variation with γ_H at early time-steps. However, a higher signal will be seen at late time steps due to the heating operator acting to maintain drive for the turbulence.

It was found in section 5.5 that the maximum growth rate in the CYCLONE base case is $\gamma_{max} \sim 0.2 c_s/R$ and so a heating rate of $\gamma_H = 0.02 c_s/R$ is a good initial estimate. In figures 6.2 and 6.3, simulations have been run with 100M markers and $\gamma_H = [0, 0.02, 0.05] c_s/R$. Coarse-graining was used in these simulations, with a coarse graining grid $N_s \times N_{\theta_*} \times N_\zeta \times N_{En} \times N_\lambda = 128 \times 32 \times 128 \times 32 \times 32$ and a coarse-graining relaxation rate $\gamma_{cg} = 0.45 c_s/R$.

It can be seen in figure 6.2 that S/N is not substantially affected by the heating term, except for slightly higher values at late time.

In addition to the signal to noise ratio, one can also observe the temperature gradient scale length, R/L_T, averaged over a radial window between $r = 0.4a$ and $r = 0.6a$ and varying with time. The variation of R/L_T in figure 6.3 illustrates that applying a heating term reduces the relaxation of the temperature profile.

The heating rate used in future simulations is taken to be $\gamma_H = 0.02 c_s/R$

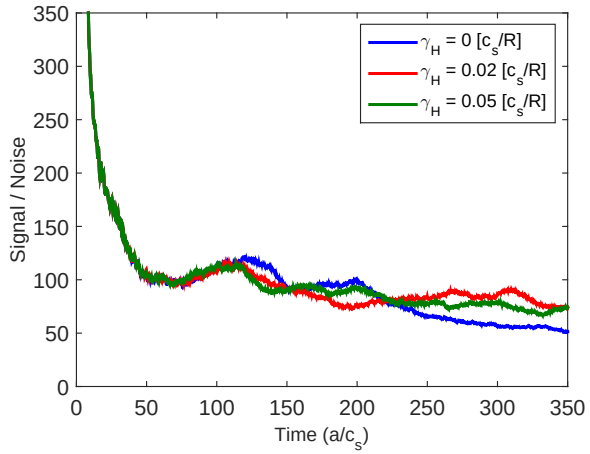

Figure 6.2: The signal to noise ratio for 100M markers can be seen to remain mostly unchanged by a heating term.

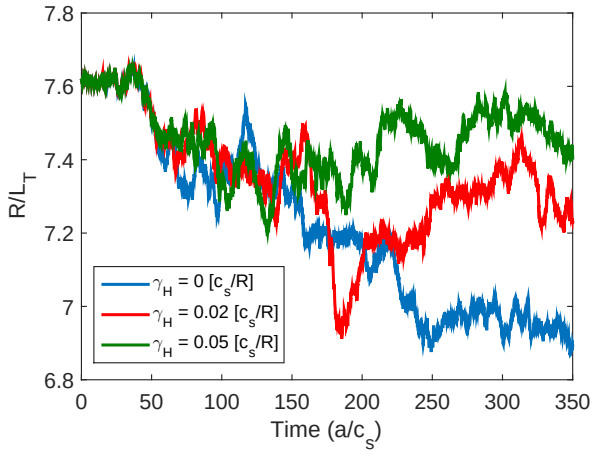

Figure 6.3: R/L_T as a function of time, plotted for varying heat rates.

after analysis of the results included in figure 6.3. It was found that this led to an acceptable reduction in the profile relaxation.

6.2.3 Coarse-graining

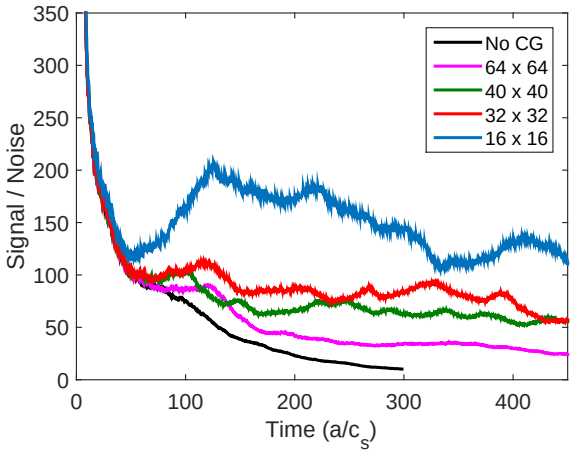

Figure 6.4: The signal to noise ratio in a CYCLONE base case for varying values of $N_\lambda \times N_{En}$. The signal to noise ratio in the absence of any coarse-graining is given by the black line.

An extremely important step in setting up non-linear simulations while maintaining an acceptable level of noise is selecting the correct parameters for the coarse-graining [63]. As first discussed in section 3.13, the coarse-graining is the most commonly used noise control method implemented in ORB5 but does require manual adjustment to get the best performance. A coarse-graining rate of once every 10 time steps per marker has been selected, $n_{cg} = 10$, and is a commonly used value for ORB5 simulations. This reduces the number of markers required proportionally to the number of bins; by a factor of 10.

The size of the coarse-graining grid can generally be taken to match the grid that the potential is stored on. This ensures that the coarse-graining does not act on turbulence at a level that may have physics relevant to the simulation. However, this can be improved upon by using a field-aligned grid which allows larger bin sizes in the poloidal direction whilst still not damping the physically relevant scales. The use of such a grid leads to a requirement of only 32 coarse-graining bins in the poloidal direction for ORB5 [63], greatly reducing the number of total coarse-graining bins used.

This still leaves several parameters for the coarse-graining noise control scheme which must be fine-tuned manually. The first of these is the total number of coarse-

graining bins (bin numbers in some directions of phase space are not set by the field grid size), which has to be carefully balanced to ensure at least two markers in each bin when a coarse-graining is performed. The condition that arises from this constraint is that the ratio of marker to bin number must be (at least) of order $1/n_{cg}$, in this case 1/10 [63]. As the coarse-graining bins are across the entire phase space, the grid resolution in energy, N_{En}, and pitch angle, N_λ, are important and can be adjusted.

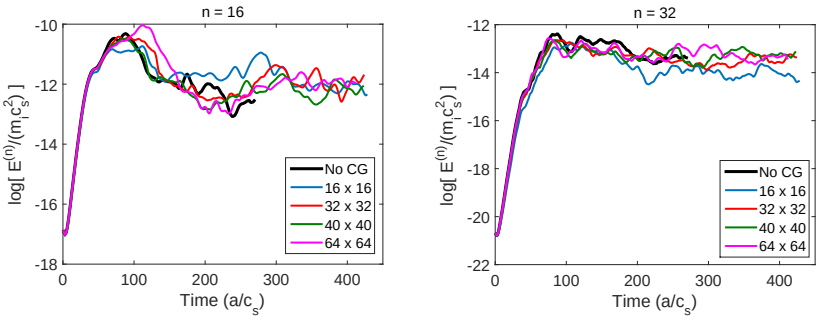

Figure 6.5: The electric field-energy spectrum for two different toroidal modes in the CYCLONE base case with varying values of $N_\lambda \times N_{En}$ are plotted. The energy spectrum in the absence of any coarse-graining is given by the solid black line.

For the grid sized used in these non-linear simulations, the number of coarse bins in the physical directions are $N_s \times N_{\theta_*} \times N_\zeta = 128 \times 32 \times 128$ which represents bins across half the torus (since one of every two toroidal modes are kept). Therefore, the number of total coarse-graining bins across the entire phase space is given by $128 \times 32 \times 128 \times N_{En} \times N_\lambda$. For $N_{En} = N_\lambda = 40$ this gives approximately 840M bins, and therefore 100M markers should provide a high enough number of markers per bin for the coarse-graining. We therefore take this as an initial estimate.

Figure 6.4 shows the S/N ratio and figure 6.5 the energy spectrum for two selected toroidal modes with varying numbers of coarse-graining bins. 100M markers were used in each simulation, with a heating rate $\gamma_H = 0.02 c_s/R$ and a coarse-graining relaxation rate $\gamma_{CG} = 0.45 c_s/R$. It can be seen that coarse-graining does improve the S/N of each simulation, but as the number of bins increase the S/N ratio drops. This is as would be expected, since fewer markers will be present in each bin if the bins themselves decrease in size. Averaging over more markers with each step will result in a higher reduction of noise, however, it will also have a greater effect on the physics of each mode. The energy spectrum of the modes shown in figure 6.5 indicate that there is a larger variation from the non-noise controlled simulations when using fewer bins. A balance between signal improvement and minimal changes to the physics of the simulations is desired.

It was decided that for these simulations, $N_{En} = N_\lambda = 32$ provides the best balance. Although $N_{En} = N_\lambda = 16$ gives a larger improvement to the S/N ratio, its effect on the physics of the simulations was judged too large in comparison to the benefits given.

Finally, the relaxation rate of the coarse-graining must be decided for the simulations that are to be performed. Unfortunately, the optimal relaxation rates are specific to the physical quantities of the simulation and are not at all universal. Therefore, to decide on an appropriate value a scan over varying relaxation rates is performed. The only requirement for the relaxation rate is $(n_{cg}\Delta t) \cdot \gamma_{cg} \leq 1$, with the full relaxation of all weights within a bin to their average value occurring for $(n_{cg}\Delta t) \cdot \gamma_{cg} = 1$. The time step size is chosen to be $\Delta t = 20\Omega_{ci}^{-1}$. This therefore imposes a requirement on the relaxation rate of $\gamma_{cg} \leq 1/(n_{cg}\Delta t) = (5 \times 10^{-3})\Omega_{ci} = 0.9c_s/R$ in these simulations.

A scan over several different relaxation rates, $[0, 0.225, 0.45, 0.9]c_s/R$, was performed. The resulting signal to noise ratio can be seen in figure 6.6, which along with comparisons of the energy spectrum for several toroidal modes, shown in figure 6.7, allows us to select the most appropriate relaxation rate. In these simulations, the same heating rate has been used of $\gamma_H = 0.02c_s/R$ and a coarse-graining grid of size $N_s \times N_{\theta_*} \times N_\zeta \times N_{En} \times N_\lambda = 128 \times 32 \times 128 \times 32 \times 32$.

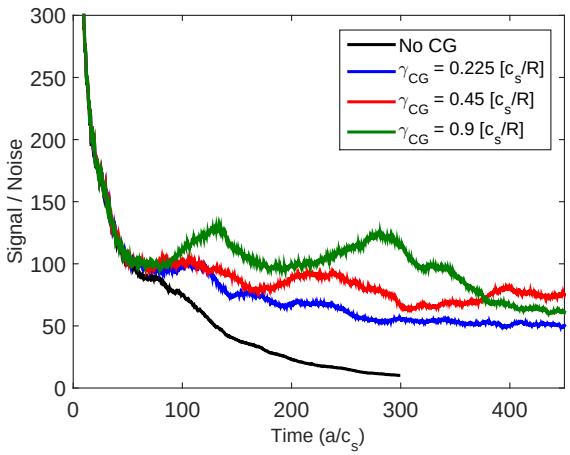

Figure 6.6: The signal to noise ratio as a function of time shows improvements for appropriate coarse graining rate γ_{cg}.

From these results, it was decided the coarse-graining rate that gives the best improvement to the S/N ratio of the simulation while minimising the effects on the growth and behaviour of the modes is given by $\gamma_{cg} = 0.45c_s/R$. Although $\gamma_{CG} = 0.9c_s/R$ does give a better S/N ratio in the earlier time-steps it provides

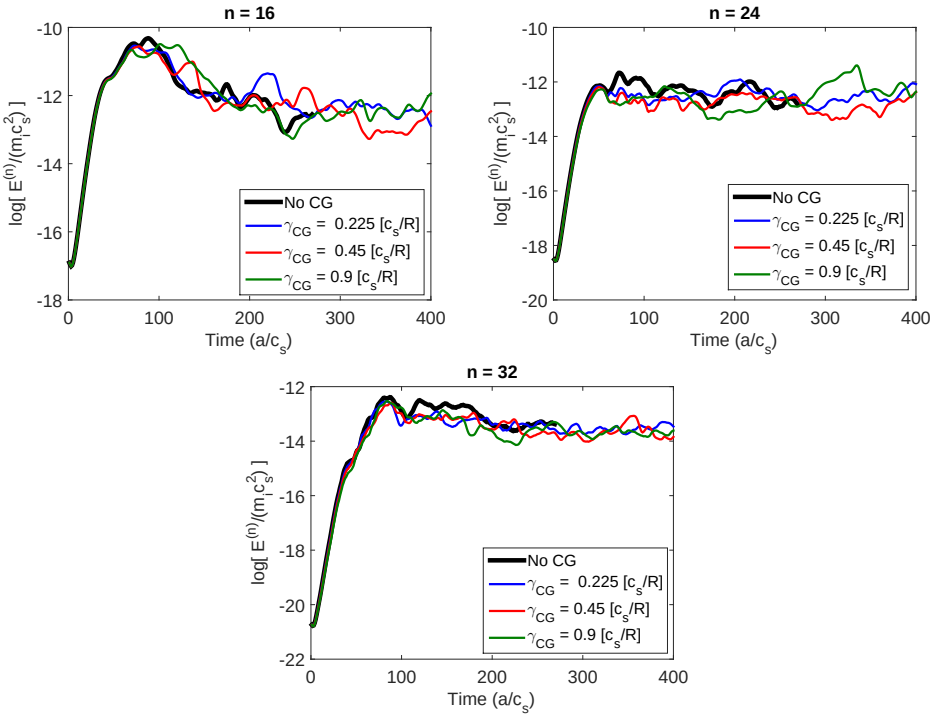

Figure 6.7: The electric-field energy spectra of modes with n = 16, 24 and 32 are seen to vary with differing coarse-graining rate γ_{cg}.

little improvement at later times. Additionally, the variation of the various energy spectra seen in figure 6.7 is considered to be unacceptably large for $\gamma_{CG} = 0.9c_s/R$.

The final coarse-graining parameters are taken as $N_s \times N_\theta \times N_\zeta \times N_{En} \times N_\lambda = 128 \times 32 \times 128 \times 32 \times 32$, with a coarse-graining rate of $\gamma_{cg} = 0.45c_s/R$.

6.3 Results

After adjusting noise control and heating parameters with the non-rotating case, the same parameters can be used over numerous rotating simulations. This will ensure that the effects on the physics and noise of the simulations will remain constant despite the other changes that will occur between the simulations themselves.

In a non-linear simulation, the main point of interest is usually the quasi-steady state, as this is where the flux and diffusivity can be studied and also where any comparisons with experimental results would be made. Although often the interest is not in the time-variation of the transport, but its time average. This is because despite small variations, the transport would be expected to remain largely the same during this phase and so an average over time should gives a good estimate

of transport for comparison between simulations.

In order to get a good result, we aim to continue the simulation for at least 500 (a/c_s) after reaching the quasi-steady state. Although the transport may be expected to remain approximately constant during this time, it is worth noting that the rotation profile may still be evolving due to the toroidal momentum flux. Studies of turbulent transport within gyrokinetic codes have been well documented, for more information the reader is directed to a review by Garbet [104]. The flux is here presented in gyro-Bohm units, $\chi_{GB} = c_s \rho_s^2 / a$.

For these simulations, R/L_T and R/L_n were also increased by 20% from values used during the earlier parameter adjustment. This change was made to promote larger fluxes and to ensure that all simulations will contain substantial turbulence.

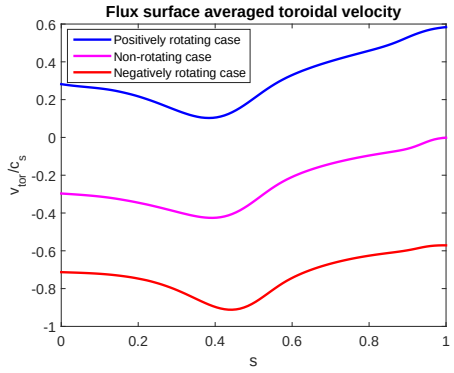

(a) There is a sizeable velocity present in the 'non-rotation' case, and a substantial radial gradient.

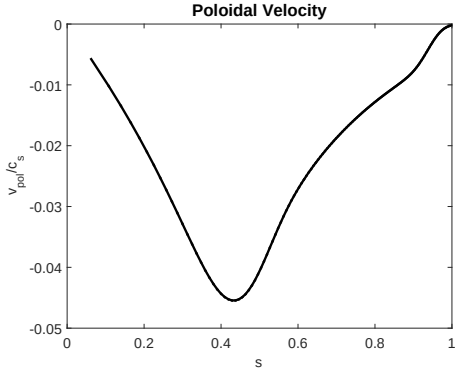

(b) Poloidal velocity remains largely constant across all simulations.

Figure 6.8: The velocity profiles of the non-linear simulations performed; for a non-rotating, negatively rotating and positively rotating plasma.

An effective diffusivity can be calculated from the non-linear results for various transport quantities. This effective diffusivity assumes that the transport is a purely diffusive process, which is likely not the case. As has been discussed in the previous chapter, the momentum transport may have contributions from a Coriolis pinch, and so will not be purely diffusive. The effective diffusivity is given by

$$\chi_G = \frac{\Gamma_G}{\nabla G} \tag{6.5}$$

where ∇G is the equilibrium gradient of G and Γ_G is the flux of quantity G.

It is convenient when analysing the transport properties to take either an average across a radial width ($r = 0.4$ to $r = 0.6$) or to look at a time-average that

has been taken over the last half of the simulation.

Simulations with solid-body toroidal rotation profiles were performed with applied toroidal velocities, $v_{tor} = [-0.52, 0, 0.52]c_s$. Equivalent weak-flow simulations were performed as well, though the positively rotating simulation was ended approximately 50 (a/c_s) early due to a low signal to noise ratio negatively effecting the results (S/N < 20). The resulting toroidal velocity profiles of the simulations can be seen in figure 6.8a. The poloidal velocity for each simulation remained approximately constant, at the value shown in figure 6.8b; this poloidal velocity is a result of the profile gradients.

6.3.1 Non-rotation case

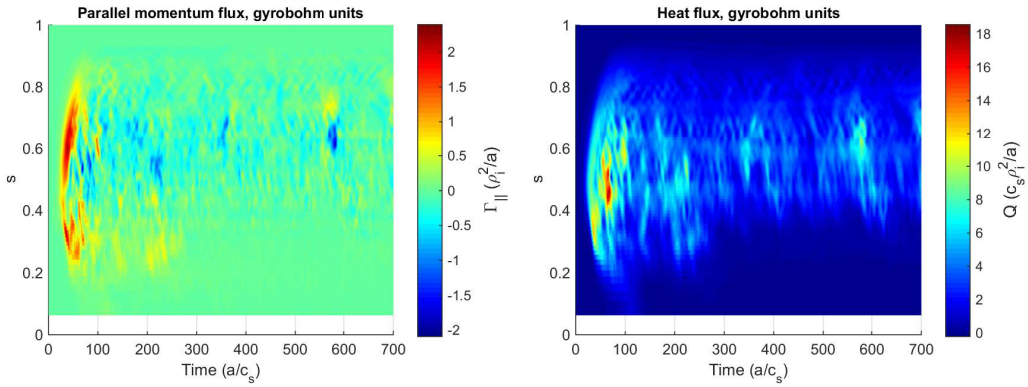

(a) Parallel flux, in gyrobohm units.

(b) Heat flux, in gyrobohm units.

Figure 6.9: Heat and parallel flux for non-rotating case.

The radial flux of parallel momentum and heat for a non-rotating simulation can be seen in figures 6.9a and 6.9b respectively. They show avalanche-like bursts, which are a common feature of non-linear simulations for which the ITG mode is dominant. Models of this behaviour have been proposed which involve an interaction between the zonal flows generated by turbulence and the turbulent potential fluctuations [105].

Significantly, it can be seen that even in the non-rotating case the magnitude of the turbulence at late time is substantially suppressed from its initial size at the beginning of the non-linear phase. The toroidal velocity profile shown in figure 6.8a shows a substantial flow shear generated as a results of the profile gradients. It has been well documented that a flow shear in non-linear simulations can reduce and sometimes completely suppress turbulence, and it appears that the diamagnetic shear is here having this effect. This may prove to limit the data we can gain from

later simulations as the inclusion of a solid body rotation may introduce a further stabilising effect.

Ideally, a case with much smaller diamagnetic flows would be used to study the effects of the inertial forces upon transport. A method of reducing the diamagnetic flows in a simulation with a background potential has been implemented within ORB5 already, but the strong-flow modifications are not yet compatible.

6.3.2 Solid body rotating plasma

Figures 6.10a and 6.10b are the parallel momentum and heat fluxes respectively for a simulation with negative toroidal rotation ($v_{tor}/c_{si} = -0.52$). While, figures 6.11a and 6.11b show momentum and heat flux for a simulation with a positive rotation ($v_{tor}/c_{si} = 0.52$).

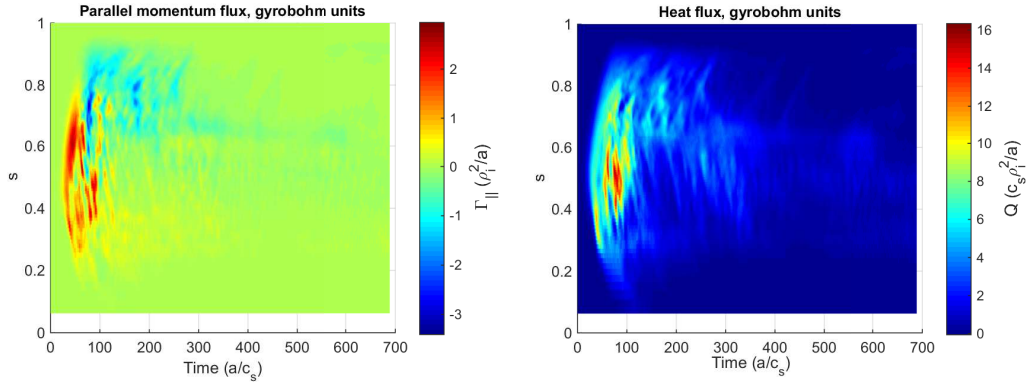

(a) Parallel flux, in gyrobohm units.

(b) Heat flux, in gyrobohm units.

Figure 6.10: Heat and parallel flux for a solid body rotation, corresponding to $v_{tor}/c_{si} = -0.52$.

It can be seen that the toroidal rotation acts to reduce the transport in both cases, but it is apparent that with a negative toroidal rotation rate the turbulence is almost completely suppressed. A likely reason for this asymmetry in toroidal rotation is the already present toroidal velocity in the non-rotating simulation. The flow shear remains in each simulation but the magnitude of the total toroidal velocity differs substantially depending on the direction of applied rotation; a positive rotation acts in opposition to the already present flows. Given that the centrifugal drift is dependent upon the square of the parallel flow (approximately the toroidal flow in a large aspect ratio device), the inertial drifts will be much larger in a negatively rotating simulation.

As the magnitude of measured toroidal velocity, seen in figure 6.8a, has

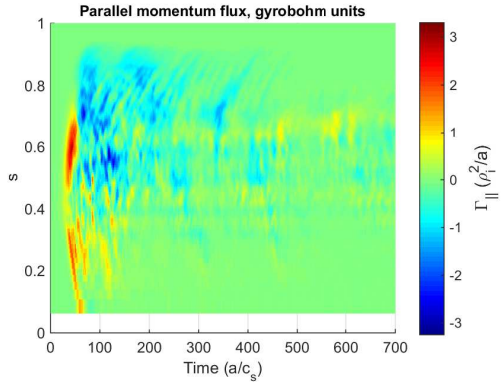

(a) Parallel flux, in gyrobohm units.

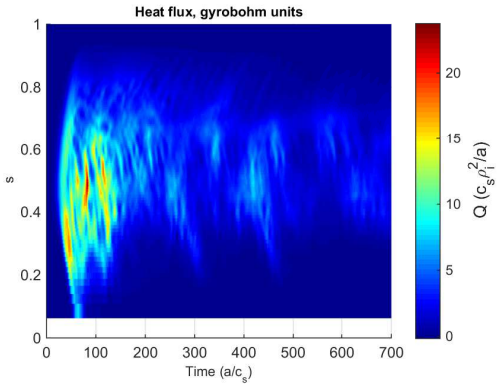

(b) Heat flux, in gyrobohm units.

Figure 6.11: Heat and parallel flux for a solid body rotation, corresponding to $v_{tor}/c_{si} = 0.52$.

little difference between the 'non-rotating' case and the positively rotating case it would be expected that the centrifugal drifts are of a similar size in each simulation. Therefore, the larger flux at earlier time steps followed by a reduced flux at later times may therefore be the result of some unknown non-linear interactions.

The destabilization seen when applying a small toroidal rotation to a linear system, that already has a stabilizing flow shear, does not appear to have been carried over to the non-linear interactions. Little effect from the change of growth rate observed in linear simulations is seen in the late time non-linear results. However, the positively rotating simulation does show larger fluxes than the non-rotating simulations immediately after the linear phase has finished. This may be due to a change in growth rate because of the mode tilting studied in the linear simulations.

6.3.3 Quasi-steady state

After the non-linear simulations have saturated they reach a quasi-steady state were the turbulence of the system remains approximately constant. It is in this phase which we can analyse the turbulent transport properties, taking an average across a finite window of time.

By comparing the toroidal velocity profiles for each simulation at t = 0 and the last time-step we may see the extent of any changes to the flows of the system. In figure 6.12, it is clear that even at late time the flux surface averaged toroidal velocity has undergone only a small change from its initial state. This suggests that the momentum transport in these simulations is small, which is consistent with earlier analysis of linear simulations.

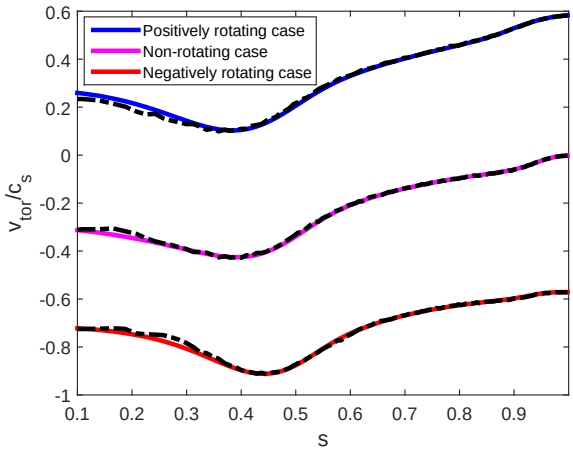

Figure 6.12: The rotation profile for each simulation. The solid line shows the initial toroidal flow profile and the dashed line shows the rotation profile for the same simulation at the last time-step.

The heat flux and diffusivity are of interest as they show the radial transport of energy throughout the system, which is a good measure of turbulence in an ITG dominant simulation, such as those described here. Additionally, as in section 5.7, we are interested in the toroidal momentum flux. An inward Coriolis pinch is still possible and could be significant in increasing the $E \times B$ shear, and subsequently reducing turbulent transport [91].

All quantities discussed in this section are time-averages of the flux surface averaged quantities taken across the last half of the simulation.

The heat diffusivity at late time, figure 6.13, is shown to reduce with increasing positive toroidal rotation, and drop substantially for a negative rotation. There also appears to be a shift in the radial position of peak diffusivity to lower radius under the application of a toroidal rotation.

When comparing strong and weak-flow simulations it appears that the strong-flow modifications add a stabilising effect and reduce the heat diffusivity in simulations. The positively rotating weak-flow case actually shows a higher diffusivity than the non-rotating simulation. However, it is important to note that the positively rotating weak-flow simulation had a smaller S/N ratio than other simulations. Figure 6.13 also shows a large standard deviation for this result.

Figure 6.14 plots the time-averaged parallel momentum flux (which we take as approximately equal to the toroidal momentum flux) normalized against heat flux. It can be seen that if excluding the edges, the non-rotating case has only a small inwards momentum flux. Application of a positive toroidal rotation appears

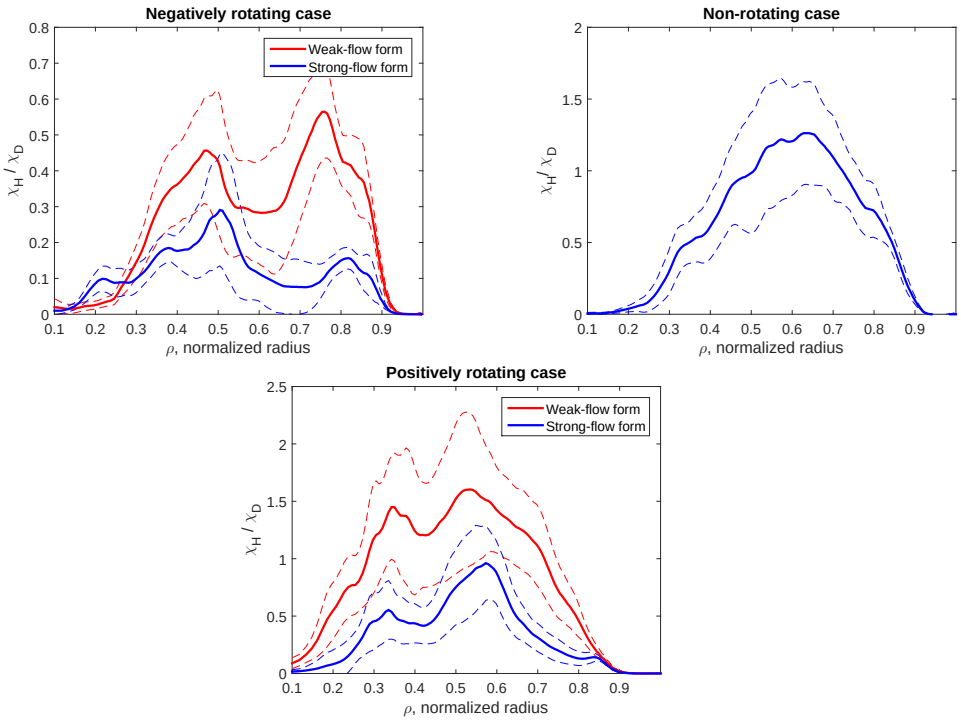

Figure 6.13: Flux-surface averaged ion heat diffusivity in units of $\chi_D = c_s \rho_i^2 / L_n$, and time-averaged across the last half of the simulation. The solid line shows the time-averaged value and the dashed lines show a change of one standard deviation in each direction from the mean.

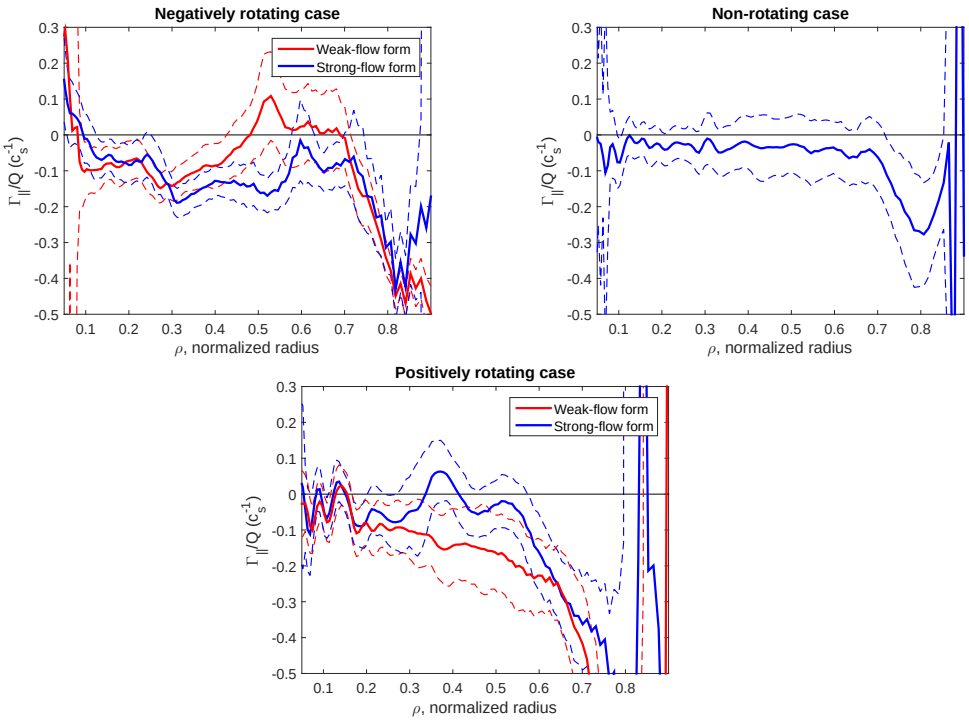

Figure 6.14: Late time averages of parallel momentum flux (normalized with heat flux) as a radial function. The solid line shows the time-averaged value and the dashed lines show a change of one standard deviation in each direction from the mean.

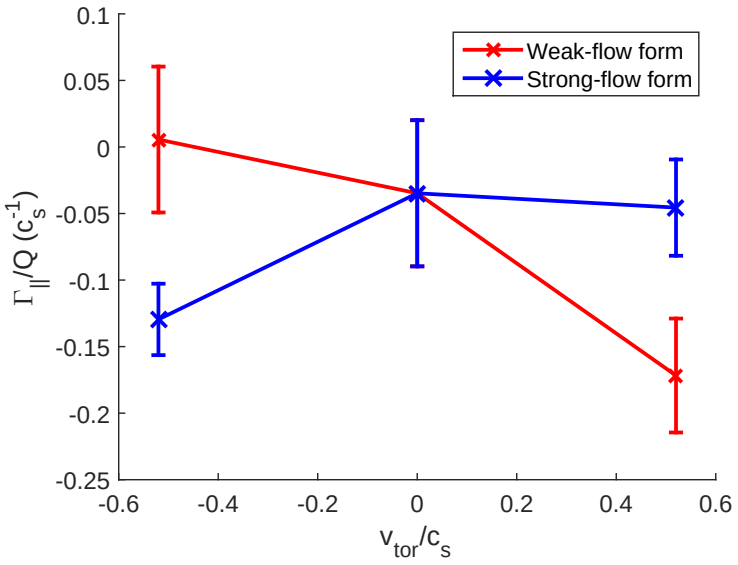

Figure 6.15: Time averaged parallel momentum flux (normalized with heat flux) averaged across a radial window of width centred around r = 0.5a and of width 0.2a plotted as a function of v_{tor}. The error bars indicate one standard deviation for each data point.

to lead to a generally larger (though still small) inwards pinch effect but has a region around $\rho \sim 0.57$ which spikes into a positive flux. The reason for this is not immediately apparent, but it does occur at roughly the same radius as the peak heat diffusivity for this case.

A negative rotation rate is shown to lead to a stronger pinch effect in general than the non-rotating case and has a substantial radial width which has greatly increased inwards momentum flux.

In figure 6.15, the flux-surface averaged momentum flux across the region $r = (0.4 \text{ to } 0.6)$ is plotted as a function of the applied toroidal velocity for the simulation. Comparing this to the linear case, figure 5.11b, we see a size-ably smaller pinch in the non-linear simulations. Additionally, there is a noticeable increase in the asymmetry of pinch with toroidal velocity. At least part of this can be accounted for by the large flows generated from the profile gradients. The actual toroidal velocity at mid-radius, figure 6.8a, is substantially smaller for the positive rotation case than the negative rotation case and when considering the standard deviation of the results the positive rotation case is not different enough from the 'non-rotating' case to allow us to state a difference with any real confidence.

It is difficult to make judgements of the difference between weak and strong-

flow formalisms in regards to figure 5.11b, as the fluxes are small and therefore $\Gamma_{||}/Q$ is likely sensitive to small variations. Despite the substantial change seen in figure 6.8a, between the weak and strong-flow results, we cannot make definitive conclusions. In fact, the deviation seems to suggest that all of these non-linear simulations may be extremely sensitive to small changes in simulations.

Given the low levels of transport, it is also worth noting that fluctuations seen in figure 6.14 may actually be the result of otherwise small fluctuations of flux, and as such it is difficult to make firm conclusions.

6.3.4 Energy Spectrum

Figures 6.16a, 6.16b and 6.16c show the energy spectrum of several toroidal modes in the simulations with negative rotation, no rotation and positive toroidal rotation respectively. Differences in the linear phase of the simulation appear to be minor, but it can be seen that there is a significant drop in the energy of modes in the negative rotation case when compared to the non-rotating case. The lower n modes also show an energy loss in the positive rotation case. This suggests the inertial terms in a solid body rotation act to suppress toroidal modes with low n more than high n modes.

The saturation level of the zonal flows in the rotating cases appear to be approximately three times larger than in the non-rotating case. This suggests that the zonal flows have an increased stabilising effect when a solid body rotation is added to the simulations.

6.4 Summary

This chapter has begun by performing a fine-tuning of the noise control and heating parameters, so that we can be confident that they are still working as intended. This also allows us to be certain that the S/N ratio of our non-linear simulations is as good as possible.

A series of non-linear simulations are then performed which apply solid body rotations to a system with parameters matching the CYCLONE case. A stabilizing influence did seem to be present regardless of the sign of rotation rate, but it was found that a negatively rotating plasma has a far greater stabilising effect than a positively rotating plasma. However, transport was found to already be low even before rotations were added due to the flows arising from the profile gradients. It appears the destabilizing effect which occurs when applying a small toroidal rotation

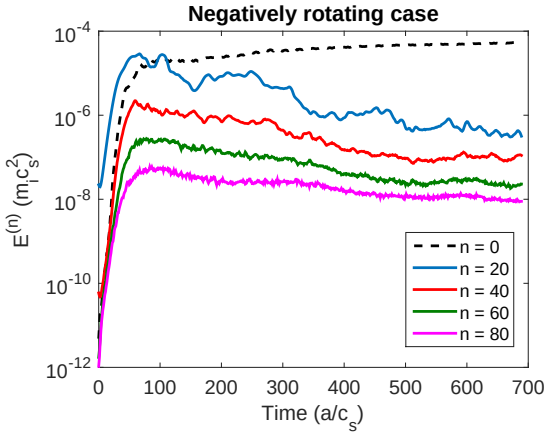

(a) Energy spectrum for a plasma rotating in the negative toroidal direction.

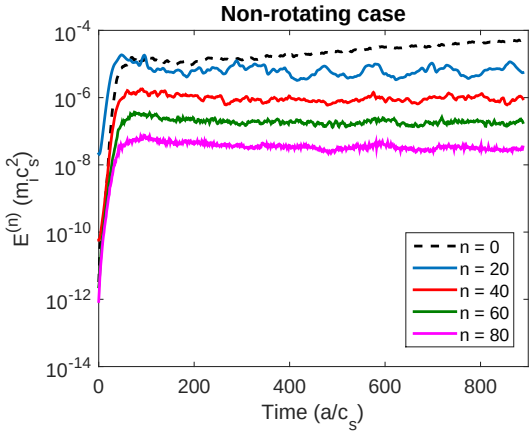

(b) Energy spectrum for a non-rotating plasma.

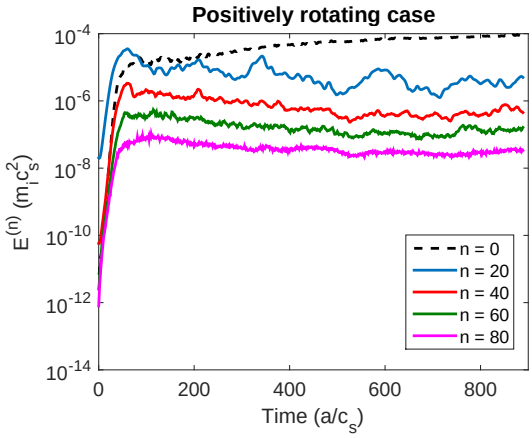

(c) Energy spectrum for a plasma rotating in the positive toroidal direction.

Figure 6.16: The electric field-energy spectra of the zonal flow (n=0) and toroidal modes n=20,40,60 and 80 for different rotation rates.

to a system already that is stabilized by a flow shear is not carried over to the non-linear interactions.

Chapter 7

Conclusion

In the past, the rotation of a plasma had not been a subject of particular interest in tokamak physics and strongly rotating plasma were not consistent with the gyrokinetic models used for turbulence studies. However, it is now believed that plasma rotation can have a stabilizing effect on tokamaks and while many studies of the effects of a radial electric shear have been performed, the physics of the inertial forces which arise from a plasma rotation are less well explored. As such, the aim of this thesis has been to investigate the behaviour of a tokamak with a plasma that is rotating toroidally at velocities approaching the ion thermal velocity. Previous simulations of rotating plasmas have used local gyrokinetic codes, but simulations performed as part of this thesis were run in the global gyrokinetic code ORB5.

To this end, ORB5 has been extended to allow for strong-flows; the changes made are largely detailed in chapter 3. This process involved modifications of the gyrokinetic equations used within ORB5 to match those discussed in chapter 2 and was followed by modifications of the equilibrium distribution function of ORB5. Modifications to the equilibrium distribution function were made to ensure that the simulations remains in an approximately gyrokinetic equilibrium, even under high levels of toroidal rotation. A density correction was added so that the equilibrium profiles would more closely match the inputs but the poloidal variation introduced to the density was retained.

7.1 Summary of Results

Some basic testing was performed to ensure that ORB5 still worked as intended, and that the newly defined equilibrium distribution function gave equilibrium profiles which remained reasonably close to the inputs. Following this, studies were per-

formed in chapter 4 which investigate the possibility of Geodesic Acoustic Modes taking the form of radial eigenmodes in a tokamak. It was found that the dependence of GAM frequency on radial wavenumber k_r was poorly behaved in simulations for which k_r was not close to zero. However, despite this, the predicted eigenfunctions were found within the simulations. This showed that not only is ORB5 capable of recreating the bands of frequency which have shown experimentally, but demonstrates that the predictions as made by Itoh [75] are valid in a global simulation.

The first investigations of toroidal rotating plasmas studied the change of GAM frequency with both a positive and negative toroidal rotation. Although results did not entirely match predictions, the analytical theory still provided a good match. Predictions were seen to overestimate the change of frequency with v_{tor} and so gave a poorer match as the toroidal Mach number approached unity. The symmetrical nature of frequency change, with dependence upon the magnitude of v_{tor} and not the direction, were also matched in results from later linear studies. Worth noting is that reults suggest that the density correction term had a sizable impact on the GAM frequency, while the other modifications made had a much smaller impact.

Attempts were made to investigate the damping of GAMs in a rotating system, but a poor trend was observed at best. It is possible that the GAMs became more weakly damped as rotation rate increased, but our data is not detailed enough to make firm conclusions. Previous simulations performed within ORB5 have suggested that recovery of the damping rate of a GAM requires a much higher number of markers in simulations than those needed to recover the GAM frequency. As such, future investigations which may be performed will likely require more computationally intensive simulations.

Linear simulations in chapter 5 found that the gyrokinetic model derived in a co-moving frame gave good predictions of the frequency variation with toroidal rotation for non-zero toroidal modes. Similarly to observation of GAM frequency, the direction of rotation was not found to be an important feature in regards to the mode frequency. However, although the centrifugal and Coriolis terms did largely appear to behave in a similar way to local codes, it was found that these terms acted in opposition to the stabilising effects of a diamagnetic shear. Once the mode structures were un-tilted, further increases to toroidal velocity showed a stabilizing influence. This feature would only appear in a global simulation and it therefore highlights the importance of further investigations into the effects of toroidal rotation in a global system as well as local. Similar changes between the weak and strong-flow forms of ORB5 were observed for these linear studies as were observed with the

GAM simulations.

Although the prediction made in a co-moving frame suggested an inwards toroidal momentum pinch caused by the Coriolis force, later studies suggested that the effect of this would be small when using adiabatic electrons. A momentum pinch, which increased inwardly with increasing toroidal rotation was seen in linear results, but it did not appear to be an important mechanism. Since the predictions were made from a gyro-fluid model it is not unlikely that some pinch may still form from effects that were not accounted for. Though, it was found that the tilting of the modes matched closely with changes to the linear mode growth rates. Despite the actual tilting of the modes remaining roughly symmetric (angle of negative rotating plasma matching positively rotating case), the change in growth rate did depend on rotation direction. A suggested cause of this asymmetry was the radial length of the mode structures, which was observed to grow for a negatively rotating simulation.

Non-linear simulations in chapter 6 seemed to contain a large flow shear even before a toroidal rotation was applied, which acted to keep transport in simulations low. Despite this, it was observed that toroidal rotations did have a stabilising effect upon turbulence. There was an asymmetry observed in the reduction of transport with the direction of rotation. When the plasma was given a negative toroidal rotation (in the same direction as the already present flows), the turbulence was found to exhibit a much stronger reduction and was almost completely suppressed.

These results suggest that the strong-flow terms may be able to offer some insight in future research of tokamak confinement. Although the benefit of applying a strong flow to a tokamak may not surpass those from of the application of a sheared electric field, it still contains noticeable effects upon the behaviour of transport in even a large aspect ratio device; as studied in this thesis. As such, these inertial terms will likely be large enough that they cannot be neglected when studying turbulent transport.

7.2 Future Work

As the work in this thesis has introduced the strong-flow terms to ORB5 there are numerous further investigations that may now be performed.

Simulations which were performed for this thesis have all used adiabatic electrons. However, the Coriolis pinch effect found in the local co-moving model is not expected to appear in any substantial form unless kinetic electrons are included in simulations [93]. Therefore, simulations that include kinetic electrons could show a larger flow shear forming from an inwards toroidal momentum pinch that was not

reflected in our simulations.

The work covered in this thesis has performed collisionless non-linear simulations but the capability for collisional studies exists within ORB5. As a toroidal rotation has been shown to have a stabilizing effect on turbulence it would be a useful study to investigate how this behaviour responds to collisional simulations. There should be minimal changes required to the collisional components of ORB5 to successfully integrate with the strong-flow terms introduced in this thesis.

Another point of high interest would be strong-flow simulations for MAST-like parameters. Previous work has been done with ORB5 investigating the effect of flows in MAST, but these were performed at a time when large toroidal flows were not accurately modelled within simulations [19, 103, 106]. Within a spherical tokamak, the poloidal component of the magnetic field is significantly larger, and therefore any contributions from $\mathbf{u}_E$ also have an increased importance. Combined with the larger flows that have been observed experimentally, investigations which contain these strong-flow terms could be a point of high interest [32].

Aside from improvements to the conservation, investigations that include a poloidally varying background potential could also be a worthwhile point of study. The background potential has been intentionally treated in the strong-flow modifications so as to allow a radially and poloidally varying background electric potential, which would closer match those that may be observed experimentally.

Appendix A

Abbreviations

Contained in the table below is a list of abbreviations and mathematical symbols that have been used in this thesis. The list is by no means exhaustive, notations used in only a small section (for example) have not been defined here.

Symbol	Description
a	Minor radius of last closed flux surface
$\mathbf{A}$	Magnetic Vector Potential
$\mathbf{b}$	Magnetic field unit vector
$\mathbf{B}$	Magnetic field vector
c_s	Ion sound speed
e	Elementary charge
$\mathbf{E}$	Electric field vector
f	Distribution Function
f_0	Equilibrium distribution function
δf	Perturbed distribution function
$\mathbf{J}$	Plasma current vector
k_x	Mode wavenumber (component in x-direction)
L_T, L_n	Temperature and density gradient length scales
m	Poloidal mode number/ Particle mass
M	Million (when placed after a number)
n	Toroidal mode number / Particle density
n_s	Density of species s
n_0	Density at ρ_{peak}
δn_i	Perturbed ion density
N	Marker number
q	Safety factor/ Particle electric charge
Q	Heat flux

Symbol	Description
r	Minor radius of plasma
R	Major radius of plasma
$\mathbf{R}$	Gyro-centre (guiding centre) position vector
R_0	Major radius at magnetic axis
s	Radial coordinate
S/N	Signal to noise
t	Time
T	Temperature
T_0	Temperature at ρ_{peak}
u_E	$E \times B$ velocity
v	Velocity
$v_{\parallel}$	Velocity parallel to magnetic field
$v_{\perp}$	Velocity perpindicular to magnetic field
v_{Ti}	Ion thermal velocity
w	Particle weight
$\mathbf{x}$	Particle position vector
α	Gyro-phase angle
β	Plasma β
γ	Growth rate/ Damping rate of mode
Γ	Adiabatic index
$\Gamma_{\parallel}$	Parallel momentum flux
ϵ	Small parameter/ Particle energy
τ_e	The ratio of electron to ion temperature
θ	Poloidal angle
θ_*	Straight-field line poloidal angle
ρ	Normalized radius, r/a
$\boldsymbol{\rho}$	Charge density
ρ_i	Ion gyro-radius
ρ_*	Normalized gyro-radius
ρ_{peak}	Radial position at which gradient profiles peak. Profiles are also normalized against value at this position.
ϕ	Electric potential
Φ	Background electric potential
$\delta\phi$	Perturbed electric potential
ψ	Poloidal flux
ψ_c	Toroidal canonical momentum
χ	Tilting angle
χ_H	Heat diffusivity
Ω_{ci}	Ion cyclotron frequency

Appendix B

Derivation of Toroidal Rotation Rate

The toroidal rotation rate is given by the toroidal component of the drift velocities.

$$\Omega_t = \mathbf{v} \cdot \boldsymbol{\nabla}\zeta = (\mathbf{u_E} + v_0\mathbf{b}) \cdot \boldsymbol{\nabla}\zeta \tag{B.1}$$

where u_E is the $E \times B$ drift and v_0 is the parallel flow velocity, as given in equation 3.37. This equation can be expanded by substituting for the velocities with equations 3.10 and 3.37.

$$\Omega_t = \left(\frac{\partial\phi}{\partial\psi}\right)\left[\left\{-F\left(\boldsymbol{\nabla}\psi \times \boldsymbol{\nabla}\zeta\right) + |\nabla\psi|^2\boldsymbol{\nabla}\zeta\right\} + \frac{F}{B}\mathbf{b}\right] \cdot \boldsymbol{\nabla}\zeta \tag{B.2}$$

and can then be simplified to give the more useful form of

$$\Omega_t = \left(\frac{\partial\phi}{\partial\psi}\right)\left\{\frac{|\nabla\psi|^2}{R^2B^2} + \frac{F^2}{R^2B^2}\right\} = \left(\frac{\partial\phi}{\partial\psi}\right). \tag{B.3}$$

Therefore, the toroidal rotation rate in a tokamak is equal to the derivative of the background potential with respect to the poloidal flux function.

Additionally, it has been previously stated that the poloidal contributions from the parallel and background $E \times B$ flows cancel with each other. This can be checked by taking the poloidal component of each flow

$$\mathbf{u_E} \cdot \boldsymbol{\nabla}\theta_* = \frac{1}{B^2}\left(\frac{\partial\phi}{\partial\psi}\right)\left[-F\boldsymbol{\nabla}\theta_* \cdot \left(\boldsymbol{\nabla}\psi \times \boldsymbol{\nabla}\zeta\right) + |\nabla\psi|^2\boldsymbol{\nabla}\zeta \cdot \boldsymbol{\nabla}\theta_*\right] \tag{B.4}$$

which simplifies to

$$\mathbf{u_E} \cdot \boldsymbol{\nabla}\theta_* = -\frac{F}{B^2}\left(\frac{\partial \phi}{\partial \psi}\right)\boldsymbol{\nabla}\theta_* \cdot (\boldsymbol{\nabla}\psi \times \boldsymbol{\nabla}\zeta)\,. \tag{B.5}$$

The poloidal component of parallel flow is given by

$$v_0 \mathbf{b} \cdot \boldsymbol{\nabla}\theta_* = \frac{v_0}{B}\left(F\boldsymbol{\nabla}\zeta + \boldsymbol{\nabla}\psi \times \boldsymbol{\nabla}\zeta\right) \cdot \boldsymbol{\nabla}\theta_* = \frac{v_0}{B}\boldsymbol{\nabla}\theta_* \cdot (\boldsymbol{\nabla}\psi \times \boldsymbol{\nabla}\zeta)\,. \tag{B.6}$$

By taking the sum of equation B.5 and B.6, the total remaining poloidal velocity is found to be zero.

$$\mathbf{v} \cdot \boldsymbol{\nabla}\theta_* = (\mathbf{u_E} + v_0\mathbf{b}) \cdot \boldsymbol{\nabla}\theta_* = \left(\frac{\partial \phi}{\partial \psi}\right)\left[-\frac{F}{B^2} + \frac{F}{B^2}\right]\{\boldsymbol{\nabla}\theta_* \cdot (\boldsymbol{\nabla}\psi \times \boldsymbol{\nabla}\zeta)\} = 0 \tag{B.7}$$

Appendix C

Full expansion of the equations of motion

Continuing on from section 3.12.1, the curl of the background $\mathbf{E}\times\mathbf{B}$ drift is calculated as

$$\boldsymbol{\nabla}\times\mathbf{u}_E = J_{\theta_*,s,\zeta}\left[-\left(\frac{[\boldsymbol{\nabla}s\cdot\boldsymbol{\nabla}\theta_*]}{R^2}\frac{\partial u_\zeta}{\partial s}+\frac{|\nabla\theta|^2}{R^2}\frac{\partial u_\zeta}{\partial\theta_*}\right)\boldsymbol{\nabla}s+\left(\frac{|\nabla s|^2}{R^2}\frac{\partial u_\zeta}{\partial s}+\frac{[\boldsymbol{\nabla}s\cdot\boldsymbol{\nabla}\theta_*]}{R^2}\frac{\partial u_\zeta}{\partial\theta_*}\right)\boldsymbol{\nabla}\theta_*+\left(|\nabla s|^2|\nabla\theta_*|^2-[\boldsymbol{\nabla}s\cdot\boldsymbol{\nabla}\theta_*]^2\right)\left(\frac{\partial u_s}{\partial\theta_*}-\frac{\partial u_{\theta_*}}{\partial s}\right)\boldsymbol{\nabla}\zeta\right]. \tag{C.1}$$

To simplify further equations, the curl of u_E can be defined

$$\boldsymbol{\nabla}\times\mathbf{u}_E = X\mathbf{e}_s + Y\mathbf{e}_{\theta_*} + Z\mathbf{e}_\zeta \tag{C.2}$$

where X, Y and Z are

$$X = \boldsymbol{\nabla}s\cdot(\boldsymbol{\nabla}\times\mathbf{u}_E) = -\frac{1}{J_{\theta_* s\zeta}}\frac{\partial u_\zeta}{\partial\theta_*} \tag{C.3}$$

$$Y = \boldsymbol{\nabla}\theta_*\cdot(\boldsymbol{\nabla}\times\mathbf{u}_E) = \frac{1}{J_{\theta_* s\zeta}}\frac{\partial u_\zeta}{\partial s} \tag{C.4}$$

$$Z = \boldsymbol{\nabla}\zeta\cdot(\boldsymbol{\nabla}\times\mathbf{u}_E) = \frac{1}{J_{\theta_* s\zeta}}\left(\frac{\partial u_s}{\partial\theta_*}-\frac{\partial u_{\theta_*}}{\partial s}\right). \tag{C.5}$$

The parallel component of equation C.2 is then given by

$$\mathbf{b}\cdot(\boldsymbol{\nabla}\times\mathbf{u}_E) = \frac{F(\psi)}{BR^2}Z + \frac{1}{BJ_{\theta_*\psi\zeta}}Y. \tag{C.6}$$

which is used in the calculation of $B^*_{\parallel}$.

To find the perpendicular component, the cross product of $\mathbf{B}$ with equation C.2 is calculated

$$\begin{aligned}\mathbf{B}\times(\boldsymbol{\nabla}\times\mathbf{u_E}) = FX\left(\boldsymbol{\nabla}\zeta\times\boldsymbol{\nabla}s\right) + FY\left(\boldsymbol{\nabla}\zeta\times\boldsymbol{\nabla}\theta_*\right) + \\ \left(\boldsymbol{\nabla}\psi\cdot\boldsymbol{\nabla}s\right)X\boldsymbol{\nabla}\zeta + \left(\boldsymbol{\nabla}\psi\cdot\boldsymbol{\nabla}\theta_*\right)Y\boldsymbol{\nabla}\zeta - \frac{Z}{R^2}\boldsymbol{\nabla}\psi\end{aligned} \tag{C.7}$$

which is followed by a second cross product with $\mathbf{B}$ and division by B^2.

$$\begin{aligned}\mathbf{b}\times[\mathbf{b}\times(\boldsymbol{\nabla}\times\mathbf{u}_E)] = -\frac{F^2}{B^2R^2}X\boldsymbol{\nabla}s - \frac{1}{B^2R^2}\left(\left[\boldsymbol{\nabla}s\cdot\boldsymbol{\nabla}\psi\right]X + \left[\boldsymbol{\nabla}\theta_*\cdot\boldsymbol{\nabla}\psi\right]Y\right)\boldsymbol{\nabla}\psi \\ - \frac{F^2}{B^2R^2}Y\boldsymbol{\nabla}\theta_* - \frac{F}{B^2R^2}Z\left(\boldsymbol{\nabla}\zeta\times\boldsymbol{\nabla}\psi\right) + \left(\frac{F}{B^2J_{\theta_*\psi\zeta}}Y \right. \\ \left. -\frac{|\nabla\psi|^2}{B^2R^2}Z\right)\boldsymbol{\nabla}\zeta\end{aligned} \tag{C.8}$$

The components of which are

$$\begin{aligned}\{\mathbf{b}\times[\mathbf{b}\times(\boldsymbol{\nabla}\times\mathbf{u}_E)]\}\cdot\boldsymbol{\nabla}s = -\frac{1}{B^2R^2}\left\{F^2\left(|\nabla s|^2X + \left[\boldsymbol{\nabla}s\cdot\boldsymbol{\nabla}\theta_*\right]Y\right)\right. \\ \left. + \left(\boldsymbol{\nabla}s\cdot\boldsymbol{\nabla}\psi\right)\left(\left[\boldsymbol{\nabla}s\cdot\boldsymbol{\nabla}\psi\right]X + \left[\boldsymbol{\nabla}\psi\cdot\boldsymbol{\nabla}\theta_*\right]Y\right)\right\}\end{aligned} \tag{C.9}$$

$$\begin{aligned}\{\mathbf{b}\times[\mathbf{b}\times(\boldsymbol{\nabla}\times\mathbf{u}_E)]\}\cdot\boldsymbol{\nabla}\theta_* = -\frac{1}{B^2R^2}\left\{F^2\left(\left[\boldsymbol{\nabla}s\cdot\boldsymbol{\nabla}\theta_*\right]X + |\nabla\theta_*|^2Y\right)\right. \\ + \left(\boldsymbol{\nabla}\psi\cdot\boldsymbol{\nabla}\theta_*\right)\left(\left[\boldsymbol{\nabla}s\cdot\boldsymbol{\nabla}\psi\right]X + \left[\boldsymbol{\nabla}\psi\cdot\boldsymbol{\nabla}\theta_*\right]Y\right) \\ \left. -\frac{F}{J_{\theta_*\psi\zeta}}Z\right\}\end{aligned} \tag{C.10}$$

$$\{\mathbf{b}\times[\mathbf{b}\times(\boldsymbol{\nabla}\times\mathbf{u}_E)]\}\cdot\boldsymbol{\nabla}\zeta = \frac{1}{B^2R^2}\left\{\frac{F}{J_{\theta_*\psi\zeta}}Y - \frac{|\nabla\psi|^2}{R^2}Z\right\} \tag{C.11}$$

and used in the equations of motion in ORB5 as discussed in section 3.12.1.

Bibliography

[1] Bert Metz and Ogunlade R Davidson. *Climate change 2007: Mitigation: Contribution of working group III to the fourth assessment report of the intergovernmental panel on climate change.* Intergovernmental Panel on Climate Change, 2007.

[2] Thomas F Stocker, Dahe Qin, Gian-Kasper Plattner, M Tignor, Simon K Allen, Judith Boschung, Alexander Nauels, Yu Xia, Vincent Bex, and Pauline M Midgley. Climate change 2013: The physical science basis. *Intergovernmental Panel on Climate Change, Working Group I Contribution to the IPCC Fifth Assessment Report (AR5)(Cambridge Univ Press, New York)*, 2013.

[3] Virginia Sonntag-O'Brien Ulf Moslener Christine Grning Angus McCrone, Eric Usher. *Global trends in renewable energy investment 2014.* Frankfurt School of Finance and Management, 2014.

[4] J Ongena and G Van Oost. Energy for future centuries. *Transactions of fusion science and technology*, 41:3–14, 2002.

[5] Vitalii D Shafranov, BD Bondarenko, German A Goncharov, Oleg A Lavrentev, Andrei D Sakharov, et al. On the history of the research into controlled thermonuclear fusion. *Physics-Uspekhi*, 44(8):835–843, 2001.

[6] R Aymar, P Barabaschi, and Y Shimomura. The iter design. *Plasma Physics and Controlled Fusion*, 44(5):519, 2002.

[7] P-H Rebut et al. Iter: the first experimental fusion reactor. *Fusion engineering and design*, 30(1):85–118, 1995.

[8] Satoshi Konishi, Satoshi Nishio, Kenji Tobita, and DEMO The. Demo plant design beyond iter. *Fusion engineering and design*, 63:11–17, 2002.

[9] John S Lilley. *Nuclear physics: principles and applications*. John Wiley & Sons, 2009.

[10] John D Lawson. Some criteria for a power producing thermonuclear reactor. *Proceedings of the Physical Society. Section B*, 70(1):6, 1957.

[11] Denis Keefe. Inertial confinement fusion. *Annual Review of Nuclear and Particle Science*, 32(1):391–441, 1982.

[12] George H Miller, Edward I Moses, and Craig R Wuest. The national ignition facility. *Optical Engineering*, 43(12):2841–2853, 2004.

[13] Francis F. Chen. *Introduction of Plasma Physics and Controlled Fusion Volume 1: Plasma Physics*. Plenium Press, second edition, 1990.

[14] William D D'haeseleer, William Nicholas Guy Hitchon, JL Shohet, JD Callen, and DW Kerst. Flux coordinates and magnetic field structure. a guide to a fundamental tool of plasma theory. 1991.

[15] FL Hinton and RD Hazeltine. Theory of plasma transport in toroidal confinement systems. *Reviews of Modern Physics*, 48(2):239, 1976.

[16] AJ Wootton, BA Carreras, H Matsumoto, K McGuire, WA Peebles, Ch P Ritz, PW Terry, and SJ Zweben. Fluctuations and anomalous transport in tokamaks. *Physics of Fluids B: Plasma Physics (1989-1993)*, 2(12):2879–2903, 1990.

[17] W Horton. Drift waves and transport. *Reviews of Modern Physics*, 71(3):735, 1999.

[18] Steven C Cowley, RM Kulsrud, and R Sudan. Considerations of ion-temperature-gradient-driven turbulence. *Physics of Fluids B: Plasma Physics (1989-1993)*, 3(10):2767–2782, 1991.

[19] Peter Hill. *The effect of toroidal flows on the stability of ITGs in MAST*. PhD thesis, University of Warwick, 2012.

[20] PH Diamond, SI Itoh, K Itoh, and TS Hahm. Plasma phys. control. fusion 47. *R35*, 2, 2005.

[21] Kimitaka Itoh, S-I Itoh, PH Diamond, A Fujisawa, Y Nagashima, M Yagi, A Fukuyama, TS Hahm, K Hallatschek, and GR Tynan. Physics of zonal flows. In *TURBULENT TRANSPORT IN FUSION PLASMAS: First ITER*

International Summer School, volume 1013, pages 106–126. AIP Publishing, 2008.

[22] T. S. Hahm. Nonlinear gyrokinetic equations for tokamak microturbulence. *Physics of Fluids*, 31(9):2670, 1988.

[23] T. S. Hahm. Nonlinear gyrokinetic equations for turbulence in core transport barriers. *Physics of Plasmas*, 3(12):4658, 1996.

[24] John G Kirkwood. The statistical mechanical theory of transport processes i. general theory. *The Journal of Chemical Physics*, 14(3):180–201, 1946.

[25] MHA Hassan. Plasma kinetic equations. *TRIESTE COURSE*, page 47, 1981.

[26] John Wesson. *Tokamaks*. Oxford University Press, third edition, 2004.

[27] EA Frieman and Liu Chen. Nonlinear gyrokinetic equations for low-frequency electromagnetic waves in general plasma equilibria. *Physics of Fluids*, (25):502–508, 1982.

[28] John E Rice. Spontaneous rotation and momentum transport in tokamak plasmas. In *Journal of Physics: Conference Series*, volume 123, page 012003. IOP Publishing, 2008.

[29] YB Kim, PH Diamond, and RJ Groebner. Neoclassical poloidal and toroidal rotation in tokamaks. *Physics of Fluids B: Plasma Physics (1989-1993)*, 3(8):2050–2060, 1991.

[30] RC Morris, MG Haines, and RJ Hastie. The neoclassical theory of poloidal flow damping in a tokamak. *Physics of Plasmas (1994-present)*, 3(12):4513–4520, 1996.

[31] Peter C de Vries, M-D Hua, DC McDonald, C Giroud, M Janvier, MF Johnson, T Tala, K-D Zastrow, and JET EFDA Contributors. Scaling of rotation and momentum confinement in jet plasmas. *Nuclear Fusion*, 48(6):065006, 2008.

[32] RJ Akers, JW Ahn, GY Antar, LC Appel, D Applegate, C Brickley, C Bunting, PG Carolan, CD Challis, NJ Conway, et al. Transport and confinement in the mega ampere spherical tokamak (mast) plasma. *Plasma physics and controlled fusion*, 45(12A):A175, 2003.

[33] AG Peeters, Clemente Angioni, A Bortolon, Y Camenen, Francis James Casson, Basil Duval, L Fiederspiel, WA Hornsby, Yasuhiro Idomura, T Hein, et al.

Overview of toroidal momentum transport. *Nuclear Fusion*, 51(9):094027, 2011.

[34] A. G. Peeters, D. Strintzi, Y. Camenen, C. Angioni, F. J. Casson, W. A. Hornsby, and A. P. Snodin. Influence of the centrifugal force and parallel dynamics on the toroidal momentum transport due to small scale turbulence in a tokamak. *Physics of Plasmas*, 16(4):042310, 2009.

[35] Francis James Casson, AG Peeters, C Angioni, Y Camenen, WA Hornsby, AP Snodin, and G Szepesi. Gyrokinetic simulations including the centrifugal force in a rotating tokamak plasma. *Physics of Plasmas (1994-present)*, 17(10):102305, 2010.

[36] Francis James Casson. *Turbulent transport in rotating tokamak plasmas*. PhD thesis, University of Warwick, 2011.

[37] AJ Brizard and TS Hahm. Foundations of nonlinear gyrokinetic theory. *Reviews of modern physics*, 79(2):421, 2007.

[38] RJ Fonck, G Cosby, RD Durst, SF Paul, N Bretz, S Scott, E Synakowski, and G Taylor. Long-wavelength density turbulence in the tftr tokamak. *Physical review letters*, 70(24):3736, 1993.

[39] Robert G Littlejohn. Hamiltonian formulation of guiding center motion. *Physics of Fluids (1958-1988)*, 24(9):1730–1749, 1981.

[40] John R Cary and Robert G Littlejohn. Noncanonical hamiltonian mechanics and its application to magnetic field line flow. *Annals of Physics*, 151(1):1–34, 1983.

[41] A Brizard. Nonlinear gyrokinetic maxwell-vlasov equations using magnetic co-ordinates. *Journal of plasma physics*, 41(03):541–559, 1989.

[42] Alain J Brizard. Nonlinear gyrokinetic vlasov equation for toroidally rotating axisymmetric tokamaks. *Physics of Plasmas (1994-present)*, 2(2):459–471, 1995.

[43] Robert G Littlejohn. Variational principles of guiding centre motion. *Journal of Plasma Physics*, 29(01):111–125, 1983.

[44] P. Angelino, A. Bottino, R. Hatzky, S. Jolliet, O. Sauter, T. M. Tran, and L. Villard. On the definition of a kinetic equilibrium in global gyrokinetic simulations. *Physics of Plasmas*, 13(5):052304, 2006.

[45] Simon J Allfrey and R Hatzky. A revised δf algorithm for nonlinear pic simulation. *Computer physics communications*, 154(2):98–104, 2003.

[46] S Jolliet, Alberto Bottino, P Angelino, Roman Hatzky, TM Tran, BF McMillan, O Sauter, K Appert, Yasuhiro Idomura, and Laurent Villard. A global collisionless pic code in magnetic coordinates. *Computer Physics Communications*, 177(5):409–425, 2007.

[47] J Candy and RE Waltz. An eulerian gyrokinetic-maxwell solver. *Journal of Computational Physics*, 186(2):545–581, 2003.

[48] Mike Kotschenreuther, G Rewoldt, and WM Tang. Comparison of initial value and eigenvalue codes for kinetic toroidal plasma instabilities. *Computer Physics Communications*, 88(2):128–140, 1995.

[49] Charles K Birdsall and A Bruce Langdon. *Plasma physics via computer simulation*. CRC Press, 2004.

[50] John M Dawson. Particle simulation of plasmas. *Reviews of Modern Physics*, 55(2):403, 1983.

[51] David Tskhakaya. The particle-in-cell method. In *Computational Many-Particle Physics*, pages 161–189. Springer, 2008.

[52] J Candy, RE Waltz, and W Dorland. The local limit of global gyrokinetic simulations. *Physics of Plasmas*, 11(5):L25, 2004.

[53] Hinrich Lütjens, Anders Bondeson, and Olivier Sauter. The chease code for toroidal mhd equilibria. *Computer physics communications*, 97(3):219–260, 1996.

[54] L Guazzotto, R Betti, J Manickam, and S Kaye. Numerical study of tokamak equilibria with arbitrary flow. *Physics of Plasmas (1994-present)*, 11(2):604–614, 2004.

[55] MPI Forum. MPI: A Message-Passing Interface Standard (Version 1.1), 1995. Technical Report, URL: http://www.mpi-forum.org.

[56] Charlson C Kim and Scott E Parker. Massively parallel three-dimensional toroidal gyrokinetic flux-tube turbulence simulation. *Journal of Computational Physics*, 161(2):589–604, 2000.

[57] Mathieu Fivaz, S Brunner, G De Ridder, O Sauter, TM Tran, J Vaclavik, L Villard, and K Appert. Finite element approach to global gyrokinetic particle-in-cell simulations using magnetic coordinates. *Computer physics communications*, 111(1):27–47, 1998.

[58] Klaus Höllig. *Finite element methods with B-splines*, volume 26. Siam, 2003.

[59] Sébastien Jolliet. Gyrokinetic particle-in-cell global simulations of ion-temperature-gradient and collisionless-trapped-electron-mode turbulence in tokamaks. 2009.

[60] Edward Anderson, Zhaojun Bai, Christian Bischof, Susan Blackford, James Demmel, Jack Dongarra, Jeremy Du Croz, Anne Greenbaum, S Hammerling, Alan McKenney, et al. *LAPACK Users' guide*, volume 9. Siam, 1999.

[61] L Susan Blackford, Jaeyoung Choi, Andy Cleary, Eduardo D'Azevedo, James Demmel, Inderjit Dhillon, Jack Dongarra, Sven Hammarling, Greg Henry, Antoine Petitet, et al. *ScaLAPACK users' guide*, volume 4. siam, 1997.

[62] S Jolliet, Alberto Bottino, P Angelino, Roman Hatzky, TM Tran, BF McMillan, O Sauter, K Appert, Yasuhiro Idomura, and Laurent Villard. A global collisionless pic code in magnetic coordinates. *Computer Physics Communications*, 177(5):409–425, 2007.

[63] T Vernay, S Brunner, L Villard, BF McMillan, S Jolliet, TM Tran, and A Bottino. Synergy between ion temperature gradient turbulence and neoclassical processes in global gyrokinetic particle-in-cell simulations. *Physics of Plasmas (1994-present)*, 19(4):042301, 2012.

[64] BF McMillan, S Jolliet, TM Tran, L Villard, A Bottino, and P Angelino. Long global gyrokinetic simulations: Source terms and particle noise control. *Physics of Plasmas (1994-present)*, 15(5):052308, 2008.

[65] Stephan Brunner, Ernest Valeo, and John A Krommes. Collisional delta-f scheme with evolving background for transport time scale simulations. *Physics of Plasmas*, 6(12):4504, 1999.

[66] Thibaut Vernay, Stephan Brunner, Laurent Villard, BF McMillan, Olivier Sauter, Sébastien Jolliet, Trach-Minh Tran, and Alberto Bottino. Global collisional gyrokinetic simulations of itg microturbulence starting from a neoclassical equilibrium. In *Journal of Physics: Conference Series*, volume 260, page 012021. IOP Publishing, 2010.

[67] Hideo Sugama. Gyrokinetic field theory. *Physics of Plasmas (1994-present)*, 7(2):466–480, 2000.

[68] Niels Winsor, John L Johnson, and John M Dawson. Geodesic acoustic waves in hydromagnetic systems. *Physics of Fluids (1958-1988)*, 11(11):2448–2450, 1968.

[69] Akihide Fujisawa. A review of zonal flow experiments. *Nuclear Fusion*, 49(1):013001, 2009.

[70] Hideo Sugama and T-H Watanabe. Collisionless damping of zonal flows in helical systems. *Physics of Plasmas (1994-present)*, 13(1):012501, 2006.

[71] A. Biancalani, A. Bottino, Ph. Lauber, and D. Zarzoso. Numerical validation of the electromagnetic gyrokinetic code nemorb on global axisymmetric modes. *Nuclear Fusion*, 54(10):104004, 2014.

[72] H Sugama and T-H Watanabe. Erratum:collisionless damping of zonal flows in helical systems[phys. plasmas13, 012501 (2006)]. *Physics of Plasmas (1994-present)*, 14(7):079902, 2007.

[73] T Ido, Y Miura, K Kamiya, Y Hamada, K Hoshino, A Fujisawa, K Itoh, SI Itoh, A Nishizawa, H Ogawa, et al. Geodesic–acoustic-mode in jft-2m tokamak plasmas. *Plasma physics and controlled fusion*, 48(4):S41, 2006.

[74] A Fujisawa, K Itoh, A Shimizu, H Nakano, S Ohsima, H Iguchi, K Matsuoka, S Okamura, SI Itoh, and PH Diamond. Spectrograph of electric field fluctuation in toroidal helical plasma. *Plasma physics and controlled fusion*, 48(4):S31, 2006.

[75] Kimitaka Itoh, Sanae-I Itoh, Patrick H Diamond, Akihide Fujisawa, Masatoshi Yagi, Tetsuo Watari, Yoshihiko Nagashima, and Atsushi Fukuyama. Geodesic acoustic eigenmodes. *Plasma and Fusion Research*, 1:037–037, 2006.

[76] Sergei Winitzki. Cosmological particle production and the precision of the wkb approximation. *Phys. Rev. D*, 72:104011, Nov 2005.

[77] John Heading. *An introduction to phase-integral methods*. Courier Corporation, 2013.

[78] Gilbert W Stewart. On the early history of the singular value decomposition. *SIAM review*, 35(4):551–566, 1993.

[79] AG Elfimov. Alfvén continuum deformation by kinetic geodesic effect in rotating tokamak plasmas. *Physics of Plasmas (1994-present)*, 17(2):022102, 2010.

[80] AG Elfimov, RMO Galvao, and RJF Sgalla. Rotation effect on geodesic and zonal flow modes in tokamak plasmas with isothermal magnetic surfaces. *Plasma Physics and Controlled Fusion*, 53(10):105003, 2011.

[81] W Guo, L Ye, D Zhou, X Xiao, and S Wang. Kinetic effect of toroidal rotation on the geodesic acoustic mode. *Physics of Plasmas (1994-present)*, 22(1):012501, 2015.

[82] VI Ilgisonis, VP Lakhin, AI Smolyakov, and EA Sorokina. Geodesic acoustic modes and zonal flows in rotating large-aspect-ratio tokamak plasmas. *Plasma Physics and Controlled Fusion*, 53(6):065008, 2011.

[83] VP Lakhin, VI Ilgisonis, and AI Smolyakov. Geodesic acoustic modes and zonal flows in toroidally rotating tokamak plasmas. *Physics Letters A*, 374(48):4872–4875, 2010.

[84] C Wahlberg. Geodesic acoustic mode induced by toroidal rotation in tokamaks. *Physical review letters*, 101(11):115003, 2008.

[85] F Zonca and L Chen. Radial structures and nonlinear excitation of geodesic acoustic modes. *EPL (Europhysics Letters)*, 83(3):35001, 2008.

[86] Scott E Parker, Charlson Kim, and Yang Chen. Large-scale gyrokinetic turbulence simulations: effects of profile variation. *Physics of Plasmas (1994-present)*, 6(5):1709–1716, 1999.

[87] AM Dimits, G Bateman, MA Beer, BI Cohen, W Dorland, GW Hammett, C Kim, JE Kinsey, M Kotschenreuther, AH Kritz, et al. Comparisons and physics basis of tokamak transport models and turbulence simulations. *Physics of Plasmas (1994-present)*, 7(3):969–983, 2000.

[88] C.M. Greenfield, J.C. DeBoo, T.H. Osborne, F.W. Perkins, M.N. Rosenbluth, and D. Boucher. Enhanced fusion performance due to plasma shape modification of simulated iter discharges in diii-d. *Nuclear Fusion*, 37(9):1215, 1997.

[89] X Lapillonne, BF McMillan, T Görler, S Brunner, T Dannert, F Jenko, F Merz, and L Villard. Nonlinear quasisteady state benchmark of global gyrokinetic codes. *Physics of Plasmas (1994-present)*, 17(11):112321, 2010.

[90] A Bottino, AG Peeters, R Hatzky, S Jolliet, BF McMillan, TM Tran, and L Villard. Nonlinear low noise particle-in-cell simulations of electron temperature gradient driven turbulence. *Physics of Plasmas (1994-present)*, 14(1):010701, 2007.

[91] AG Peeters, C Angioni, and D Strintzi. Toroidal momentum pinch velocity due to the coriolis drift effect on small scale instabilities in a toroidal plasma. *Physical review letters*, 98(26):265003, 2007.

[92] Y Camenen, AG Peeters, C Angioni, Francis James Casson, WA Hornsby, AP Snodin, and D Strintzi. Impact of the background toroidal rotation on particle and heat turbulent transport in tokamak plasmas. *Physics of Plasmas (1994-present)*, 16(1):012503, 2009.

[93] AG Peeters, C Angioni, Y Camenen, Francis James Casson, WA Hornsby, AP Snodin, and D Strintzi. The influence of the self-consistent mode structure on the coriolis pinch effect. *Physics of Plasmas (1994-present)*, 16(6):062311, 2009.

[94] AG Peeters, Clemente Angioni, A Bortolon, Y Camenen, Francis James Casson, Basil Duval, L Fiederspiel, WA Hornsby, Yasuhiro Idomura, T Hein, et al. Overview of toroidal momentum transport. *Nuclear Fusion*, 51(9):094027, 2011.

[95] KH Burrell. Effects of e× b velocity shear and magnetic shear on turbulence and transport in magnetic confinement devices. *Physics of Plasmas (1994-present)*, 4(5):1499–1518, 1997.

[96] AG Peeters, C Angioni, et al. Linear gyrokinetic calculations of toroidal momentum transport in a tokamak due to the ion temperature gradient mode. *Physics of Plasmas (1994-present)*, 12(7):072515, 2005.

[97] RE Waltz, GD Kerbel, and J Milovich. Toroidal gyro-landau fluid model turbulence simulations in a nonlinear ballooning mode representation with radial modes. *Physics of Plasmas (1994-present)*, 1(7):2229–2244, 1994.

[98] RE Waltz, RL Dewar, and X Garbet. Theory and simulation of rotational shear stabilization of turbulence. *Physics of Plasmas*, 5(5):1784, 1998.

[99] Sarah L Newton, Steve C Cowley, and Nuno F Loureiro. Understanding the effect of sheared flow on microinstabilities. *Plasma Physics and Controlled Fusion*, 52(12):125001, 2010.

[100] JW Connor and TJ Martin. Rotation shear and drift wave stability. *Plasma Physics and Controlled Fusion*, 49(9):1497, 2007.

[101] TS Hahm, MA Beer, Z Lin, GW Hammett, WW Lee, and WM Tang. Shearing rate of time-dependent eb flow. *Physics of Plasmas*, 6(3), 1999.

[102] PW Terry. Suppression of turbulence and transport by sheared flow. *Reviews of Modern Physics*, 72(1):109, 2000.

[103] Peter Hill, S Saarelma, B McMillan, A Peeters, and Erwin Verwichte. Perpendicular wavenumber dependence of the linear stability of global ion temperature gradient modes on e× b flows. *Plasma Physics and Controlled Fusion*, 54(6):065011, 2012.

[104] X Garbet, Y Idomura, L Villard, and TH Watanabe. Gyrokinetic simulations of turbulent transport. *Nuclear Fusion*, 50(4):043002, 2010.

[105] Ben F McMillan, S Jolliet, TM Tran, L Villard, A Bottino, and P Angelino. Avalanchelike bursts in global gyrokinetic simulations. *Physics of Plasmas (1994-present)*, 16(2):022310, 2009.

[106] S Saarelma, Peter Hill, A Bottino, G Colyer, AR Field, B McMillan, A Peeters, CM Roach, et al. Global gyrokinetic turbulence simulations of mast plasmas. *Plasma Physics and Controlled Fusion*, 54(8):085012, 2012.